UNIVERSIDAD DE CHILE
FACULTAD DE CIENCIAS FÍSICAS Y MATEMÁTICAS
DEPARTAMENTO DE FÍSICA

VORTICES INDUCED BY ELECTRIC AND MAGNETIC FIELD AND TOPOLOGICAL TRANSITIONS IN OUT OF EQUILIBRIUM SYSTEMS

TESIS PARA OPTAR AL GRADO DE
MAGÍSTER EN CIENCIAS, MENCIÓN FÍSICA

VALESKA TATIANA ZAMBRA AGUIRRE

PROFESOR GUÍA:
MARCEL G. CLERC GAVILÁN

MIEMBROS DE LA COMISIÓN:
DIANA DULIĆ
MICHAŁ KOWALCZYK
MARIO WILSON

Este trabajo ha sido parcialmente financiado por Millenium Institute for Research in Optics MIRO

SANTIAGO DE CHILE
2020

RESUMEN TESIS PARA OPTAR
AL GRADO DE MAGÍSTER EN CIENCIAS, MENCIÓN FÍSICA
POR: VALESKA TATIANA ZAMBRA AGUIRRE
FECHA: 2020
PROF. GUÍA: MARCEL G. CLERC GAVILÁN

VORTICES INDUCED BY ELECTRIC AND MAGNETIC FIELD AND TOPOLOGICAL TRANSITIONS IN OUT OF EQUILIBRIUM SYSTEMS

Electrically driven nematic liquid crystal layers are ideal platform for studying the interactions of local topological defects, called vortices or umbilical defects. This thesis is devoted to experimentally and theoretically study the behavior of vortices in nematic liquid crystal cells under the influence of external electric and magnetic field. This dissertation is composed of six chapters and appendixes that contain articles published and manuscripts submitted during this work. In the first chapter, we present a theoretical and experimental framework required to understand the present dissertation.

In second chapter, we investigate the interaction of vortices in an inhomogeneous nematic liquid crystal cell. Experimentally, we characterize the coarsening dynamics in samples containing glass beads as spacers and show that the inclusion of such imperfections changes the critical exponent of the coarsening law. Moreover, we demonstrate that slightly deformed beads attract vortices of both topological charges, thus, presenting a mainly quadrupolar behavior. Theoretically, based on a model of diluted vortices in a dipolar medium, a $2/3$ exponent is inferred, which is consistent with the experimental observations.

In third chapter, we investigate an experiment involving a liquid crystal cell under the influence of a low frequency oscillatory electric field. Unexpectedly, we observe topological states of matter in systems with injection and dissipation of energy. An amplitude equation with oscillatory parameters allows us to characterize the topological transition.

In fourth chapter, we study a nematic liquid crystal cell under the combined effect of the electric and the magnetic field of a magnetic ring which exhibits a stable vortex triplet. Theoretically, an amplitude equation with topological forcing allows us to reveal the origin of the vortex triplet. A lattice of vortices is observed when the frequency of the applied voltage is decreased. By adding an inertia term to the amplitude equation it is possible to reveal the origin of this phenomenon.

In fifth chapter, we investigate how the inherent fluctuations affect the vortex nucleation. Experimentally, the number of vortices was studied as a function of voltage and temperature. Theoretically, a model was derived to describe the number of vortices as a function of different parameters. Numerically, the number of vortices was studied as a function of the bifurcation parameter, anisotropy, and noise, showing a quite fair agreement with the experimental observations.

Finally, in chapter six, we summarize the conclusions of this thesis and related perspectives.

RESUMEN TESIS PARA OPTAR
AL GRADO DE MAGÍSTER EN CIENCIAS, MENCIÓN FÍSICA
POR: VALESKA TATIANA ZAMBRA AGUIRRE
FECHA: 2020
PROF. GUÍA: MARCEL G. CLERC GAVILÁN

VORTICES INDUCIDOS POR CAMPOS ELÉCTRICO Y MAGNÉTICO Y TRANSICIONES TOPOLÓGICAS EN SISTEMAS FUERA DEL EQUILIBRIO

Películas delgadas de cristal líquido nemático impulsadas eléctricamente son una plataforma ideal para estudiar las interacciones de los defectos topológicos locales, llamados vórtices o defectos umbilicales. Esta tesis está dedicada a estudiar de forma experimental y teórica el comportamiento de los vórtices en celdas de cristal líquido nemático bajo la influencia de campos eléctricos y magnéticos externos. Esta investigación está compuesta por seis capítulos y anexos que contienen artículos publicados y manuscritos presentados durante este trabajo. En el primer capítulo, presentamos un marco teórico y experimental necesario para comprender la presente tesis.

En el segundo capítulo, investigamos la interacción de vórtices en una celda de cristal líquido nemático no homogénea. Experimentalmente, caracterizamos la dinámica de engrosamiento (distancia promedio entre vórtices) en muestras que contienen perlas de vidrio como espaciadores y mostramos que la inclusión de tales imperfecciones cambia el exponente crítico de la ley de engrosamiento. Además, demostramos que las perlas ligeramente deformadas atraen vórtices de ambas cargas topológicas, presentando así un comportamiento principalmente cuadrupolar. Teóricamente, basado en un modelo de vórtices diluidos en un medio dipolar, se infiere un exponente de $2/3$, lo cual es consistente con las observaciones experimentales.

En el tercer capítulo, investigamos un experimento que involucra una celda de cristal líquido bajo la influencia de un campo eléctrico oscilatorio de baja frecuencia. Inesperadamente, observamos estados topológicos de la materia en sistemas con inyección y disipación de energía. Una ecuación de amplitud con parámetros oscilatorios nos permite caracterizar la transición topológica.

En el cuarto capítulo, estudiamos una celda nemática de cristal líquido bajo el efecto combinado del campo eléctrico y magnético de un anillo magnético que exhibe un triplete de vórtice estable. Teóricamente, una ecuación de amplitud con forzamiento topológico nos permite revelar el origen del triplete de vórtices. Se observa una red de vórtices cuando disminuye la frecuencia del voltaje aplicado. Añadiendo un término de inercia a la ecuación de amplitud es posible revelar el origen de este fenómeno.

En el quinto capítulo, investigamos cómo las fluctuaciones inherentes afectan la nucleación de vórtices. Experimentalmente, se estudió el número de vórtices en función del voltaje y la temperatura. Teóricamente, se derivó un modelo para describir el número de vórtices en función de diferentes parámetros. Numéricamente, se estudió el número de vórtices en función del parámetro de bifurcación, anisotropía y ruido, mostrando una concordancia bastante justa con las observaciones experimentales.

Finalmente, en el capítulo seis, resumimos las conclusiones de esta tesis y las perspectivas relacionadas.

to my family

Agradecimientos

Nunca pensé que iba a defender mi tesis en medio de una pandemia mundial, la cuarentena y el distanciamiento social me han puesto meláncolica, perdón si escribí mucho.
Quiero agradecer a todos quienes me han apoyado, enseñado y formado tanto como persona como en mi carrera científica. Partiendo por los que han estado desde siempre, a mi madre por enseñarme su valentía, fortaleza y fomentar en mi el pensamiento crítico desde que era pequeña. A mi yaya y mi tata por su amor y apoyo incondicional, a mis hermanos por alegrarme los dias. A mis tios, Tomy, Roberto, Yuvicza, Francisco y Laura, por todo el cariño que me han dado siempre, por creer en mi y apoyarme siempre en cada uno de mis pasos . A mis primxs y a toda mi familia. A la tía María por su cariño, apoyo y enseñarme a vivir la vida con alegría.

Agradecer a mi esposo por su apoyo, risas, compañía y por prepararme comida rica mientras yo escribía la tesis. A mis suegros por todo su apoyo y cariño. A mis amigas de la vida, Guzana, Cony, Pame, Kissy, Tate y Vale por todo el apoyo, consejos y buenos momentos. A mis profesoras de ciencia del colegio, Ana García y María Mercedes Flores por enseñarme y guiarme en mis primeros pasos en la ciencia.

A mis compañeros/amigxs del LAFER, Cami, Gregorio, Enrique, Fabián, Michel, Alejandro, Gladys, Karin, David y Sebastian, por todas las risas, anécdotas y buenos momentos vividos.

Agradecer a las instituciones, fundaciones, y medios de comunicación que me han apoyado en la divulgación científica: Explora Conicyt, Universidad de Chile, Injuv, Fundación Natida, Ingeniosas, Tremendas, Bacanes, Corporación Más Ciencia Más Sueños, Txs Radio y Diario Atacama.

Agradecer a mi profesor guía, Marcel Clerc, por su entrega, tiempo y dedicación en formarme como científica, por contagiar con su entusiasmo y alegría el hacer ciencia día a día, y por sus sabias palabras. También agradecer a todos aquellas personas con las que colaboré en el desarrollo de esta tesis, profesor Michal Kowalczyk, Enrique Calisto, Esteban Aguilera, Raouf Barboza, Stefania Residori, Umberto Bortolozzo, Roberto Gajardo y Michel Ferré. A los profesores Diana Dulic, Miguel Kiwi y Jaime Roesler por todo su apoyo.

Finalmente quiero agradecer al profesor Enrique Tirapegui, Q.E.P.D., por todo su apoyo, sabiduría brindada, su calidad humana y por ser el padre de la física no lineal en Chile, legado que seguiremos cultivando.

Contents

List of Figures

Introduction

Robust phenomena correspond to dynamical behaviors that occurs in different physical systems. Vortices are a robust phenomenon. In a simple way, we can say that a vortex is a kind of whirlpool that has a singularity at its center and we can see it in different contexts such as in a spiral galaxy, in hurricanes, in the eddies that form in our heads, eddies in the sea, among others (see Fig.1). In the last decades, the study of vortices in different areas of physics and mathematics such as condensed matter, superconductors, topology, liquid crystals and optics have acquired great interest and contributed to the development in different areas. In 2016 J. Michael Kosterlitz and David J. Thouless received the Nobel Prize in Physics for their discoveries of topological transitions and topological phases of matter.

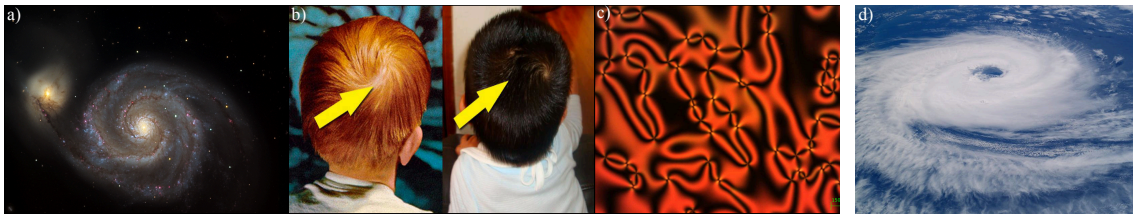

Figure 1: Vortices in different physical systems. a)Spiral galaxy. b) Eddies in heads. c)Vortices in liquid crystal. d)Hurricane.

The study of vortices is still very relevant to understand different physical phenomena and for the development of future technologies, such as photonics, optical communications systems, optical storage and interconnect, biomedical imaging. In this dissertation, in the context of liquid crystals, the behavior of vortices in nematic liquid crystal was studied under the influence of electric and magnetic fields, both experimentally and theoretically. All experiments were performed in the Laboratory of Robust Phenomena in Optics LAFER `https://www.cec.uchile.cl/~lafer/`.

0.1 Objectives

To investigate the behavior of vortices in out-of-equilibrium nematic liquid crystals layers by applying external electric and magnetic field.

Specific objectives:

- Develop the ability to design and perform optical experimental setups in microscopes to study liquid crystals.
- Characterize and analyze the experimental results obtained.
- Build a theoretical model and establish the mechanisms that describe the observed Topological transitions.
- Implement numerical simulations that validate the proposed model.

0.2 Figure notation and abbreviations

In this thesis, the notation used to refer to a figure is the following:

see figure *Chapter.Number*,

where *Chapter* correspond to the chapter where the figure is located in the document and *Number* is the figure numeration in that chapter.
Some of the most commonly used abbreviations in the thesis are:

- LC: Liquid Crystal.
- NLC: Nematic Liquid Crystal.
- QWP: Quarter Wave Plate.
- ITO: Indium, Tin and Oxide.
- MR: Magnetic Ring.
- CMOS: Complementary Metal Oxide Semiconductor.

Chapter 1

Framework

In this chapter the necessary elements will be provided to understand the following chapters of this thesis.

1.1 Liquid crystals

Liquid crystals are a state of aggregation of matter that have properties of both crystalline solids and isotropic liquids [1, 2]. From the crystalline solid they inherit anisotropy and from the liquid they inherit fluidity. Calamitic liquid crystals are characterized by being elongated aromatic molecules assuming rod like geometry (see Figure 1.1) that have local orientation order but not at long distances. The liquid crystals have the property of interacting strongly with light, electric and magnetic field, and temperature [2].

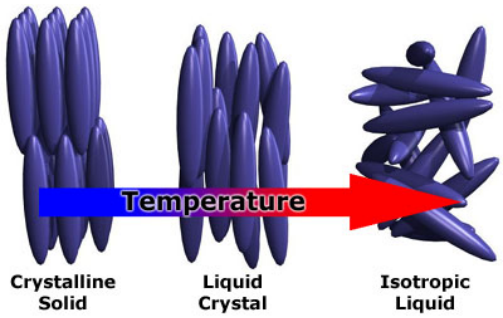

Figure 1.1: Liquid crystal molecules.

Discovery

Liquid crystals were discovered by the Austrian botanist Friedrich Reinitzer in 1888 when he discovered that cholesterol Benzoate had two melting points, at 145.5 °C it became an opaque and dense liquid and at 178.5°C it became a transparent liquid and light (Figure 1.2). A year later, Otto Lehman discovered that cholesteryl benzoate, in the opaque phase, had areas of crystalline molecular structure and called it liquid crystal.

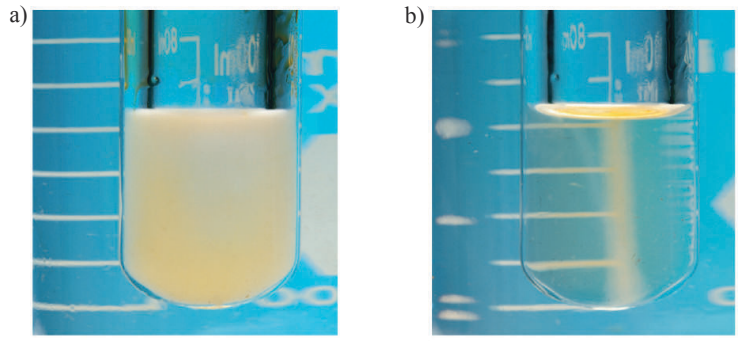

Figure 1.2: Cholesterol benzoate subjected to an increase in temperature. b) At 145.5°C it melts into an opaque and dense liquid, b) At 178.5°C it melts into a light and transparent liquid.

Mesophases

Liquid crystal molecules present an orientational order that is characterized by a director vector $\vec{n}$, since the molecules are quadrupolar this vector has the symetry $\vec{n} = -\vec{n}$. As the temperature varies, the liquid crystal molecules change their orientation structure, forming different mesophases as shown in Figure 1.3.
The Smectic phase is characterized in that the molecules are located in parallel layers with about 2 ángstrom of distance between them and the molecular orientation is constant.. In the Nematic phase, the position of the molecules are completely disordered, but point in the same direction. The only regularity is the constancy of orientation. In the Cholesteric phase, the molecular axis changes direction sequentially as it passes from one layer to another, describing a helix-shaped trajectory [2, 3].

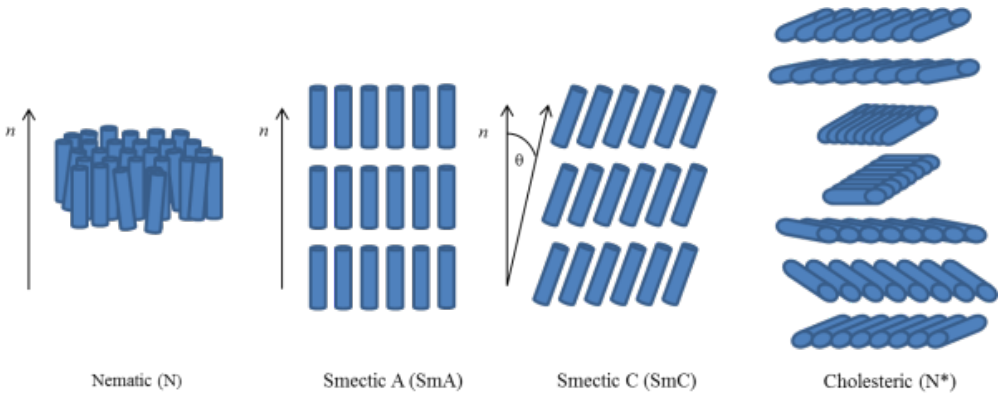

Figure 1.3: Mesophases of liquid crystals.

The nematic liquid crystals have strong coupling with electric and magnetic field, which is why they are the most widely used in the industry and therefore have been the most widely studied. This thesis concentrates its efforts on studying the behavior of vortices in nematic liquid crystal in the presence of external fields, therefore in this section we will focus on describing this mesophase in following lines.

1.2 Free Energy

The nematic liquid crystals undergoes different deformations upon applying an external field. These deformations affect the rotation of the molecules in the direction in which the torsion is being applied and do not modify the center of gravity of the molecules. The main deformations suffered by a nematic liquid crystal are splay, twist and bend [4].
Figure 1.4 shows the respective deformations.

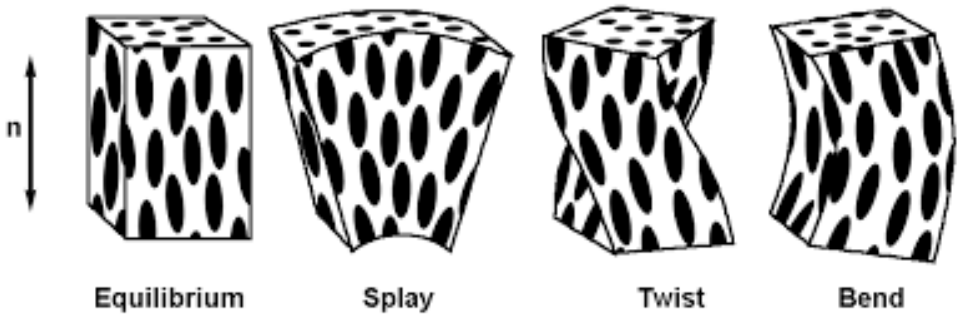

Figure 1.4: Elastic deformations in nematic liquid crystal.

The energy densities for each of these deformations are [1]

$$\begin{aligned} splay : f_1 &= \frac{1}{2} K_1 \left(\nabla \cdot \hat{n}\right)^2, \\ twist : f_2 &= \frac{1}{2} K_2 \left(\hat{n} \cdot \nabla \times \hat{n}\right)^2, \\ bend : f_3 &= \frac{1}{2} K_3 (\hat{n} \times \nabla \times \hat{n})^2, \end{aligned}$$

K_1, K_2 and K_3 are the elastic constants correspond to splay, twist and bend deformation respectly. Then, the Frank-Ossen Free energy density corresponds to

$$F_{\mathrm{d}} = \frac{1}{2} K_1 \left(\nabla \cdot \hat{n}\right)^2 + \frac{1}{2} K_2 \left(\hat{n} \cdot \nabla \times \hat{n}\right)^2 + \frac{1}{2} K_3 (\hat{n} \times \nabla \times \hat{n})^2. \tag{1.1}$$

Note that if we want to fully describe the energy density in a liquid crystal, it will be necessary to add a corresponding energy term from the treatment that the molecules have on the surface and a term for each external fields applied.

Surface anchoring

The surface on which a liquid crystal is located can be chemically treated to anchor in a strong or weak way the molecules that are at borders. A strong anchoring means that the molecules are strongly attached to the boundary with the surface and they do not respond to

the action of external fields, therefore the surface energy can be considered constant and does not affect equation (1.1). When the molecules are strongly anchored perpendicular (parallel) to the surface it is called homeotropic (planar) anchoring as shown in Figure 1.5. A weak anchoring means that molecules that are at the boundary with the surface respond to the presence of external fields, and here a surface energy term should be considered, but for the purposes of this thesis we will not delve into it.

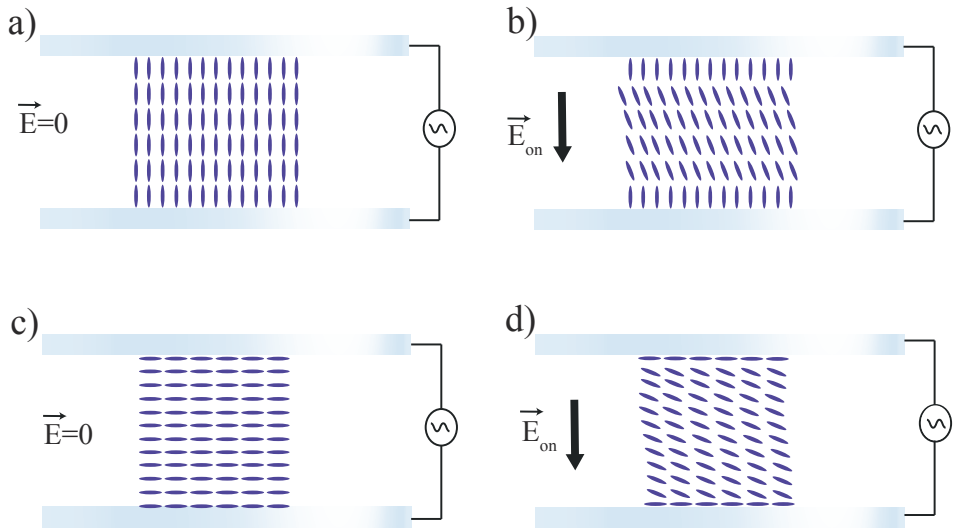

Figure 1.5: Strong anchonring in a nematic liquid crystal cell. a) Homeotropic anchoring liquid crystal cell without external field. b) Homeotropic anchoring liquid crystal cell with vertical external field. c) Planar anchoring liquid crystal cell without external field. d) Planar anchoring liquid crystal cell with a vertical external field.

External fields

If we consider an external electric field applied $\vec{E}$ to a nematic liquid crystal, the displacement of electric field is

$$\vec{D} = \bar{\bar{\varepsilon}} \cdot \vec{E},$$

where $\bar{\bar{\varepsilon}}$ is the dielectric constant tensor. For a uniaxial nematic, $\bar{\bar{\varepsilon}}$ has two main components, one in a direction parallel to the director vector $\varepsilon_{\parallel}$ and the other in any direction perpendicular to the director vector $\varepsilon_{\perp}$, that is.

$$\bar{\bar{\varepsilon}} = \begin{bmatrix} \varepsilon_{\perp} & 0 & 0 \\ 0 & \varepsilon_{\perp} & 0 \\ 0 & 0 & \varepsilon_{\parallel} \end{bmatrix}$$

For dielectric tensor ε, from [1], we have

$$\varepsilon_{\alpha\beta} = \varepsilon_{\perp}\delta_{\alpha\beta} + (\varepsilon_{\parallel} - \varepsilon_{\perp})n_{\alpha}n_{\beta}.$$

Then, $\vec{D}$ can be written as follows

$$\vec{D} = -\varepsilon_\perp \vec{E} + \left(\varepsilon_\parallel - \varepsilon_\perp\right)\left(\hat{n}\cdot\vec{E}\right)\hat{n},$$

Note that $\left(\varepsilon_\parallel - \varepsilon_\perp\right) = \Delta\varepsilon$ corresponds to the dielectric anisotropy. Then, the electrical interaction energy density is

$$\begin{aligned}\mu_{\mathrm{e}} &= \int_0^E \vec{D}\cdot \mathrm{d}\vec{E}, \\ &= -\frac{1}{2}\varepsilon_\perp\left(\vec{E}\cdot\vec{E}\right) - \frac{\Delta\varepsilon}{2}\left(\hat{n}\cdot\vec{E}\right)^2,\end{aligned} \tag{1.2}$$

note that in (1.2), the first term is independent of the molecular orientation, so it can be neglected for the director dynamics, obtaining that the density of free electric energy is

$$F_{\mathrm{e}} = -\frac{\Delta\varepsilon}{2}\left(\hat{n}\cdot\vec{E}\right)^2. \tag{1.3}$$

Analogously, in the presence of an external magnetic field, the magnetization satisfies the relation

$$M = \bar{\bar{\chi}}_m \vec{H},$$

for a uniaxial nematic, the magnetic supectibility takes the form

$$\bar{\bar{\chi}}_m = \begin{bmatrix} \chi_\perp^m & 0 & 0 \\ 0 & \chi_\perp^m & 0 \\ 0 & 0 & \chi_\parallel^m \end{bmatrix}.$$

Thereby, the magnetization es

$$\vec{M} = -\chi_\perp \vec{H} + \left(\chi_\parallel - \chi_\perp\right)\left(\hat{n}\cdot\vec{H}\right)\hat{n},$$

Note that $\left(\chi_\parallel - \chi_\perp\right) = \Delta\chi_a$ corresponds to the magnetic anisotropy. Then, the magnetic interaction energy density is

$$\begin{aligned}\mu_m &= \int_0^H \vec{M}\cdot \mathrm{d}\vec{H}, \\ &= -\frac{1}{2}\chi_\perp\left(\vec{H}\cdot\vec{H}\right) - \frac{\Delta\chi_a}{2}\left(\hat{n}\cdot\vec{H}\right)^2,\end{aligned}$$

Notice that the first term is independent of the molecular orientation, so it can be neglected, obtaining that the density of free magnetic energy is

$$F_m = -\frac{\chi_a}{2}\left(\hat{n}\cdot\vec{H}\right)^2. \tag{1.4}$$

Therefore, the total free energy density of the deformation of a nematic liquid crystal with strong anchorage and in the presence of electric and magnetic field is

$$F = F_{\mathrm{d}} + F_{\mathrm{e}} + F_m$$

then,

$$F = \frac{1}{2}K_1\left(\nabla\cdot\hat{n}\right)^2 + \frac{1}{2}K_2\left(\hat{n}\cdot\nabla\times\hat{n}\right)^2 + \frac{1}{2}K_3(\hat{n}\times\nabla\times\hat{n})^2 - \frac{\Delta\varepsilon}{2}\left(\hat{n}\cdot\vec{E}\right)^2 - \frac{\chi_a}{2}\left(\hat{n}\cdot\vec{H}\right)^2 \tag{1.5}$$

1.3 Fréedericksz Voltage

Consider a nematic liquid crystal cell of thickness d, with homeotropic anchoring and negative dielectric anisotropy $\Delta\varepsilon < 0$ subjected to an electric field $\vec{E}$ in the $\hat{z}$ direction. The molecular reorientation energy will be

$$F = \frac{1}{2}K_1\left(\nabla\cdot\hat{n}\right)^2 + \frac{1}{2}K_2\left(\hat{n}\cdot\nabla\times\hat{n}\right)^2 + \frac{1}{2}K_3(\hat{n}\times\nabla\times\hat{n})^2 - \frac{\Delta\varepsilon}{2}\left(\hat{n}\cdot\vec{E}\right)^2, \tag{1.6}$$

we minimize this energy using (the inertial term is negligible due to strong relation viscosity γ [1])

$$\gamma\frac{\vec{n}}{\mathrm{d}t} = -\frac{\delta F}{\delta\vec{n}},$$

considering that $|n| = 1$, then,

$$\gamma\frac{\vec{n}}{\mathrm{d}t} = -\frac{\delta F}{\delta\vec{n}} + \vec{n}\left(\vec{n}\cdot\frac{\delta F}{\delta\vec{n}}\right),$$

we obtain [5]

$$\begin{aligned}\gamma\frac{\mathrm{d}\vec{n}}{\mathrm{d}t} = K_3[\nabla^2\vec{n} - \vec{n}\left(\vec{n}\cdot\nabla^2\vec{n}\right)] + (K_3 - K_1)[\vec{n}\left(\vec{n}\cdot\nabla\right)\left(\nabla\cdot\vec{n}\right) - \nabla\left(\nabla\cdot\vec{n}\right)]\\ +(K_2 - K_3)\left[2\left(\vec{n}\cdot\nabla\times\vec{n}\right)\left(\vec{n}\left(\vec{n}\cdot\nabla\times\vec{n}\right) - \nabla\times\right) + \vec{n}\times\nabla\left(\vec{n}\cdot\nabla\times\vec{n}\right)\right]\\ -\Delta\varepsilon\left(\vec{n}\cdot E\right)\left(\vec{n}\left(\vec{n}\cdot\vec{E}\right) - \vec{E}\right).\end{aligned}$$

To find when the nematic molecules are reoriented due to the action of the electric field and the competition with elastic force, for this we consider $\vec{n} \approx (u, v, 1 - \frac{u^2+v^2}{2})$ with u and v are small perturbations, and negllecting high order terms

$$\begin{aligned}\gamma\frac{\mathrm{d}u}{\mathrm{d}t} &= K_3\partial_{zz}u - \Delta\varepsilon E^2 u,\\ \gamma\frac{\mathrm{d}v}{\mathrm{d}t} &= K_3\partial_{zz}v\Delta\varepsilon E^2 v.\end{aligned} \tag{1.7}$$

Using the ansatz that satisfies hometropic boundary conditions, that is $u = v = 0$ at $z = 0$ and $z = \mathrm{d}$, then the ansatz which we choose to study the stability is

$$u = v = sin(kz)\mathrm{e}^{\sigma t},$$

with $k = n\pi/\mathrm{d}$. Using this ansatz in (1.7), and straight forward calculations

$$\gamma\sigma = -K_3k^2 - \Delta\varepsilon E^2.$$

We look for the critical value of E necessary to generate the molecular reorientation of the nematic, then, for n=1 and $\sigma = 0$,

$$E = \sqrt{\frac{-K_3k^2}{\Delta\varepsilon\mathrm{d}^2}} = \sqrt{\frac{-K_3\pi^2}{\Delta\varepsilon\mathrm{d}^2}}.$$

Thus, the critical voltage is

$$V_F = \sqrt{\frac{-K_3\pi^2}{\Delta\varepsilon}} \tag{1.8}$$

This critical voltage is called Fréedericksz Voltage [6] and corresponds to the minimum voltage necessary for the electrical force to be greater than the elastic force generating the molecular reorientation.

1.4 Vortices in liquid crystal

In a nematic phase liquid crystal cell with negative dielectric constant and homeotropic anchoring, the molecules tend to align perpendicular to an applied electric field when the electric field has a voltage higher than Fréedericksz Voltage by minimizing the Frank-Ossen energy. On the other hand, due to the elasticity and boundary conditions of the material, the molecules tend to be parallel to the electric field. Hence, the balance between electric and elastic force, causes the molecules to have different orientations throughout the sample. This effect promotes formation of topological defects called vortices, umbilical defects or disclination line [7], that can be observed under linear crossed polarization [8]. These defects interact with each other and annihilate by pairs.

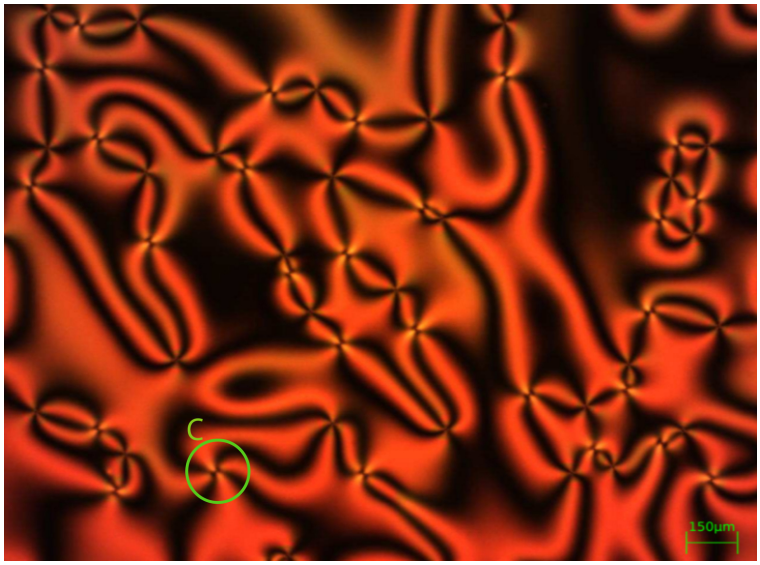

Figure 1.6: Vortices in nematic liquid crystal.

Theoretically, the vortex dynamics in liquid crystals has been described near the reorientational instability of the molecules (Fréedericksz transition) [9,10] by the anisotropic Ginzburg Landau equation with real coefficients [9]

$$\partial_t A = \mu A - |A|^2 A + \nabla^2 A + \delta \partial_{\eta\eta} \bar{A}, \tag{1.9}$$

where A accounts for the amplitude of the critical mode, μ is the bifurcation parameter which describes the diference between the applied voltage V_0 and the critical Fréedericksz voltage V_F, $\mu \propto V_o - V_F$. δ is de the anisotropy of the material defined by $\delta = (K_1 - K_2)/(K_1 + K_2)$, with K_1 and K_2 are elastic deformation constants splay and twist of the liquid crystal, respectively. The spatial coupling is described by the symbol $\partial_\eta = \partial_x + \mathrm{i}\partial_y$ and the Laplacian $\nabla^2 = \partial_\eta \partial_{\bar{\eta}}$.
A vortex is characterized by having a phase singularity at the point where the amplitude A is 0, this singularity is characterized through the topological charge, defined as [8]

$$m = \frac{1}{2\pi} \oint_C \nabla\theta(\vec{r}) \mathrm{d}\vec{l} = \frac{1}{2\pi} \oint \mathrm{d}\theta \tag{1.10}$$

where C is any curve that encloses a vortex (see Figure 1.6) and m is an integer. Once vortices are created, they interact and annihilate with the vortex of opposite topological charge. Figure 1.7 shows the vortex solutions of equation (1.9). For a vortex of topological charge $+1$, the module of A has a circular core and a phase jump of $+\ 2\pi$. For a negative vortex -1, the module of A has a square core and a phase jump of -2π [9].

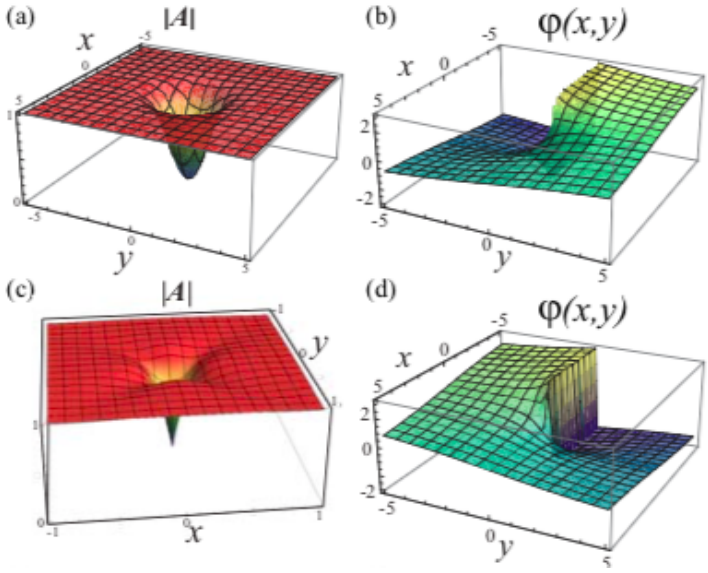

Figure 1.7: Positive and negative vortex solutions of equation (1.9). a) and c) correspond to the plot of the module $|A|$ for a positive and negative vortex, respectively. b) and c) correspond to the plot of the phase of A, and $\psi = arctan\,(\mathrm{Im}(A)/\,\mathrm{Re}(A))$, for a positive and negative vortex respectively.

Different research groups [8, 11] studied the behavior of vortices in nematic liquid crystal and have demonstrated that, for long-distance, the interaction between two vortices of opposite charge is proportional to the inverse of the distance between them [8], and that the density of vortices, in a homogeneous liquid crystal cell, is proportional to the inverse of time [11].

1.5 Topological transitions

There are different phases of matter, such as solid, liquid, gaseous, plasma, Bose-Einstein condensate, among others [12]. By changing a macroscopic parameter such a temperature, pressure, etc. a system undergoes a phase transition and changes from one state to another, changing its properties. In the 20th century, Landau showed that different phases have different symmetries and in a phase transition, a higher symmetry group is divided into a lower symmetry subgroup, thus, a phase transition implies a symmetry break [13]. For example, the cooling of a fluid in a crystalline solid breaks the symmetry continuous of translation since each point in the fluid has the same properties but when it becomes a crystal, each point does not have the same properties. Another example is the phase transition a magnet undergoes as the temperature rises beyond a critical value to move from a ferromagnetic

state to a paramagnetic state. The ferromagnetic state has a magnetization that breaks the rotational symmetry, and then it is restored to the paramagnetic state [14].
However, at beginnings of 70's, Berezinskii, Kosterlitz and Thouless discovered that there is a new type of phase transition called topological phase transition [15, 16]. The main characteristic of this type of phase transition is that the transition occurs without any symmetry breaking. Thus, the distinction between topological phases is not in their symmetry but in their topology. Note that the topology is the study of invariant properties under continuous deformation. This new understanding of the phase transitions of matter that they achieved made them winners of the 2016 Nobel Prize in Physics. In the following lines we will explain the Kosterlitz-Thouless transition.

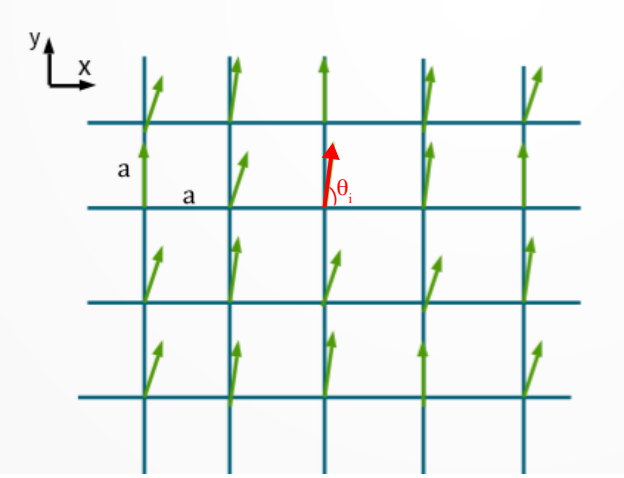

Figure 1.8: Square lattice of spins that can rotate freely.

Consider an infinite square lattice made of spins that can rotate freely.
The energy of the system will correspond to the interaction of the spins with their closest neighbors,

$$H = -J \sum_{<\mathrm{i},j} \vec{S}_\mathrm{i} \cdot \vec{S}_j = -J \sum_{<\mathrm{i},j>} cos(\theta_\mathrm{i} - \theta_j), \tag{1.11}$$

where the sum is for the closest neighbors and θ the angle that the spin forms with respect to the x axis (see Fig.1.8). Assuming that the direction of the spin varies slowly when moving through the network, that is, $\theta(\vec{r}) \approx \theta$.
For close neighbors, the angles will have similar values, then, $\theta_\mathrm{i} - \theta_j$ will have values close to 0, hence, if we expand $\cos(\theta_\mathrm{i} - \theta_j)$ as a series of powers, the equation (1.11) becomes

$$H = -2JN + \frac{J}{2} \sum_{<\mathrm{i},j>} (\theta_\mathrm{i} - \theta_j)^2, \tag{1.12}$$

where N is the total number of spins. Let a be the separation distance between two neighboring spins of the square lattice, then

$$\theta_{\mathrm{i},j} - \theta_{\mathrm{i},j+a} \approx -\frac{\partial\theta}{\partial x} \left(x_{(\mathrm{i},j)} - x_{(\mathrm{i},j+a)} \right) \approx -a \frac{\partial\theta}{\partial x}. \tag{1.13}$$

In the square lattice, according to Figure 1.8, we can see that a spin will have to 4 neighbors, then, applying (1.13) to the 4 neighbors and replacing it in (1.12), we obtain

$$H = H_0 + \frac{J}{4}\sum_{\mathrm{i}}\sum_{k}^{4}\left(\theta_{\mathrm{i}} - \theta_k\right)^2$$

$$H = H_0 + \frac{J}{4}\sum_{\mathrm{i}} a^2\left(\left(\frac{\partial\theta}{\partial x}\right)_{\mathrm{i}}^2 + 2\left(\frac{\partial\theta}{\partial y}\right)_{\mathrm{i}}^2\right),$$

with $H_0 = -2JN$. The previous expression, we can write it continuously as

$$H = H_0 + \frac{J}{2}\int \mathrm{d}\vec{r}\,(\vec{\nabla}\theta)^2. \tag{1.14}$$

Kosterlitz and Thouless propose that thermal fluctuations generate vortices in the system of the square lattice of spines [16]. Using (1.14) we have that the energy for a vortex is

$$E_{vor} = E_0 + \frac{J}{2}a^2\int \mathrm{d}\vec{r}(\vec{\nabla}\theta)^2.$$

Note that a vortex has rotational symmetry, therefore, for a vortex of charge ± 1, $|\vec{\nabla}\theta(\vec{r})| = \frac{1}{r}$, then,

$$E_{vor} = E_0 + J\pi a^2 n^2\int_a^L \frac{r\mathrm{d}r}{r^2},$$

$$E_{vor} = E_0 + J\pi a^2 n^2\ ln(L/a), \tag{1.15}$$

where a is the size of the vortex core and L is the length of the system. Since $L >> a$, therefore, the vortex energy diverges, that is, infinite energy is needed to create a vortex.
The energy of a pair of vortices of opposite topological charges is

$$E_{2v} = 2E_0 + \frac{J}{2}\int \mathrm{d}\vec{r}(\vec{\nabla}\theta_1 + \nabla\vec{\theta_2})^2,$$

$$E_{2v} = 2E_0 + \frac{J}{2}\int \mathrm{d}\vec{r}(\vec{\nabla}\theta_1)^2 + \frac{J}{2}\int \mathrm{d}\vec{r}(\vec{\nabla}\theta_2)^2 + J\int \mathrm{d}\vec{r}\vec{\nabla}\theta_2\vec{\nabla}\theta_1,$$

$$E_{2v} = 2E_0 - 2\pi J n^2 ln(r/a). \tag{1.16}$$

With r the distance between the centers of the vortices.
In (1.16) we can see that the energy for a pair of vortices is finite, therefore, creating and destroying them is possible. Therefore, it is easier for the system to create pairs of vortices of opposite topological charges than individual vortices.
The entropy of an individual vortice is

$$S = k_B \ln\left(\frac{L^2}{a^2}\right). \tag{1.17}$$

The expression L^2/a^2 are the possible positions for a vortex of area a^2.
The free energy is $F = E - TS$, then, using (1.15) and (1.17), the free energy for an individual vortex is

$$F = E_0 + Jn^2\pi \ln\left(\frac{L}{a}\right) - Tk_B\left(\frac{L^2}{a^2}\right),$$

$$F = E_0 + (J\pi n^2 - 2Tk_B)\ln\left(\frac{L}{a}\right).$$

Since L tends to infinity, we have the following cases

$$T < \frac{J\pi}{2k_b} \rightarrow F \sim \infty,$$

$$T > \frac{J\pi}{2k_b} \rightarrow F \sim -\infty.$$

For $F \sim \infty$ the system is unstable and prefers not to have individual vortices, for $F \sim -\infty$ the system is stable and prefer to have individual vortices [16, 17] (see Figure 1.9). Briefly, it can be stated that there is a critical temperature, T_{KT}, below which the existance of individual vortices is not possible and it is possible above it. However, the fact that under the temperature T_{KT} it is not possible to have individual vortices, does not remove the fact that it is possible to have pairs of vortices of opposite topological charge, since as we saw in (1.16) the energy of having these pairs of vortices in finite.

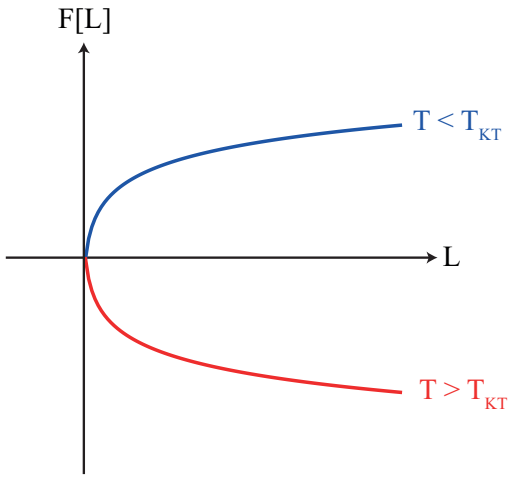

Figure 1.9: Free energy for an individual vortice. The blue curve corresponds to $T < T_{KT}$ and is unstable. The red curve corresponds to $T > T_{KT}$ and is stable.

Thus, the Kosterlitz-Thouless Transition consists of passing from a phase of lower temperature in which there are pairs of vortices (of opposite topological charges) to a phase of higher temperature in which there are individual vortices (see Figure 1.10). The critical temperature at which this transition occurs is $T_{KT} = \frac{J\pi}{2K_B}$.
Note that if we calculate the order parameter for this system, which corresponds to the expected value of the x projection of the spin $\langle S_x \rangle$, through a series of calculations, we obtain

$$\langle S_x \rangle = \langle cos(\theta(\vec{r})) \rangle = \langle cos(\theta(0)) \rangle,$$
$$\langle S_x \rangle = \frac{\int \mathrm{d}\vec{r}\, cos(\theta(0)) \mathrm{e}^{-\beta H}}{\int \mathrm{d}\vec{r} \mathrm{e}^{-\beta H}} = 0.$$

This result indicates that the order parameter is null for any temperature, hence, at all times there will be a disordered phase and both phases (pairs of vortices and individual vortices) are always disordered, that is, there is never a break of symmetry under this transition,

thus contradicting Landau's Phase Transitions theory. The latter is because the Kosterlitz-Thouless Transition is a topological phase transition [15, 16, 18].

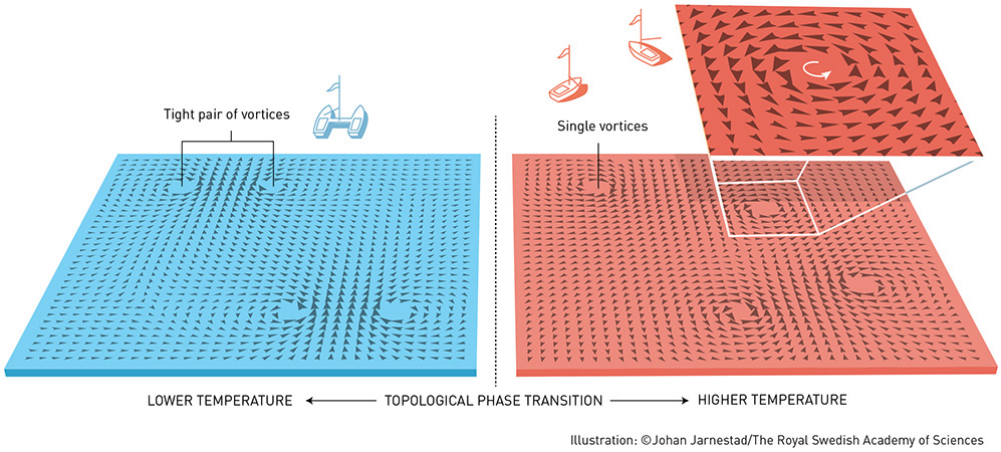

Figure 1.10: Kosterlitz-Thouless transition.

Chapter 2

Umbilical defect dynamics in an inhomogeneous nematic liquid crystal layer

In the context of dilute gases of n-vortices in a homogeneous medium, the interaction between defects is governed by

$$M\dot{\mathbf{r}}_{\mathbf{i}} = \sum_{j\neq \mathrm{i}}^{n} \frac{q_{\mathrm{i}j}}{r_{\mathrm{i}j}} \hat{r}_{\mathrm{i}j}, \qquad \mathrm{i} = \{1, 2, \ldots, n\}, \tag{2.1}$$

where $r_{\mathrm{i}j} \equiv ||\mathbf{r_i} - \mathbf{r_j}||$ is the distance between the ith and jth-vortex, $\hat{r}_{\mathrm{i}j}$ in the unitary vector directed from jth to ith-vortex, and $q_{\mathrm{i}j}$ is the, respective, product of the topological charges of vortices. Hence, the dynamics of a gas of n-vortices corresponds to an overdamped n-body problem. Note that the above set of equations is invariant under the self-similarity transformation

$$\begin{aligned} \mathbf{r_i} &\rightarrow \lambda \mathbf{r_i}, \\ t &\rightarrow \lambda^2 t. \end{aligned} \tag{2.2}$$

Thererfore, if one dilates or expands time and space, using the above scaling, then, the set of Eqs. (2.1) are invariant. We can introduce $N(t)$, the number of vortices at time t, which can be estimated as

$$N(t) = \frac{A}{\langle r \rangle^2}, \tag{2.3}$$

where A is the area of the sample under study, and $\langle r \rangle$ is the average distance between vortices. Because the set of Eqs. (2.1) governs the vortices dynamics, the average distance $\langle r \rangle$ and $N(t)$ are determined by the vortices evolution. Then, $\langle r \rangle$ and $N(t)$ should also be self-similar with transformation (2.2). Hence, $N(\lambda^2 t) = A/\lambda^2 \langle r \rangle^2$. From the previous equality, one infers that the only possibility is that the number of vortices scales as

$$N(t) = \frac{\beta}{t}, \tag{2.4}$$

with β a dimensional constant. Indeed, the number of defects decreases inversely proportional to time, so-called *coarsening law*. Experimentally, this law was, indeed, observed and validated in nematic liquid crystal samples, [11, 19, 20].
We are interested in studying how the coarsening law changes when vortices are induced in an inhomogeneous medium.

2.1 Experimental Setup

To understand the vortex dynamics in an inhomogeneous medium, we have considered a cell of liquid crystal with thickness of 15μm that contains inside glass beads with a random distribution. The LC cell is composed by two Indium Tin Oxide (ITO transparent conductor) coated glass slabs, which are chemically treated to have homeotropic anchoring. Namely, the molecules are anchored to be orthogonal to walls. The glass beads have a diameter of $15\mu m$ and usually, the manufacturer incorporates it to keep the thickness of the cell and avoid buckling. Thus, these glass beads come for default in the most of LC cell. However, the glass beads are not completely monodisperse and perfectly spherical, this will be essential to understand the dynamics of vortices in these media.
The cell described above is filled with MLC-6608 nematic liquid crystal (from Merck) that has a negative dielectric anisotropy. Afterwards, this sample is placed under the microscope (Olympus Bx51) between circular crossed polarizers or linear cross polarizers, and collimated white light from a microscope condenser is sent onto the liquid crystal cell. A sinusoidal voltage $13.5Vpp$, with high-frequency $100Hz$ produced by a function generator (Agilent 33521A) attached to a high voltage amplifier (Tabor Electronics 9200), is applied to the sample. The texture of the liquid crystal generated is captured by a CMOS camera (Thorlabs DCC1645C) which is connected to the microscope. See Figure 2.1.

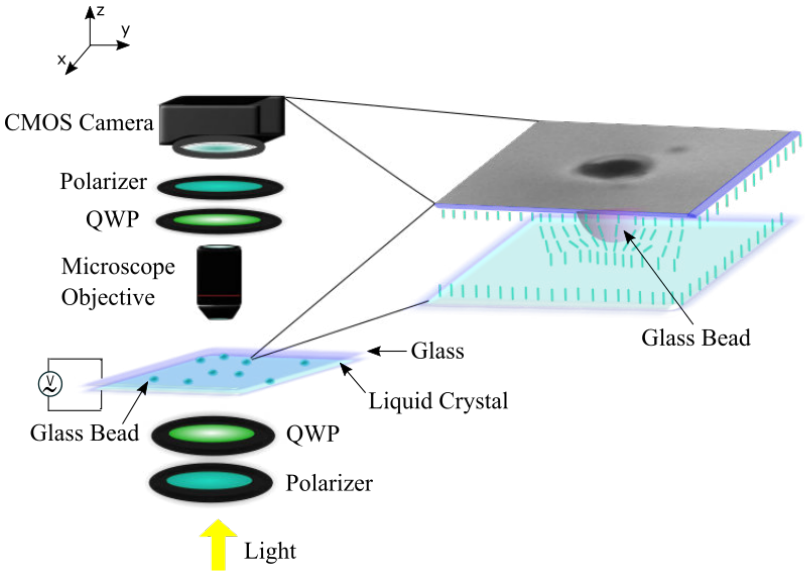

Figure 2.1: Schematic representation of the experimental setup. A nematic liquid cell, with glass beads inside with a random distribution, is inserted between circular cross polarizers in a microscope. A sinusoidal voltage is applied to the sample. Images are captured by a CMOS camera.

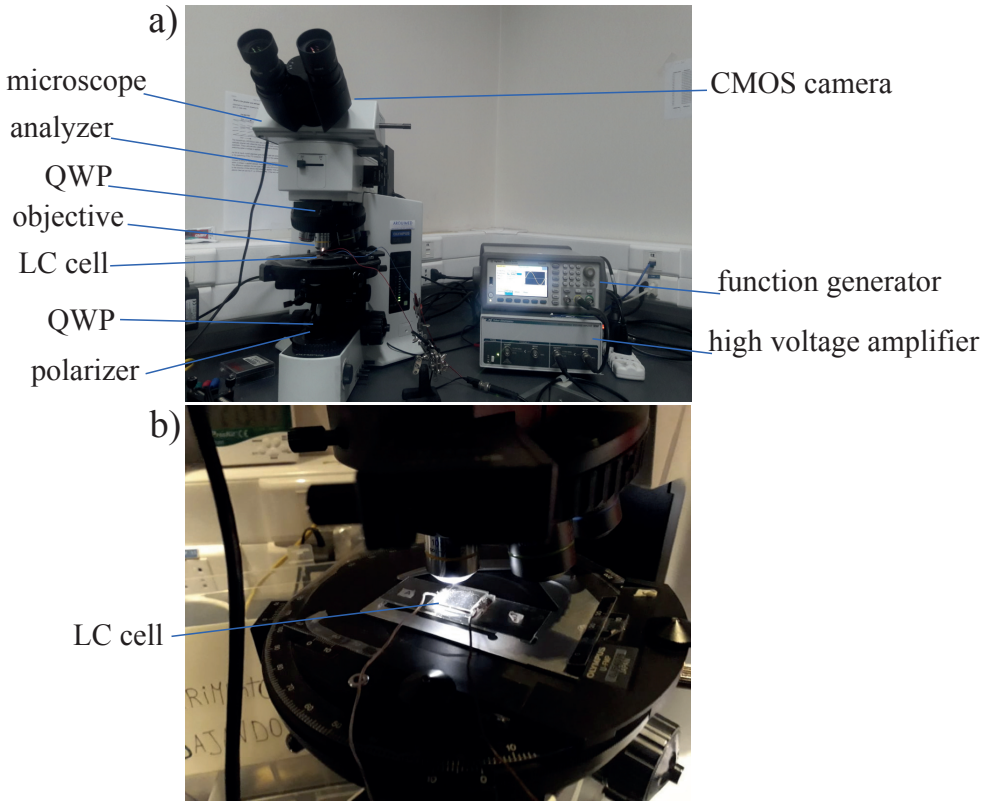

Figure 2.2: Experimental setup. a) Components of the experimental setup. Microscope (Olympus Bx51), polarizer, quarter wave plates QWP (532 nm), nematic liquid crystal cell, objective, analyzer, function generator (Agilent 33521A), high voltage amplifier (Tabor Electronics 9200) and CMOS camera (Thorlabs DCC1645C). Zoom of figure a). Nematic liquid crystal cell on the stage of the microscope.

2.2 Results

When the applied voltage is higher than the Freederickz voltage, the emergence of umbilical defects is observed. These defects appear as a result of inherent fluctuations (thermal and electronics) and then are annihilated with the vortex of opposite topological charge in order to establish the new uniform equilibrium on the sample, this process takes around 20 seconds. Figure 2.3 corresponds to a temporal sequence of snapshots. Figure 2.3 a) the voltage is turned off, Figure 2.3 b) voltage is on and the creation of vortices begins, Figure 2.3 c) formation of vortices, these are given by the interception of four black brushes, Figure 2.3 d) and e) annihilation of vortices with vortices of opposite topological charge, Figure 2.3 f) all vortices have been annihilated.

In order to verified our findings we carried out the experiments under the same conditios with a thicker liquid crystal cells. We observed the same phenomenon with slower dynamics, for instance, under 26 °C, 15 Vpp, and 100 Hz, for a 15 μm thick cell, the coarsening process takes $\sim$20 s and for a 75 μm thick cell, it takes $\sim$ 90 s.

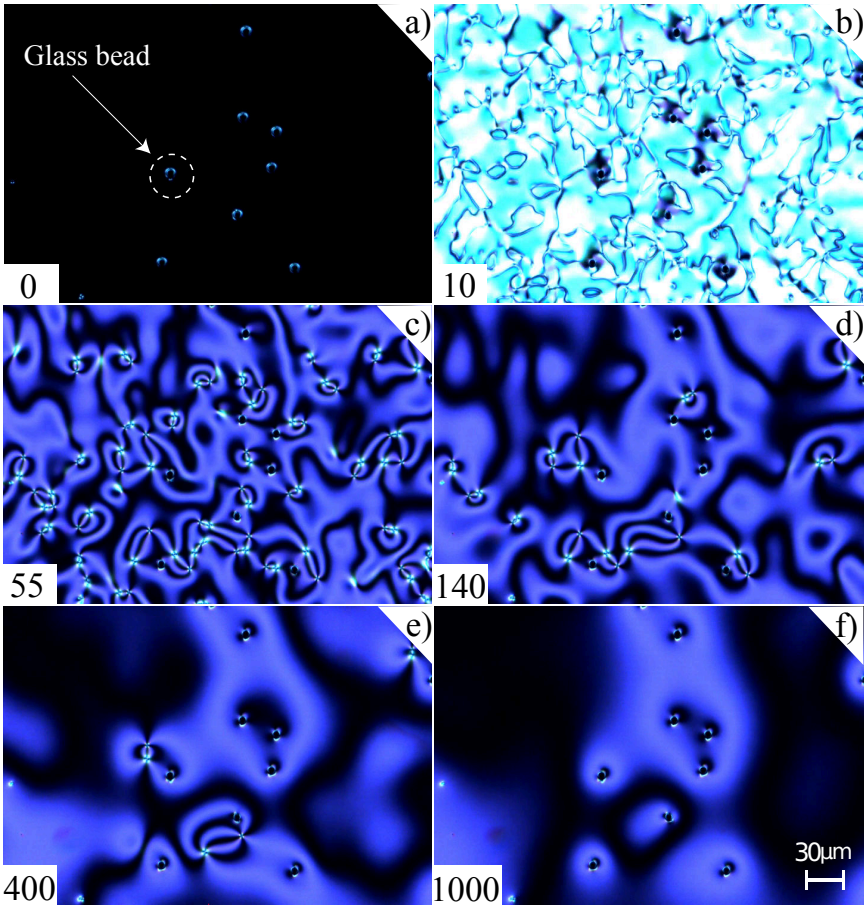

Figure 2.3: Temporal sequence of snapshots depicts umbilical defects dynamics in a non uniform liquid crystal cell. The temporal increment of each frame corresponds to 0.33 s.

To examine the influence of the presence of glass beads on the coarsening process we studied six different regions of the sample with a different random distribution of glass beads in an area 1.43 mm^2. In each one of these regions, a voltage was applied to observe the emergence and annihilation of vortices.
We analyze the images with a particle tracking process, wich allow us to determine the number of vortices an their respective positions. Figure 2.4 c-f) depicts the number of vortices as a function of time for each region of the liquid crystal sample. These results, correspond to the average of 10 realizations. We can observe that the number of vortices decays as a function of time with a power law. Indeed, the coarsening process is persistent under the presence of random glass beads. To determine the exponent of this coarsening process we have considered the following fitting

$$N_f(t) = \beta t^{-\alpha} + N_\infty, \tag{2.5}$$

where N_f corresponds to number of vortices as a function of time, $\{\beta, \alpha, N_\infty\}$ are fitting parameters, which account for the features of the liquid crystal and the cell under study. N_∞ describes the imperfections of the system, which causes the vortices to become trapped in given positions, and the inaccuracy of the recognition method.

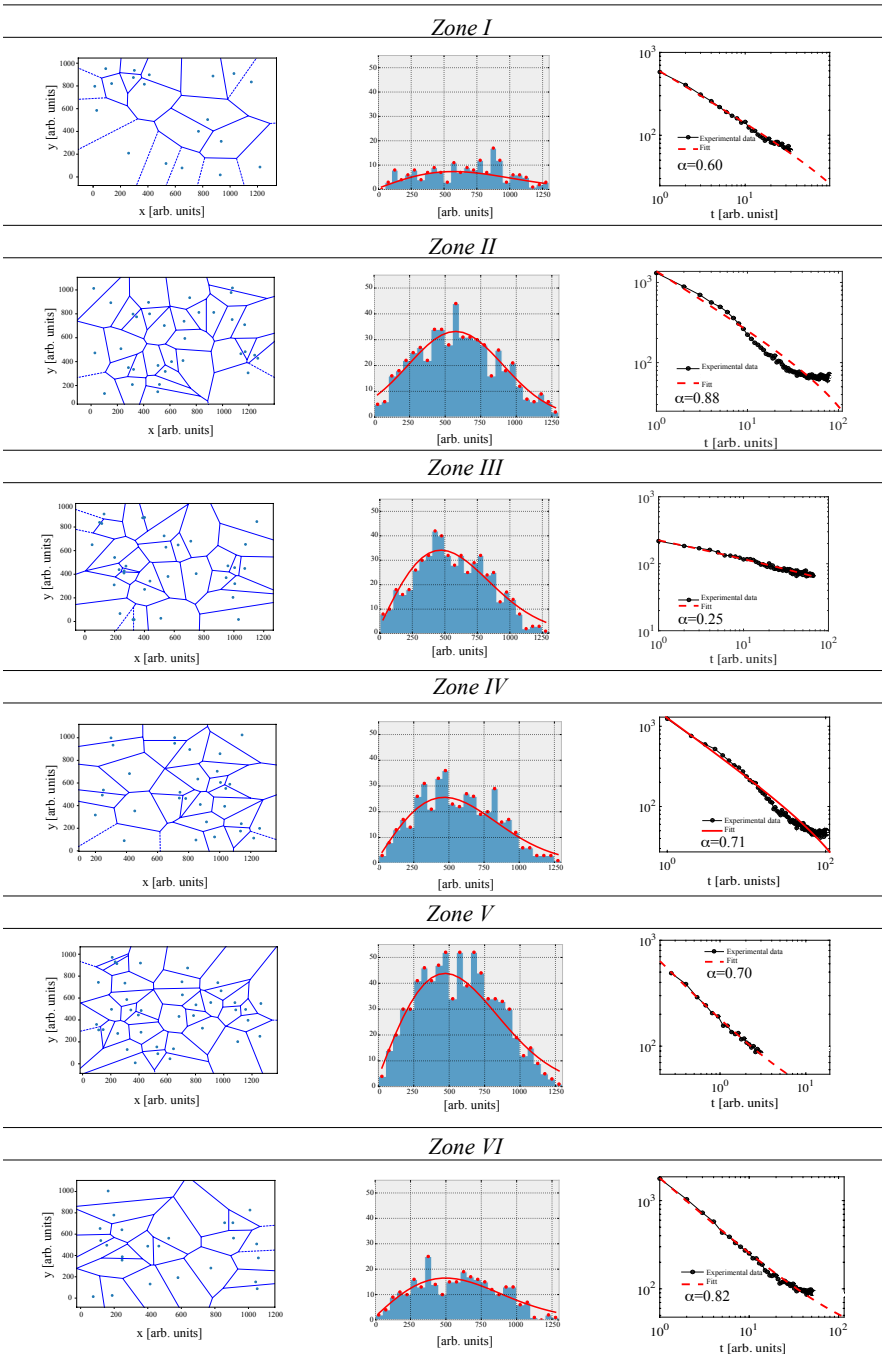

Figure 2.4: Summary of different zones. For each respective region: left panels Voronoi tessellation, center panels distribution of the mutual distance between beads, right panels graphs of the number of vortices as a function of time.

To characterize the clustering and distribution of glass beads, we have computed the Voronoi tessellation [21] of glass beads in different observed zones (see left panels in the Figure 2.4). Center panels in Figure 2.4 correspond to respective histogram of the bead mutual distance on each observation zone, the red solid line is a fitting curve using a Raleigh distribution. Right panels in Figure 2.4 show the temporal evolution of number of vortices

in the studied region.
To quantify the disorder of the distribution of glass beads in each region, we use the Shannon Entropy [22]

$$S = -\sum_{\mathrm{i}=1}^{N_t} P_{\mathrm{i}} \log(P_{\mathrm{i}}), \tag{2.6}$$

Where P_{i} is given by

$$P_{\mathrm{i}} = \frac{f_{\mathrm{i}}}{N_t^2}, \tag{2.7}$$

Where f_{i} is the number of times that the distance between two spheres has a value $\mathrm{i}x + \Delta x$, and N_t corresponds to the total number of distances between glass beads.

Zone	Density $[mm^2]$	α	β	N_∞	Entropy
I	13.630	0.60	604.2	12.85	0.0210
II	17.217	0.88	1782.0	20.33	0.0136
III	20.803	0.25	246.4	22.44	0.00767
IV	21.521	0.71	1285.0	17.87	0.0091
V	23.673	0.70	1404.0	25.74	0.00772
VI	27.977	0.82	162.7	18.09	0.0057

Table 2.1: Results of the measured beads density, computed fitting exponents, and entropy over an area of approximately 1.394 mm^2 on different observation zones.

Table 2.1 summarizes our results for different zones of observation in the liquid crystal cell. Different coarsening laws are obtained over different zones. Unfortunatelly it is not possible to establish a correlation between the density of spheres, coarsening exponents α, and entropy. This is due to our experimental observation that there are spheres that attract vortices which affects the coarsening process. Also, glass spheres do not all behave the same, and even between the attractive ones, they do not behave completely the same. Therefore, the coarsening process is more complexed, influenced by both the distribution of spheres and the interaction between spheres and vortices.

2.3 Defects dynamics in presence of a glass beads

The presence of the glass spheres generates a deformation of the nematic director on the contour of the sphere. Depending on the shape of the beads they can act as localized potentials on the generated defects. Then, we have found attractive and non-attractive glass beads. Figure 2.5 *a*) shows a temporal sequence of snapshots of the behavior of vortices in presence of an attractive glass bead. Unexpectedly, we can observe that positive and negative vortices are attracted by the glass bead. Each topological charge is attracted by a certain region of the bead and then it disappears. In Fig. 2.5 *b*) red dashed points depict the trajectory of positive and negative vortices respectively in presence of an attractive glass bead. Here, initially, we can see vortices move close to the white straight line that joins vortices. Then, at the initial time, vortex interaction is stronger than vortex-beads interaction. However, later time, when the umbilical defects are close to the glass bead, their trajectories are deflected and reoriented towards the center of the bead.

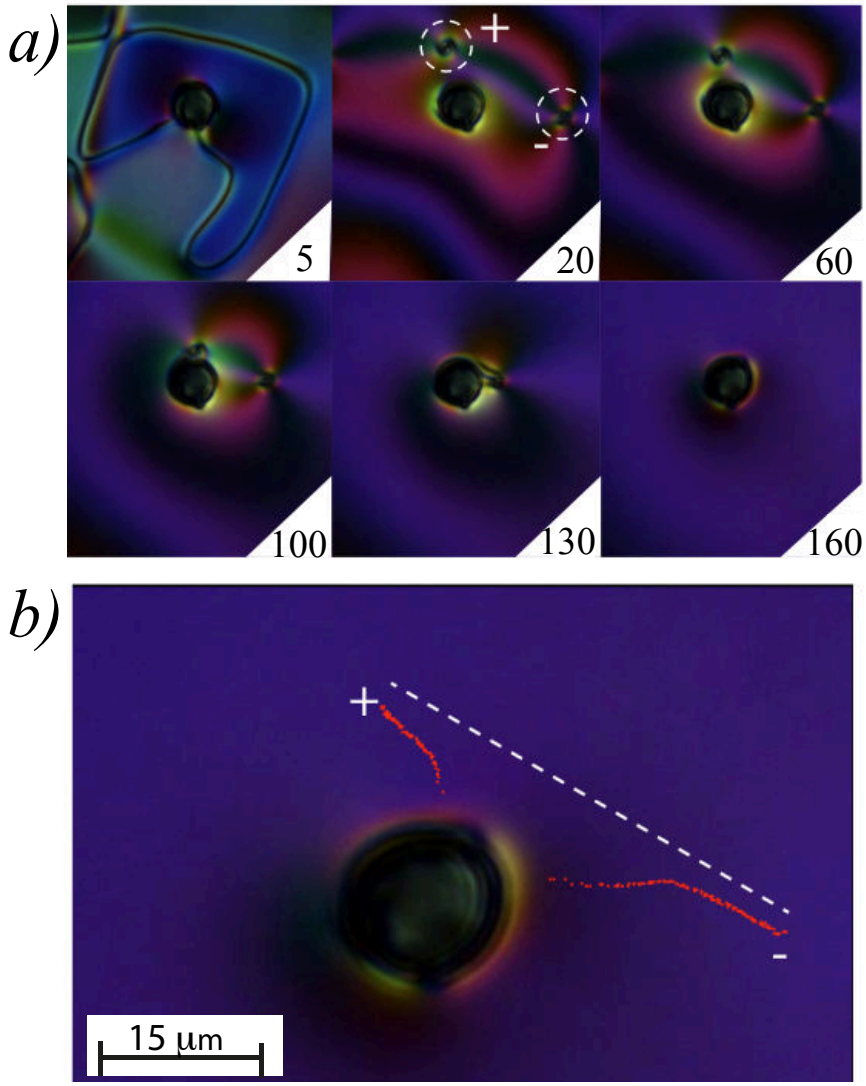

Figure 2.5: Evolution of a vortex pair in presence of an attractive glass bead. (a) Sequences of temporal snapshots. The bottom numbers in each panel account for the respective frame. The temporal increment of each frame corresponds to 0.07 s. Umbilical defects of a positive (circular shape) and negative (square shape) charge under circular crossed polarizers are recognized and monitored. The dashed circles account for the umbilical defects. (b) Trajectory of the vortices: the dashed points (red) indicate the trajectory of defects, the dashed straight line accounts for the initial distance between defects.

An attractive bead was chosen to be studied. When the voltage is applied, the vortices that are attracted by the bead were tracked its position where they collide with the glass bead. To distinguish the topological charge of vortices, circular linear cross polarizers were used. This procedure was repeated 50 times. Figure 2.6 shows the regions of the glass sphere where attract positive and negative vortices. Red and blue points correspond to positive and negative vortices. We can infer that the attractive sphere has a quadrupolar behavior, that is, the glass bead is characterized by having four poles. Therefore, the vortices of a given charge prefer to collide in certain regions of the bead. Note, that the observed poles are not

symmetric, which is a manifestation that dipolar terms are also relevant in the interactions.

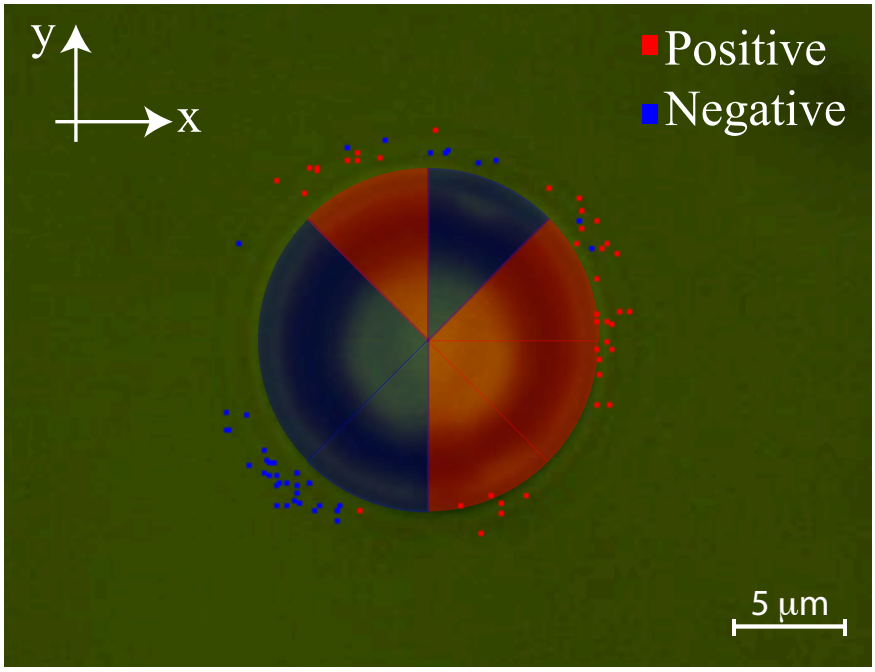

Figure 2.6: Behavior of an attractive bead. Each point represent the position where a vortex collides with the bead. Red points correspond to positive vortices and blue points correspond to negative vortices.

It is known that glass beads without surface treatment, generate homeotropic anchoring at their boundaries, that is, the liquid crystal molecules tend to be oriented normal to the surface of the glass bead [23, 24]. In addition, since the glass bead is in contact with the glass plates of the sample, a Saturn ring like defect loop appears around each glass inclusion [23,24]. Figure 2.7 shows a schematic representation of the director field lines induced by a perfect spherical glass bead and a slightly deformed bead. When the glass bead is perfectly spherical, it generates a defect at its center which has a skyrmion type structure, which is canceled with the equivalent charge caused by the Saturn ring. In Figure 2.7, the induced charge is represented by a central point (blue) and the Saturn ring by a closed curve (green). Therefore, perfectly spherical glass beads cause a net charge to cancel out, that is, the equivalent charge of the Saturn ring is equal to the charge induced at the center. Then, these glass beads do not attracting vortices, therefore, we name them *passive beads*. In contrast, deformed glass beads generate equivalent multipolar charges (dipoles, quadrupole, and so forth), which are overall neutral but affect the local dynamics of their surroundings. These glass beads with multipolar charges are characterized by attracting and annihilating vortices and we name them *active beads*.

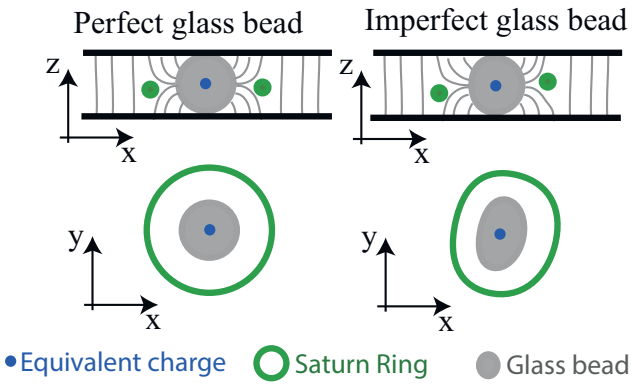

Figure 2.7: Schematic representation of the director field lines induced by a perfect spherical bead (left panel) and a slightly deformed bead (right panel). Upper and lower panels show a side and top view of the correspondingly induced defects.

We can identify experimentally these glass beads with multipolar charges. Without the applied voltage to the sample under cross-polarization, the perfect and imperfect glass beads generate either perfect rings or deformed curves of light, respectively as a consequence of the Saturn ring deformation. Figure 2.8 shows three glass beads with and without voltage, where one can identify the deformed glass bead (central). Only this central glass bead attracts vortices.

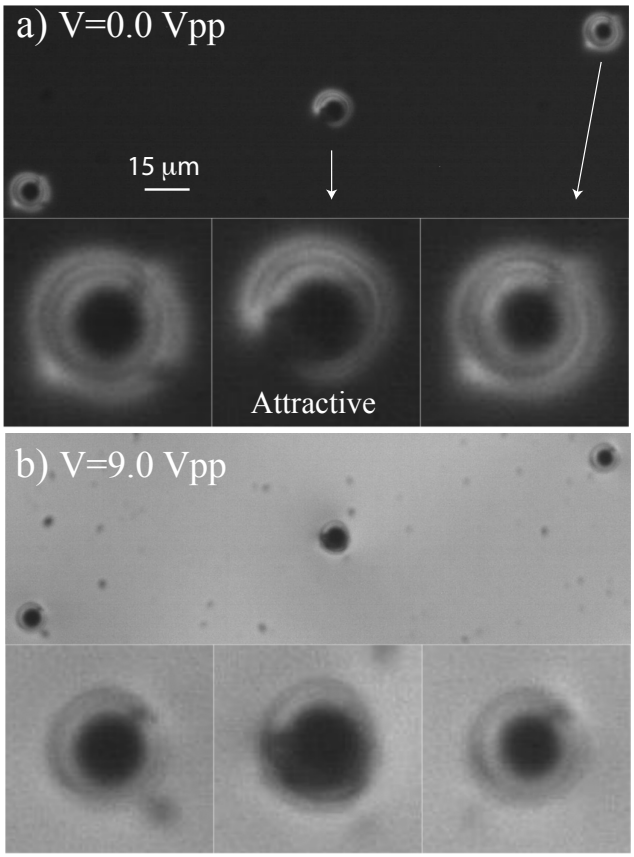

Figure 2.8: Glass beads in nematic liquid crystal cell.The central sphere corresponds to an attractive beads. a) voltage is turned off b) Voltage is turned on.

In summary, in the liquid crystal cell, we found perfect and non-perfect spherical beads. Perfect spherical glass beads, which are the majority in the sample, do not attract or repel umbilical defects. In non- perfect spherical glass beads, where its equivalent charge and the Saturn ring charge do not coincide, a multipolar charge that interacts with the topological defects is generated.

Theoretical description of attractive beads

The interaction between an imperfect glass beads and a vortex can be modeled by

$$M\dot{\mathbf{r}} = q\left[\frac{\vec{\mathrm{d}}}{\|\mathbf{r}\|^2} - \frac{\vec{\mathrm{d}}\cdot\mathbf{r}}{\|\mathbf{r}\|^4}\mathbf{r}\right] + q\left[\frac{\vec{l}^2}{\|\mathbf{r}\|^4}\mathbf{r} + \frac{2\vec{l}(\vec{l}\cdot\mathbf{r})}{\|\mathbf{r}\|^4}\right], \tag{2.8}$$

Where $\mathbf{r}(t)$ is the vector between the glass bead and the vortex positions, $\|\mathbf{r}\|$ is the magnitude of the vector $\vec{r}$, $\vec{\mathrm{d}}$ is a vector that characterizes the dipolar interaction, q is the topological charge of the interacting vortex, $\vec{l}$ is a vector that characterizes the quadrupolar interaction, and M stands for the vortex mobility, which depends on the size of the system, the properties of the liquid crystal and the applied voltage. Note that the vectors $\vec{l}$ and $\vec{\mathrm{d}}$ are not necessary parallel. On the right-hand-side of equation (2.8), the first and second parenthesis terms account, respectively, for the dipolar and quadrupolar interaction. Note that the dipolar and quadrupole interaction decay proportional to the square inverse and the cubic inverse of the distance between the vortices and the beads, respectively.
Experimentally, from Figure 2.6, it is possible to deduce that the quadrupole interaction is more dominant in the interaction, that means $\|\vec{\mathrm{d}}\| \ll \|\vec{l}\|$.

Let us consider a vortex gas in the presence of randomly distributed beads, for simplicity, we consider that glas beads are dominantly dipolar. The interaction is described by

$$M\dot{\mathbf{r}}_{\mathrm{i}} = \sum_{j}^{N-1} \frac{q_{\mathrm{i}j}}{\|\mathbf{r}_{\mathrm{i}} - \mathbf{r}_j\|^2}(\mathbf{r}_{\mathrm{i}} - \mathbf{r}_j) + \sum_{k=1}^{N'}\left[\frac{Q_{\mathrm{i}k}\vec{\mathrm{d}_k}}{\|\mathbf{r}_{\mathrm{i}} - \mathbf{l}_k\|^2} - \frac{Q_{\mathrm{i}k}[(\mathbf{r}_{\mathrm{i}} - \mathbf{l}_k)\cdot\vec{\mathrm{d}_k}]}{\|\mathbf{r}_{\mathrm{i}} - \mathbf{l}_k\|^4}(\mathbf{r}_{\mathrm{i}} - \mathbf{l}_k)\right] \tag{2.9}$$

where $\mathbf{r_i}$ stands for the position of i-th vortex (cf. Fig. 2.9), M is the vortex mobility, $q_{\mathrm{i}j}$ is the product of the topological charges of the i-th and j-th vortex, $Q_{\mathrm{i}k}$ is the intensity of the interaction between the vortices, N and N' account for the number of vortices and beads and the k-th bead, $\mathbf{l_k}$ and $\vec{\mathrm{d}}_k$ are the vector position and the dipolar vector of k-th glass bead, respectively.

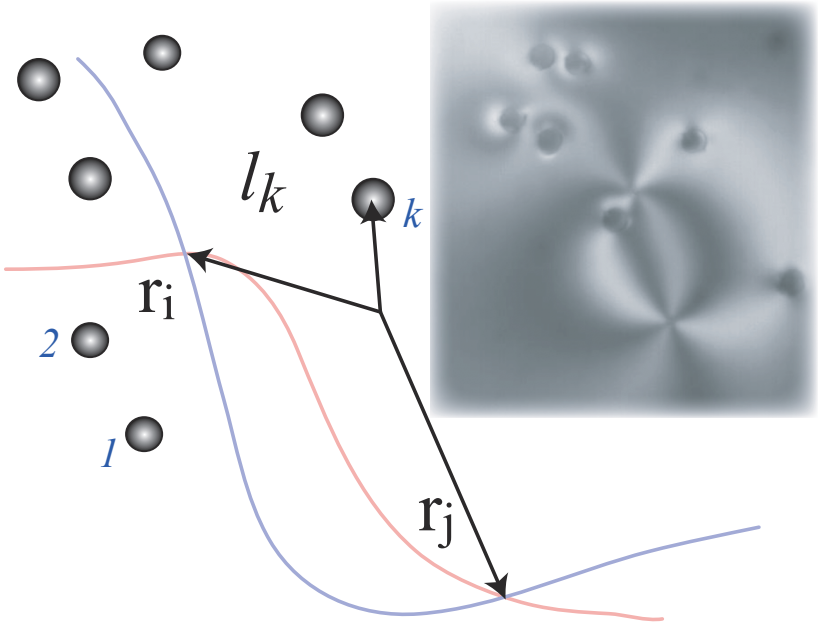

Figure 2.9: Schematic representation of a vortex pair in presence glass beads. $\mathbf{r}_\mathrm{i}$ and $\mathbf{r}_j$ correspond to positions of i-th and j-th vortices respectively. $\mathbf{l}_k$ is the position of k-th glass beads.

Let us consider the limit of diluted vortices, that is, the distance between vortices $r \approx ||\mathbf{r_i} - \mathbf{r_j}||$ is much greater than the distance between a vortex and glass beads surrounding it ($||\mathbf{r_i} - \mathbf{r_j}| \gg ||\mathbf{r_i} - \mathbf{l_k}||$). Hence, the nearby glass beads dominate the dynamics of vortices, that is,

$$M\dot{\mathbf{r}}_\mathbf{i} \approx \sum_{k=1}^{N'} \frac{Q_{ik}}{||\mathbf{r_i} - \mathbf{l_k}||^2}\vec{\mathrm{d}}_k + \sum_{k=1}^{N'} \frac{Q_{ik}(\mathbf{r_i} - \mathbf{l_k}) \cdot \vec{\mathrm{d}}_k}{||\mathbf{r_i} - \mathbf{l_k}||^4}(\mathbf{r_i} - \mathbf{l_k}). \tag{2.10}$$

In this limit, the dynamics of the vortices is not self-similar, however when performing the transformation of spatial and temporal dilation

$$\begin{aligned} \mathbf{r_i} &\to \lambda \mathbf{r_i}, \\ t &\to \lambda^3 t. \end{aligned} \tag{2.11}$$

equation (2.10) takes the form

$$M\dot{\mathbf{r}}_\mathbf{i} \approx \sum_{k=1}^{N'} \frac{Q_{ik}\vec{\mathrm{d}}_k}{||\mathbf{r_i} - \frac{\mathbf{l_k}}{\lambda}||^2} + \sum_{k=1}^{N'} \frac{Q_{ik}(\mathbf{r_i} - \frac{\mathbf{l_k}}{\lambda}) \cdot \vec{\mathrm{d}}_k}{||\mathbf{r_i} - \frac{\mathbf{l_k}}{\lambda}||^4} \left(\mathbf{r_i} - \frac{\mathbf{l_k}}{\lambda}\right). \tag{2.12}$$

The coarsening process is governed for large times and distances; therefore one can consider λ to be large ($\lambda \gg 1$). Then, the above equation is rewritten

$$M\dot{\mathbf{r}}_\mathbf{i} \approx \sum_{k=1}^{N'} \frac{Q_{ik}\vec{\mathrm{d}}_k}{||\mathbf{r_i}||^2} + \sum_{k=1}^{N'} Q_{ik}\frac{\mathbf{r_i} \cdot \vec{\mathrm{d}}_k}{||\mathbf{r_i}||^4}\mathbf{r_i} + O\left(\frac{1}{\lambda}\right), \tag{2.13}$$

so that, if one dilates space and time on large scales, the equivalent set of Eqs. (2.1) are invariant at the dominant order. Furthermore, the vortex gas in such a disordered medium satisfies an effective dynamics governed by the previous interaction law.

As we mentioned before, the number of vortices at time t has the form $N(t) = A/\langle r\rangle^2$, where A is the area of the sample under study and $\langle r\rangle$ is the average distance between vortices. Then, $\langle r\rangle$ and $N(t)$ should also be self-similar with the transformation (2.11). Hence, $N(\lambda^3 t) = A/\lambda^2\langle r\rangle^2$. Thus, we obtain

$$N(t) = \frac{\beta_0}{t^{2/3}}, \tag{2.14}$$

where β_0 is a constant. In this case, the number of defects decreases following a $-2/3$ power law. Experimentally, several zones show exponents close to $-2/3$ (see Table I). Note that all the investigated zones, with the exception zone III, show an exponent within 20 % error from the theoretical prediction. However, the dynamics of submerged vortices in an environment full of spacers with various imperfections is much more complicated, as illustrated by the experimental results, and a full agreement over all the investigated zones could not be reached.

In conclusion Nematic liquid crystals layer with negative dielectric constant and homeotropic anchoring under the influence of a voltage are the ideal context for studying the interaction of gas of topological vortices with opposite topological charges. One expects the dynamics of the vortices being characterized by a decreasing number in time, which follows a power law with critical exponent $\alpha = 1$ because the dominant interaction between the vortices is self-similar. Unexpectedly, we observe that this dynamics is persistent in thin cells of nematic liquid crystals that contain glass beads as spacers. However, the laws of the exponential decay in the number of vortices depend strongly on the distribution of the glass beads and their imperfections. Experimentally, we have characterized such a dynamics and demonstrated that the deformed glass beads attract vortices of opposite topological charges, presenting mainly a quadrupolar behavior. Theoretically, we have derived the modified power law for inhomogeneous samples, leading to $\alpha = 2/3$ exponent of the power law. The agreement with the exponents derived from the experimental observations is satisfactory over several zones of the analyzed samples. However, a complete agreement could not be reached because of the diversity of the beads and the consequent complexity of the induced vortex dynamics.

Chapter 3

Topological transitions at room temperature in nematic liquid crystal cell out of equilibrium

Matter in thermodynamic equilibrium can exhibit exotic states of matter corresponding to topological transitions, which are associated with the emergence of pairs of vortices called Berezinskii-Kosterlitz-Thouless transitions [15, 16]. This phenomenon has been observed in various contexts such as Josephson junctions [25], superconducting films [26], among others. Unlike the usual states of matter such as solid, liquid, gas, and plasma, these exotic phases correspond to the permanent emergence and self-organization of topological states.

The topological transitions of matter were discovered at the beginning of the 70s by Berezinskii [18], Kosterlitz and Thouless [16], who showed that a low dimensional system described by a physical vector order parameter in thermodynamic equilibrium undergoes a transition from a homogeneous state without vorticity, to a state in which vorticity pairs persist. Then, vortices creation and annihilation processes are, respectively, due to thermal fluctuations and free energy minimization [27], hence at the critical temperature at which they are balanced, the systems undergoes a topological transition [16, 18].
Topological equilibrium transitions usually occur at temperatures below ambient temperature, for example, helium becomes superconducting at 4 K and some ceramics achieve this transition at approximately 200 K [3].

All these physical systems under study share the property of having a parameter of complex or tensor order. An ideal physical system that contains the qualities to be described by a complex order parameter and that can be studied in almost two dimensions are thin films in liquid crystals [2]. Thus, we are interested in the study of topological transitions in nematic liquid crystal in a system out of equilibrium, that is, in a system with injection and dissipation of energy.

3.1 Experimental Setup

To investigate topological states of matter in an out of equillibrium system, let us consider experimentally a nematic liquid crystal cell, which consists of a cell 5B100A150UT180, manufactured by Instec with 15 μm of thickness that contain glass beads as spacers. The cell is filled by capillarity with MLC-6608 (Merck) nematic liquid crystal that has negative anisotropy dielectric constant ($\varepsilon_a = -4.2$ at room temperature), and the molecules of liquid crystal are orthogonally aligned to the cell plates (homeotropic conditions). An external electric field is applied in the vertical direction (z-axis) using sinusoidal, square, and sawtooth voltages with amplitude 15 Vpp, and with low frequency (fraction of Hertz). This voltage is produced by a function generator (Agilent 33521A) together with a high voltage amplifier (Tabor Electronics 9200). The imaging system used is an Olympus BX51 microscope equipped with linear cross polarizers. The light from the microscope condenser illuminates the cell mounted on the microscope stage, and a CMOS camera (Thorlabs DCC1645C) is used to capture and monitor images. Figure 3.1a shows a schematic representation of the experimental setup under consideration. For studying thermal effects, we have used a microscope (Leica DM2700 P) equipped with a thermal control microscope stage (Linkam LTS420).

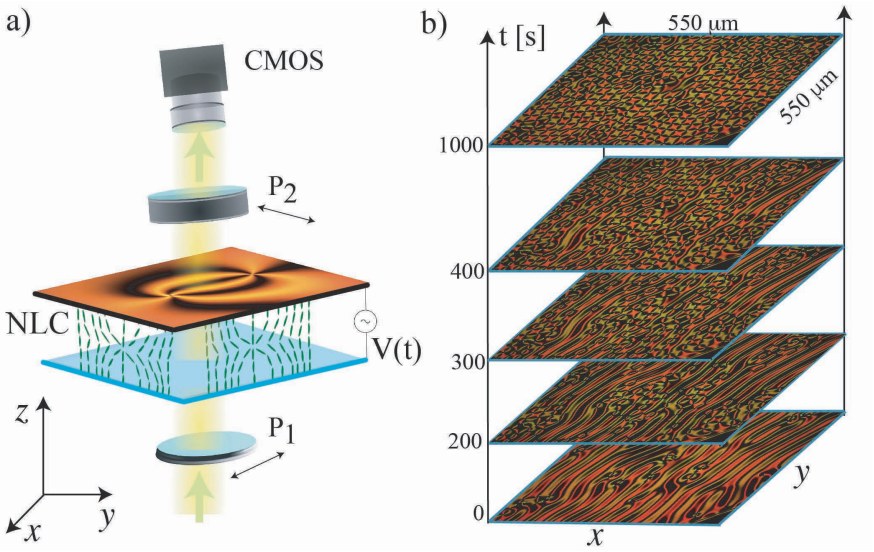

Figure 3.1: Nematic liquid crystal cell under a temporarily modulated potential exhibits creation and self-organisation of vortices. a) Schematic representation of the experimental setup. Nematic liquid crystal cell (NLC) is illuminated by white light between two crossed polarizers (P_1 and P_2). The horizontal snapshot shows a pair of vortices with opposite topological charges. b) The temporal sequence of snapshots in the region of self-organized vortices, using a pure tone voltage signal at frequency 0.335 Hz and voltage amplitude 13.5 Vpp.

3.2 Results

It has been demonstrated that applying a high frequency voltage to the sample leads to the generation of vortices with random positions and their subsequent annihilation which finally results in a homogeneous non-vortex state system [1, 2]. Therefore, the presence of vortices in liquid crystals is only a transient phenomenon.

Surprisingly, when the frequency of the applied voltage to the sample decreases to a fraction of Hertz, we observe a creation of a substantial amount of vortices that do not annihilate, and as the final state they form a vortices lattice with fixed positions, as shown in 3.1 b). Also, when a voltage with low frequency is applied with other signal shape, like for examples sawtooth and square, appears persistent vortices with random positions.

In brief, we have found that there is a critical frequency f_c at which the system exhibits a topological transitions from non-vortex state to persistent vortex state.

Figure 3.2 a) shows the average number of vortices as a function of frequency counted stroboscopically in each oscillation cycle with the standard deviation determined along the way, it is obtained when a sawtooth voltage is applied to the sample. From this graph it is possible to deduce that this transitions corresponds to a supercritical bifurcation. For frequencies lower than a critical frequency f_c, the number of vortices becomes permanent over time and we note that as the frequency decreases the number of vortices increases up to a particular critical value, and subsequently decreases monotonically until it vanishes at low frequencies, which is a manifestation of a sort of resonance at f_r for the process of creation and annihilation of topological defects.

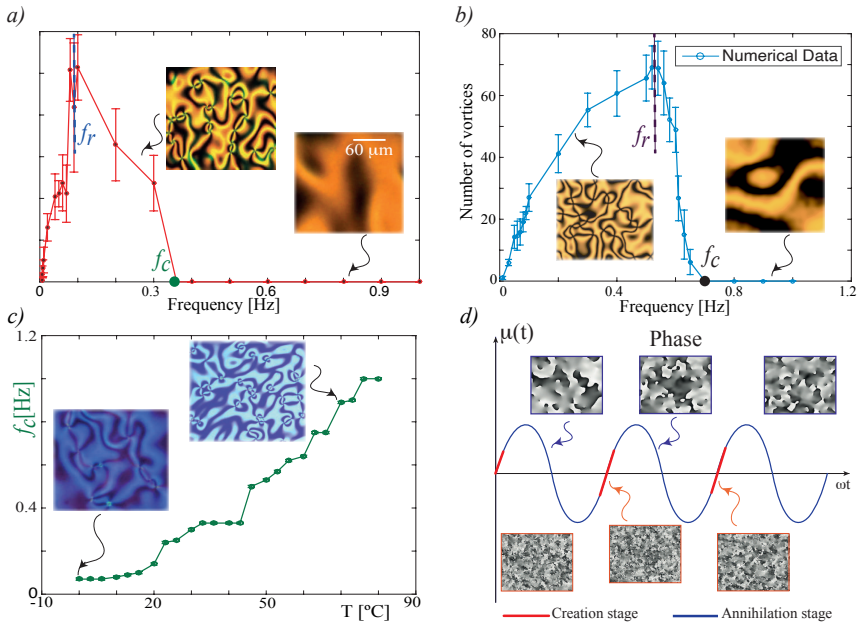

Figure 3.2: Bifurcation diagram of topological transition out of equilibrium a) experimental, and b) numerical using model Eq. (1). The experimental bifurcation diagram is obtained with a sawtooth forcing with an amplitude of 15 Vpp. c) Critical frequency $f_c(T)$ as a function of temperature. This curve was acquired thanks to a thermal controller microscope stage. The insets account for the respective snapshots at different temperatures. d) Evolution of the temporal bifurcation parameter $\mu(t)$ and characterization of the regimes of creation (red curve) and interaction (blue curve) of vortices.

Through the use of a thermal control microscope, the temperature of the nematic liquid crystal cell was changed and adequately controlled in a range between $-10°$C and $80°$C. Our temperature dependant measurements show that the critical frequency f_c monotonically increases upon rising of temperature, as illustrated in Figure3.2 c). Therefore, the topological transition induced by temporal voltage modulation is observed throughout the mesophase stability range of the nematic liquid crystal under study.

Theoretical description

To understand the origin of this topological transition out of equilibrium, we have considered modeling the Ginzburg-Landau equation with real coefficients since as it is known, this amplitude equation describes vortex solutions in nematic liquid crystal layers with external electric or magnetic forcing and homeotropic boundary conditions [9], allowing to explain the process of interaction and annihilation of vortices subject to a constant electric field and temperature [27]. For this reason, this equation is the ideal to be modeled in order to describe the topological transition found.
To account for the additional ingredients of the observed topological transition, we must incorporate the oscillatory nature of the electrical voltage applied to the liquid crystal sample, and include the inherent fluctuations due to temperature. This leads to the stochastic real Ginzburg-Landau equation with oscillatory coefficients, that is,

$$\partial_t A = [\mu_0 + \gamma \cos(2\pi f t)]\, A - |A|^2 A + \nabla^2 A + \sqrt{T}\zeta(\vec{r}, t), \tag{3.1}$$

where $A(\vec{r}, t)$ is a complex order parameter, t and $\vec{r}$ describe time and the coordinate vector that characterizes the thin film, μ_o is the uniform bifurcation parameter, which accounts for the balance between the elastic and electric force, γ and f are the amplitude and the frequency of the forcing, respectively. The function $\mu(t) = \mu_0 + \gamma \cos(2\pi f t)$ is the temporal modulated bifurcation parameter. ∇^2 denotes the usual Laplace operator. The constant T accounts for the thermal and electronics fluctuations intensity level and $\zeta(\vec{r}, t)$ is a white noise of zero mean value, $\langle \zeta(\vec{r}, t) \rangle = 0$, and no spatial or temporal memory. Namely, the stochastic term has the spatiotemporal correlation $\langle \zeta(\vec{r}, t)\zeta(\vec{r}', t') \rangle = \delta(\vec{r} - \vec{r}')\delta(t - t')$.
We note that in the high-frequency regime, this model becomes the real Ginzburg-Landau equation with real coefficients, where the vortices do not persist and the annihilation of defects of opposite charges dominates their the creation.
Numerical simulations of this model (3.1) were implemented using a finite differences code with Runge-Kutta order-4 algorithm, with a 200×200 points grid, spacing $\mathrm{d}x = 0.5$, and temporal increment $\mathrm{d}t = 0.02$. The stochastic noise $\zeta(\vec{r}, t)$ is generated through the Box-Muller transform of a uniform random number generator.

Figure 3.2b) shows this happening for frequency values up to order one. In this regimen, the number of vortices on average is zero. By decreasing the frequency further to a critical value f_c, the average number of vortices stabilizes over time. The topological transition obtained numerically using Eq. (3.1) has a qualitative behavior similar to that observed experimentally, see top panels in Figure 3.2. Notice that as the frequency decreases ($f < f_c$) the number of vortices increases up to a particular critical value and subsequently decreases monotonically until it vanishes at low frequencies, which manifests an excellent qualitative

agreement with the experimental observations. Hence, experimentally and numerically a sort of resonance is observed for the process of creation and destruction of topological defects.

These numerical simulations also allow us to identify the location of the vortices through $\pm 2\pi$ jumps of the phase of the amplitude. When comparing the evolution of the system and the profile of the bifurcation parameter function $\mu(t)$ two characteristic regions are identified. Creation of vortices happens in the intervals of time where $\mu(t)$ is small and growing (red curve in Figure 3.2d)), these vortices later interact even when $\mu(t) < 0$ (blue curve in Figure 3.2d). The vortex creation time interval decreases as the forcing frequency increases and for high frequencies the creation process is inefficient. The persistence of vortices is a consequence of the balance between the processes of creation (stochastic) and their interaction (deterministic) as it is illustrated in Figure 3.2 d).

Topological transition with harmonic driven forcing

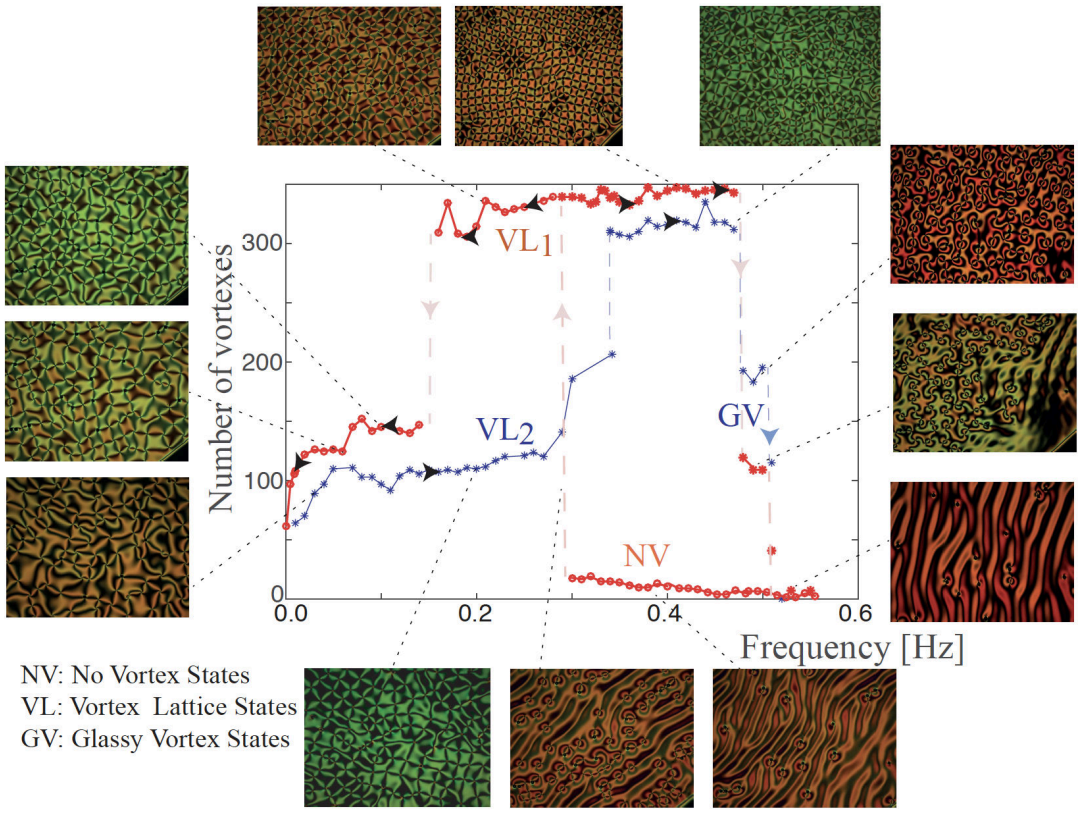

Figure 3.3: Experimental bifurcation diagram of topological transition out of equilibrium under harmonic forcing. The liquid crystal cell exhibits three states: no-vortex (NV), vortex lattice (VL) and glassy vortex (GV) states. The arrows indicate the direction of increase or decrease of the voltage. The insets show snapshots in the respective parameter ranges.

When we studied this topological transition with a harmonic signal of voltage, we found surprisingly, that there are different topological transitions with a rich morphology of structures of vortices, we have detected a discontinuous transition from non-vortex state to lattice vortex

state. Figure 3.3 shows a square vortex lattice, with persistent positions, and its respective bifurcation diagram corresponding to the out of equilibrium counterpart of Abrikosov lattice [28]. We note that the vortex lattice in not hexagonal like the one of Abrikosov, as a consequence of the asymmetry between the opposite charges [9]. When we decrease the frequency, the square lattice undergoes a subcritical bifurcation leading to a square lattice of higher wavelength (see Fig. 3.3). Similar lattice is observed by means of thermal gradient [29] or by doping with ionic impurity [30], which induces charge motions.

Increasing the frequency further the square lattice transitions to a glassy state (cf. Fig.3.3), in which the vortex structure has parametric positions in each period of the signal. For even higher frequencies the system returns to the no-vortex state.

Therefore, Figure 3.3 summarizes the complexity of the topological transitions in the liquid crystal cell maintained out of equilibrium at room temperature. We speculate that the origin of the periodic structures we have discovered may be associated with the interaction between the vortices, the excitation of stationary waves [31] and charge movements. The latter is because The application of a low-frequency electric field induces charge movements due to the weak anisotropic conductivity of the liquid crystal [1]. The accumulation of charges can induce a molecular reorientation, Carr-Helfrich mechanism [1, 32, 33], which in turn modifies the interaction between umbilical defects and can even generate a lattice arrangement of them [29]. However, precise understanding of this phenomena is yet an open problem.

The origin of the square vortex lattice is probably associated with the coupling of elastic deformations, fluid modes and charge dynamics. To describe qualitatively of this coupling, we include in the model Eq. (3.1) inertia and anisotropic effects, that is, a second temporal derivative of amplitude A.

$$\partial_{tt}A + \lambda\partial_t A = \left[\mu_0 + \gamma\cos(2\pi f t)\right] A - |A|^2 A + \nabla^2 A + \delta\partial_{\eta,\eta}\bar{A} + \sqrt{T}\zeta(\vec{r},t), \qquad (3.2)$$

where λ accounts for the rotational viscosity, δ stands for the difference of elastic constants [5, 9, 34, 35], the operator $\partial_{\eta,\eta} = \partial_{xx} - \partial_{yy} + 2i\partial_{xy}$ describes the asymmetric coupling, and $\bar{A}$ is the complex conjugate of A. Simulations of this model show the emergence of a square lattice, as seen in Figure 3.4.

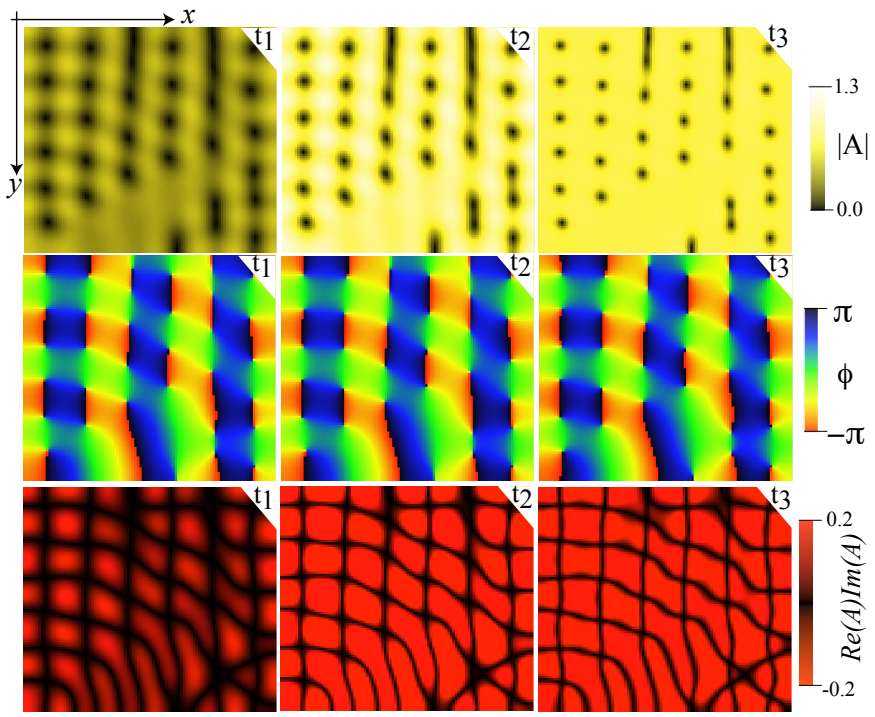

Figure 3.4: Numerical square vortex lattice. Temporal sequence ($t_1 < t_2 < t_3$) of the amplitude module $|A|$, phase $\phi = \arctan[\mathrm{Im}(A)/\,\mathrm{Re}(A)]$, and polarization field $\mathrm{Re}(A)\,\mathrm{Im}(A)$ of model Eq. (2) with inertia and anisotropic coupling over a period, given by $\mu_0 = 0.6$, $T = 0.03$, $\lambda = 1.4$, $\delta = 0.3$, $\gamma = 3$, and $f = 0.1$.

Homogeneous cell

These topological transitions were found in the first instance using a nematic liquid crystal cell, with 15 μm of thickness, that by default had randomly distributed glass spheres (the same cell from Chapter 2). To confirm that the presence of the spheres does not influence the formation of these topological transitions, we have performed the experiments in a homogeneous cell, with 75 μm of thickness, filled with the same liquid crystal used in the previous experiment.

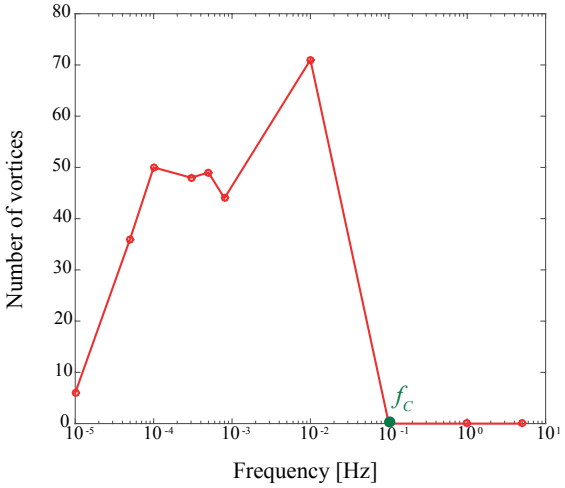

Figure 3.5: Number of votex in function of frequency for a homogeneous nematic liquid crystal cell with 75 μm of thickness.

Figure 3.5 shows the number of vortices that appear as a function of frequency for a homogeneous liquid crystal cell with a thickness of 75 μm. In this graph, it is observed that when the frequency is 0.01 Hz there is a topological transition from a non-vortex state to a lattice vortex state, as seen in Figure 3.6. Note that the conditions under which this topological transition occurs are different from the conditions under which occurs in the cell 15 μm thick. This is because as the cell is thicker, there are more molecules and since only the border molecules are anchored, for the rest of them it is easier to move and couple, so, less voltage and frequency are required to observe this topological transition.

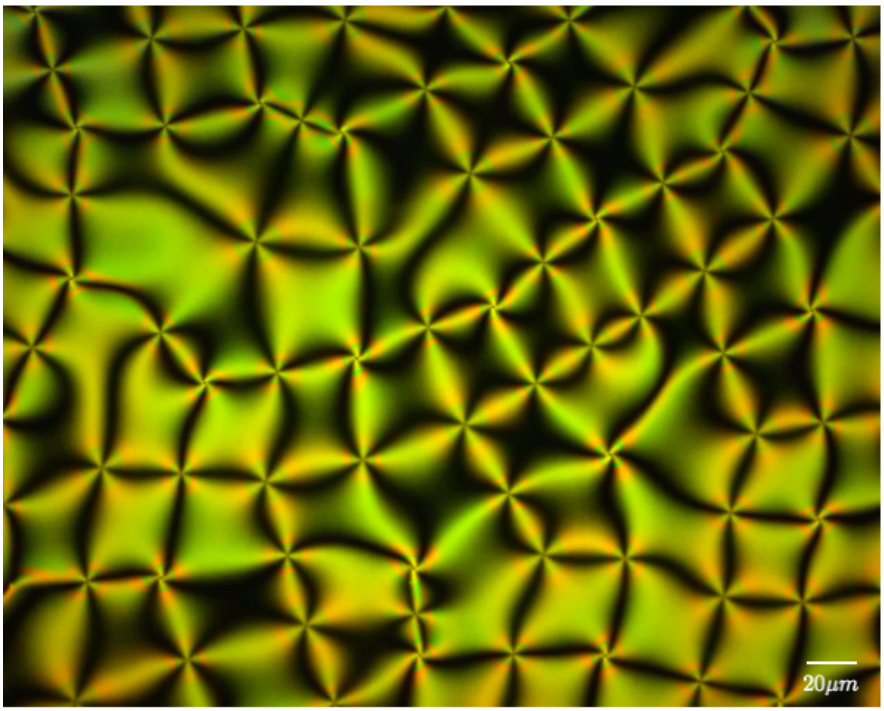

Figure 3.6: Vortex lattice observed in a 75 μm thick homogeneous cell when a sinusoidal voltage of 9 Vpp with a frequency of 0.01 Hz is applied to the sample.

In conclusion, we observed out of equillibrium topological transitions in a nematic liquid crystal cell, under suitable experimental contidions. Depending on the frequency and type of forcing, harmonic, sawtooth, or square profiles, the vortices self-organize forming square lattices, glassy states and disordered vortex structures. An stocastic real Ginzburg Landau equation can described qualitatively well this phenomenon and could be a start point for undestanding and controlling the exotic states of matter. Because vortex lattices emerge spontaneously in single cells subjected to alternative low-frequency voltages, it opens up the possibility of new and fresh applications of the generation of optical vortices.

Chapter 4

Magnetic ring induced vortex triplet in a liquid crystal layer

Vortices are particle-type solutions with topological charge that can steer the dynamics in various physical systems. A paradigmatic model that presents vortices is the Ginzburg-Landau Equation [8,36]. This amplitude equation has been used to describe fluids, superfluids, superconductors, liquid crystals, granular matter, magnetic media, and optical dielectrics, among others [8, 36–38].
As mentioned in previous chapters, the generation of vortices in liquid crystals is obtained when a sinusoidal voltage is applied to a nematic liquid crystal cell with negative dielectric anisotropy susceptibility and homeotropic anchoring on the walls. Depending on the frequency of the applied voltage, a disordered vortices gas or self-organized structures of vortices is obtained. A relevant interest that has emerged in recent years, is the development of mechanisms that allow inducing and manipulating vortices that can be a source of optical vortices or optical tweezers. These mechanisms are established through optical vortices beam [39–42]. Also, one can induce umbilical defects employing intense light beams [43], photo-sensitive walls [10, 41], or by means of external magnetic and electric fields [44, 45]. Recently, the combined action of a distant magnetic ring with a uniform electric field into the nematic cell enables the self-engineering of macroscopic q-plate [45]. With the aim of figuring out the mechanism of the induction of stable localized vortices in nematic liquid crystals by electric and magnetic fields, we have conducted an experimental and theoretical study that is detailed below.

4.1 Experimental Setup

To study vortices induced by electric and magnetic fields, we consider a cell composed by two thin glass layers separated by a thickness of d = 75 μm, which is chemically treated on its interior walls to have a homogeneous homeotropic anchoring and with transparent electrodes included (indium oxide and tin, ITO). This cell has been filled by capillarity with a nematic liquid crystal LC-BYVA-01-5G (Instec) with negative dielectric anisotropy susceptibility $\varepsilon_a = -4.89$, birefringence $\Delta n = n_e - n_o = 0.1$, rotation viscosity $\gamma = 204$ mPas, splay and bend elastic constant, respectively, $K_1 = 17.65$ pN and $K_3 = 21.39$ pN, and

negative magnetic anisotropy χ_a (not yet measured).

A neodymium magnetic ring of 3200 G with a rectangular transversal section, outer radio $R_{out} = 7$ mm, internal $R_{in} = 2$ mm, and thickness of $h = 5$ mm is placed onto the top of the nematic liquid crystal cell (cf. Fig. 4.1). The sample with the magnetic ring is introduced in an Olympus Bx51 microscope and it is positioned between two linear crossed polarizers. A sinusoidal voltage of intensity $V_0 = 7.95$ Vpp, near to the reorientation transition, *Fréederickz voltage* $V_{FT} = 6.57$ Vpp, with a frequency of $\omega = 100$Hz is applied to the sample. The system is illuminated by a white light (Halogen lamp). The temporal evolution of the liquid crystal cell under the simultaneous effects of the electric and magnetic field is monitored by a CMOS camera (Thorlabs DCC1645C), which allows us to observe the central zone of the magnetic ring. All experiments were performed at room temperature of 21°C.

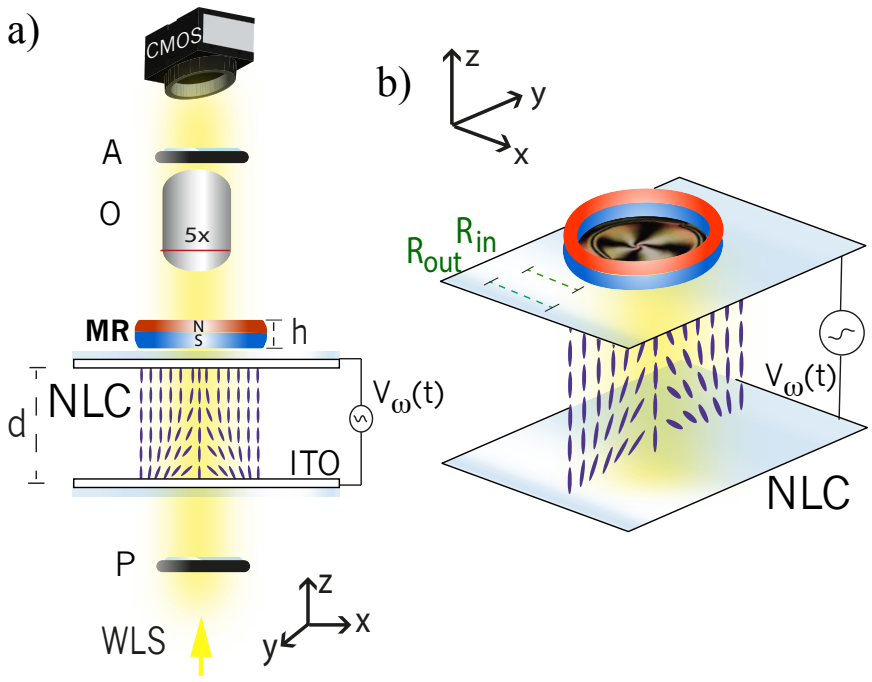

Figure 4.1: Schematic representation of the experimental setup. (a) Vertical description of the experimental setup. NLC accounts for the nematic liquid crystal cell, d is the thickness of the cell, ITO accounts for the transparent electrode (indium oxide and tin), $V_\omega(t)$ is a harmonic voltage applied to the liquid crystal layer, where ω is the voltage frequency, MR is the magnetic ring of thickness h and internal and outer radius R_{in} and R_{out}, WLS is the white light source, P and A stand for polarizers, which are crossed, O accounts for the objective and CMOS is the complementary metal-oxide-semiconductor camera. The rods represent the average direction of molecules, directors. (b) Three-dimensional schematic representation of the liquid crystal cell under the influence of the electric and magnetic fields.

4.2 Results

Molecular Reorientation

When the voltage is off, the liquid crystal sample is only subject to the influence of the magnetic field and we observed that there is no transmission of light. This is because the torque generated by the magnetic field is very weak, so it is not capable of overcoming the elastic resistance of the material. Therefore, the magnetic ring is not capable of generating molecular reorientation by itself. Namely, the configuration of molecules can not exhibit birefringence effect. To generate the molecular reorientation in the liquid crystal (see Fig. 4.3)) it is necessary to include the application a sinusoidal voltage to the sample.
We observe that when the liquid crystal cell without an applied magnetic field, the molecular reorientation voltage is 6.28 Vpp, when the magnet is placed above the cell, the molecular reorientation occurs at 4.09 Vpp. Therefore, this reorientation is observed at voltages lower than Freederickz voltage (critical voltage for instability of reorientation purely induced by an electric field), it is due to negative electrical anisotropy and the presence of electric and magnetic field. We observed that as the magnetic field intensity increases the molecular reorientation occurs at lower voltages as shown in Figure 4.2.

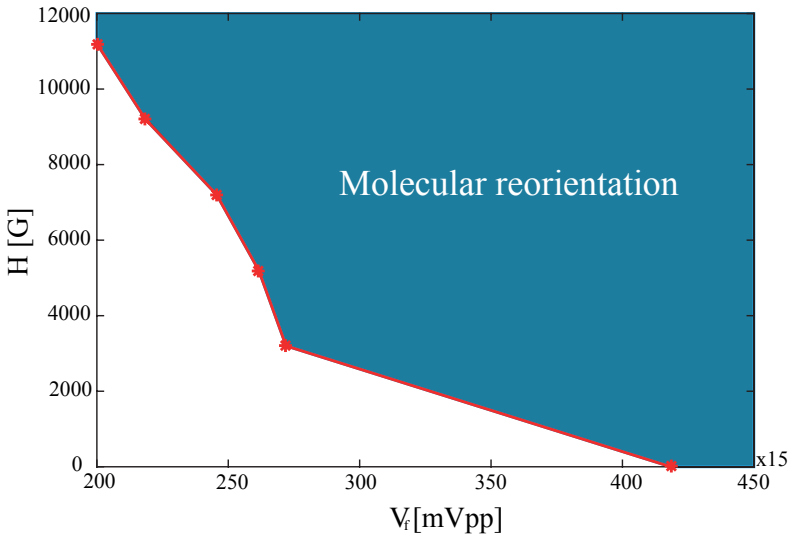

Figure 4.2: Curve of molecular reorientation transition, magnetic intensity H v/s molecular reorientation voltage Vf.

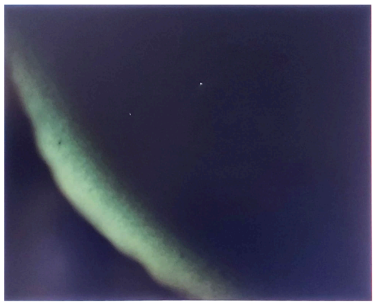

Figure 4.3: Beginning of molecular reorientation in nematic liquid crystal cell.

Appearance of the vortex triplet

After the magnet is placed above the nematic liquid crystal cell, the voltage is applied and the molecular reorientation is observed at 4.08 Vpp, the voltage begins to increase, observing what is shown in Figure 4.3. That is, in the external region the light is transmitted, which is a manifestation of molecular reorientation.
When the voltage begins to increase, at 5.25 Vpp, a black circle is observed as shown in Figure 4.4, as the voltage increases more, the molecules continue to change their orientation, and we observed a black cross with the fairly wide center and the appearence of a surrounding black ring, this structure corresponds to a vortex with a thick core. Further increase of voltage above 6.30 Vpp, results in thining out of the ring. Two vortices of opposite charges begin to appear in the antipodes of the ring. Notice that, this type of vortex corresponds to Rayleigh vortex recently predicted [46]. Continuing, at 6.90 Vpp, a triplet of vortices is observed. This structure is composed of a vortex of positive topological charge at the center, and two vortices of opposite charges on the ring. It is observed that together with increasing the voltage the core of the vortices become smaller. At 7.95 Vpp, it is observed that the arms of the center vortex begin to swirl and their cores undergo a small rotation (see Figure 4.4). We note that this induced vortex triplet is observed to remain stable and its total topological charge is +1.

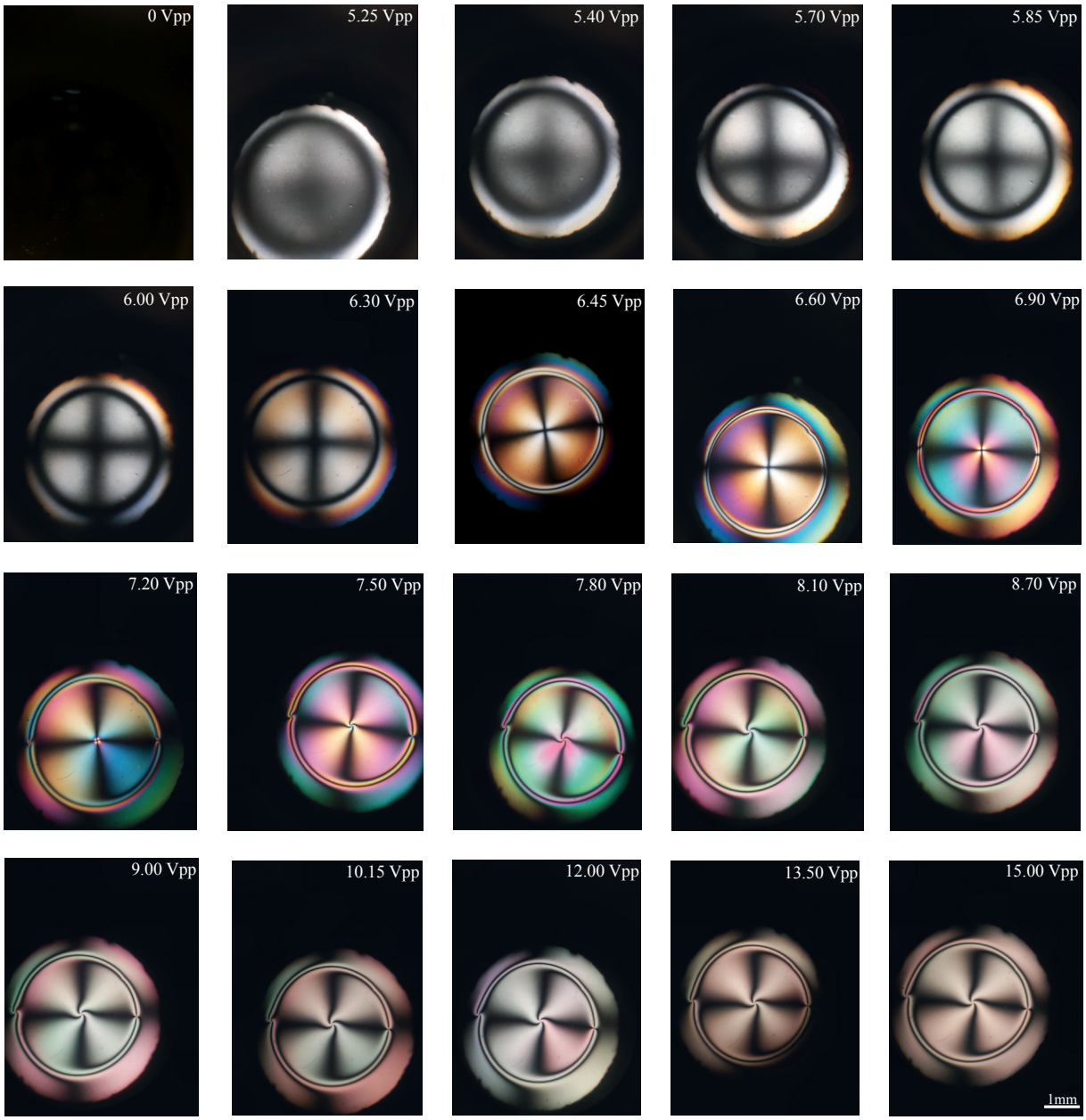

Figure 4.4: Topological transition induced by the combination of magnetic and electric field. Snapshots of nematic liquid crystal under the influence of electric and magnetic field for different voltage values. It is observed that when the voltage increases, a stable vortex triplet is created.

When the voltage is turned off and then is turned on to 7.95 Vpp with a frequency of 100 Hz, the creation of the vortex triplet is also observed and this structure remains stable as shown in Figure 4.5. When the voltage is off and then is turned on at 15 Vpp with a frequency of 100 Hz, the creation of a vortex at the center with a surrounding ring with several vortices (on the order of 10) is initially observed. After a time, vortices that are on the ring begin to annihilate themselves with their opposite topological charges, finally leaving two vortices of

opposite topological charge located on the antipodes of the ring. Thereby, the stable vortex triplet is obtained again as is shown in Figure 4.6.

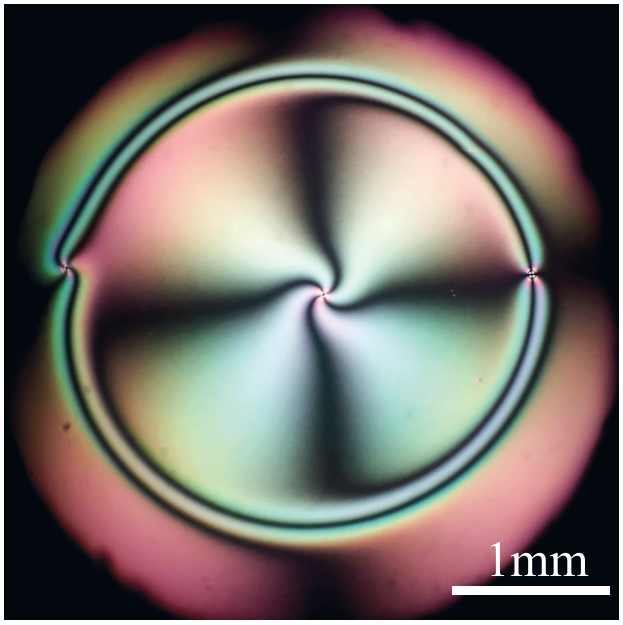

Figure 4.5: Snapshot of the vortex triplet observed above the orientational transition $V_0 = 7.95$ Vpp.

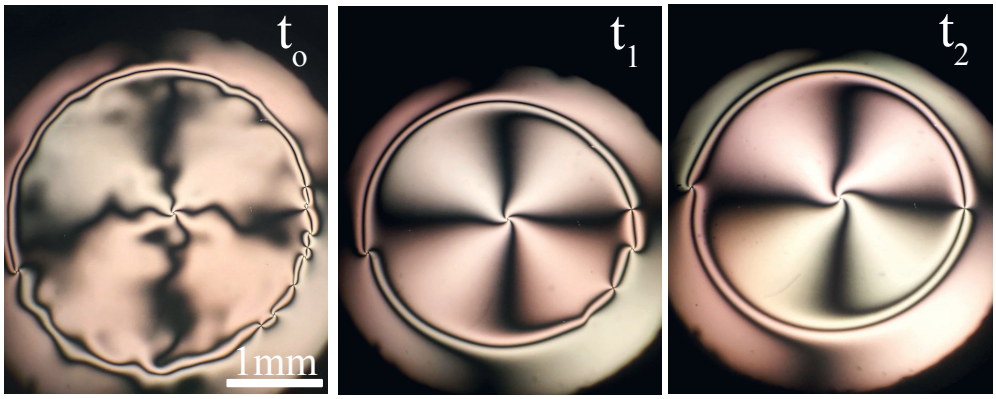

Figure 4.6: Temporal sequence of snapshots of the emergence of vortex triplet formation $t_0 < t_1 < t_2$, far from the orientational transition $V_0 = 15.0$ Vpp.

Likewise, for low voltage, Figure 4.7 shows a temporal sequence of formation of a vortex triplet from the state voltage is off at t=0 s the voltage is turned on to 6.9 Vpp. Here, we can see the immediate appearance of a black cross with a surrounding black ring, as in Figure 4.4, and as time evolves this structure converges in a vortex triplet.

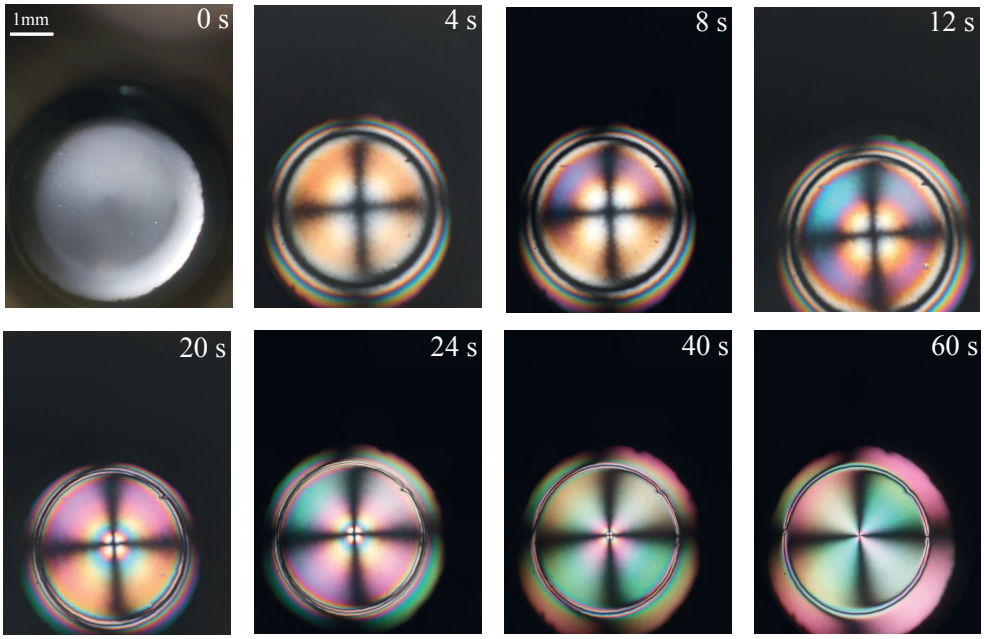

Figure 4.7: Temporal sequence of snapshots of the emergence of vortex triplet formation for 6.9 Vpp.

Using Fiji, an image analysis software (`https://imagej.net/Fiji`), profiles of the vortices corresponding to the vortex triplet were extracted as shown in Figure 4.8.

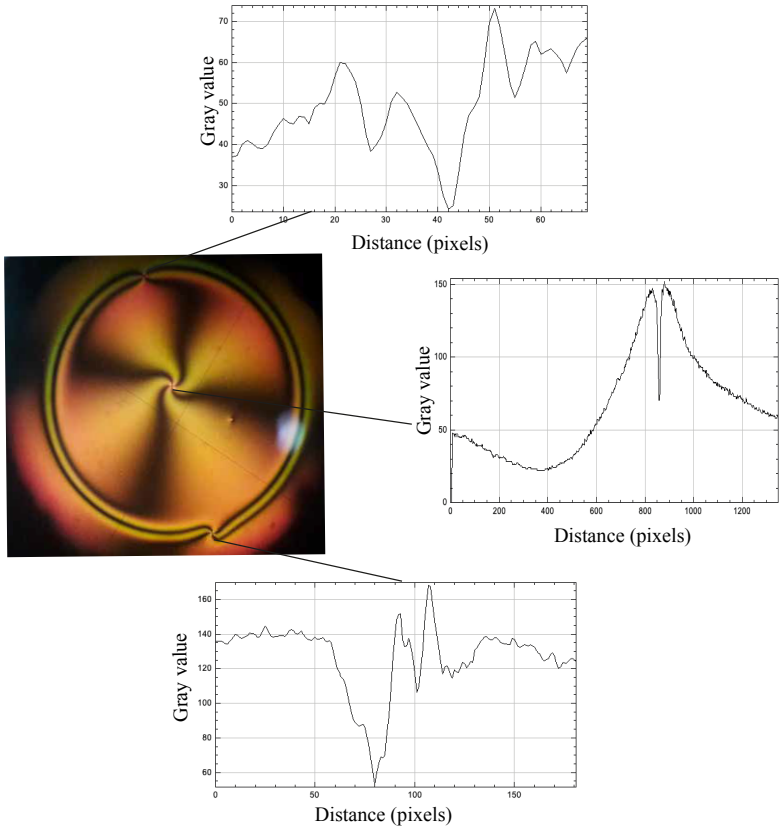

Figure 4.8: Profiles of a vortex triplet.

4.3 Intuitive description

The induced vortex triplet is determined by the structure of the magnetic field generated by the magnetic ring. Since the magnet has a north and south pole parallel to the liquid crystal sample and a rectangular cross-section, then a magnetic protuberance is observed at the center of the ring [47]. Figure 4.9 shows the magnetic structure of a ring with a rectangular cross-section schematically. Dashed curves account for the magnetic protuberance. This magnetic protuberance is a consequence of the boundary condition imposed by the inner wall of the ring on the magnetic field. Liquid crystal molecules tend to orient orthogonal respect to the magnetic field as a consequence of the negative anisotropic magnetic susceptibility [1, 2]. When considering the liquid crystal sample inside the magnetic protuberance, it naturally induces a positive vortex at the center and also a circular defect line that circumscribes the vortex (cf. Fig. 4.9b). However, for homeotropic anchoring conditions, a defect line is unstable and always stabilizes in a set of vortices with alternating charges along the line [1, 2]. Indeed, one expects this line to stabilize in vortices and, ultimately, only a few vortices to survive along the line. Observe that when the sample stands outside the magnetic protuberance, one only observes a single vortex, and there is no ring to circumscribe it [45]. Indeed, this can be accomplished by moving the liquid crystal sample away from the magnet.

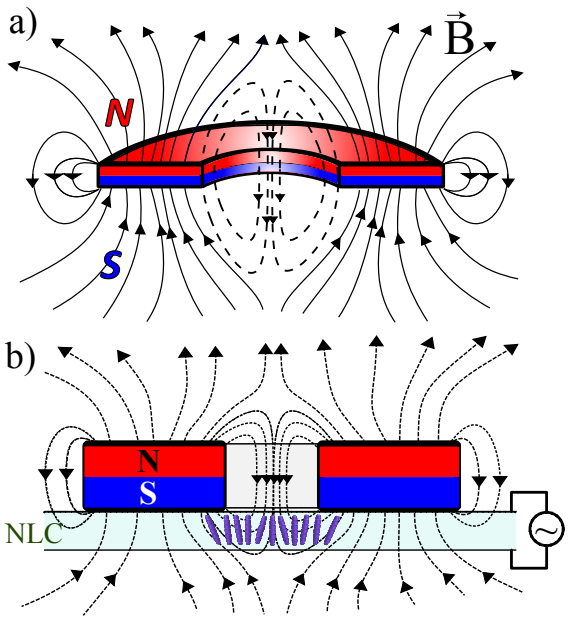

Figure 4.9: Schematic representation of the magnetic field structure of a magnetic ring with a rectangular cross-section. a) Three-dimensional representation of the magnetic field. The curves account for the lines of the magnetic field. Dashed lines account for the structure of the magnetic field within the magnetic protuberance. b) Two-dimensional representation of the magnetic field of the ring onto the nematic liquid crystal layer. The rods stand for the average direction of molecules.

4.4 Theoretical description

To develop a theoretical description The structure of the magnetic protuberance can be modeled in a first approximation by the magnetic field of a cylindrical magnet of the form

$$\vec{B}(\rho,\theta,z) = \frac{m}{4\pi}\left[\frac{(3z^2-\sigma)\hat{z}}{(\rho^2+z^2)^{5/2}} - \frac{\hat{z}-3z\rho\hat{\rho}}{(\rho^2+z^2)^{3/2}}\right], \tag{4.1}$$

where $\sigma > 0$ is a phenomenological parameter that accounts for geometric features of the magnet ring, $\sigma(R_{in}, R_{out}, h)$, m is a constant that has a dimension of permeability per magnetic moment, and $\{z, \rho\}$ are the cylindrical coordinates. Note that the origin of the coordinate is fixed at the center of the magnetic ring. Note that, due to azimuth anisotropy of the ring, the magnetic field does not depend on the θ coordinate.

To describe the mechanism of creation and pinning of vortices, we derive a model in the vicinity of the reorientational transition, a limit where analytical results are accessible, as nematic liquid crystal molecules are weakly tilted from the longitudinal axis $\hat{z}$ and backflow effects can be neglected [1, 10, 41]. The molecular reorientation of the liquid crystal is described by the director vector $\vec{n}$ when the temperature is constant [1,2]. The dynamic of the

director $\vec{n}$ is characterized by minimizing the Frank-Ossen free energy, which corresponds to

$$\begin{aligned}\mathcal{F} \quad &= \int \mathrm{d}V \Bigg\{ \frac{K_1}{2}(\nabla\cdot\vec{n})^2 + \frac{K_2}{2}(\vec{n}\cdot(\nabla\times\vec{n}))^2 + \\ &\frac{K_3}{2}(\vec{n}\times(\nabla\times\vec{n}))^2 - \frac{\varepsilon_a}{2}(\vec{E}\cdot\vec{n})^2 - \frac{\chi_a}{2}(\vec{B}\cdot\vec{n})^2 \Bigg\},\end{aligned} \tag{4.2}$$

where $\{K_1, K_2, K_3\}$ are the liquid crystal elastic constants, $\vec{E}$, and $\vec{B}$ are the electric and magnetic field, respectively [1, 2]. We consider a uniform vertical electric field $\vec{E} = E_z\hat{z} = V_\omega(t)/\mathrm{d}\ \hat{z}$ and a magnetic field $\vec{B} = B_z\hat{z} + B_\rho\hat{\rho}$ given by formula (4.1). Applying The Euler-Lagrange equations

$$\frac{\delta\mathcal{R}}{\delta\dot{\vec{n}}} = -\frac{\delta\mathcal{F}}{\delta\vec{n}} = \gamma\partial_t\vec{n} \tag{4.3}$$

with the restriction $\vec{n}\cdot\vec{n} = 1$ and $\mathcal{R} = \frac{\gamma}{2}|\vec{n}|^2$, where γ is the LC rotational viscosity. Then, we obtain

$$\begin{aligned}\gamma\partial_t\vec{n} = \quad & K_3[\nabla^2\vec{n} - \vec{n}(\vec{n}\cdot\nabla^2\vec{n})] \\ & +(K_3 - K_1)[\vec{n}(\vec{n}\cdot\nabla)(\nabla\cdot\vec{n} - \nabla(\vec{n}\cdot\nabla))] \\ + \quad & 2(K_2 - K_3)\{(\vec{n}\cdot\nabla\times\vec{n})[\vec{n}(\vec{n}\cdot\nabla\times\vec{n}) - \nabla\times\vec{n}] \\ + \quad & \vec{n}\times\nabla(\vec{n}\cdot\nabla\times\vec{n})\} - \varepsilon_a(\vec{n}\cdot\vec{E}[\vec{E} - \vec{n}(\vec{n}\cdot\vec{E})]) \\ - \quad & \chi_a(\vec{n}\cdot\vec{B}[\vec{B} - \vec{n}(\vec{n}\cdot\vec{B})]).\end{aligned} \tag{4.4}$$

To study the dynamics of the director, we consider, close to the reorientational instability, the following ansatz

$$\vec{n} = \begin{pmatrix} X\sin\left(\frac{\pi}{\mathrm{d}}(z+\frac{h}{2})\right) \\ Y\sin\left(\frac{\pi}{\mathrm{d}}(z+\frac{h}{2})\right) \\ 1-(X^2+Y^2)\sin^2\left(\frac{\pi}{\mathrm{d}}(z+\frac{h}{2})\right) \end{pmatrix} + h.o.t., \tag{4.5}$$

Using this ansatz in (4.4) with the help of the complex parameter $A = X + \mathrm{i}Y$, defining $\partial_\eta = \partial_x + \mathrm{i}\partial_y$ and after several straightforward calculations [48], and using $z_o = h/2$, we obtain

$$\begin{aligned}\gamma\partial_t A = \quad & \underbrace{\left[\lambda_0 + \varepsilon_a\left(\frac{V_0}{\mathrm{d}}\right)^2 + \chi_a B_z^2(z_0)\right]}_{\mu} A - a|A|^2A + \frac{K_1+K_2}{2}\nabla^2 A + \frac{K_1-K_2}{2}\partial_{\eta\eta}\bar{A} \\ & -\frac{4\chi_a}{\pi}B_z(z_0)B_\rho(z_0)\mathrm{e}^{\mathrm{i}\theta} - \frac{8\chi_a}{3\pi}B_z(z_0)B_\rho(z_0)\left(2AR\mathrm{e}(A\mathrm{e}^{-\mathrm{i}\theta}) + \frac{|A|^2\mathrm{e}^{\mathrm{i}\theta}}{2}\right),\end{aligned}$$

with $\lambda_o = -K_3\left(\frac{\pi}{\mathrm{d}}\right)^2$, $a = \frac{1}{4}\left[(K_1 - K_3)\left(\frac{\pi}{\mathrm{d}}\right)^2 - 3\varepsilon_a E_z^2 - 3\chi_a B_z^2\right]$. Dropping the smaller correction and rescaling the parameter A as $A(\vec{\rho}, t) \to \frac{1}{\sqrt{a}}A\left(\sqrt{\frac{2}{K_1+K_2}}\vec{r}, \frac{t}{\gamma}\right)$, we get the Topologically Driven Ginzburg-Landau equation

$$\partial_t A = \mu(\rho)A - |A|^2A + \nabla^2 A + \delta\partial_{\eta\eta}\bar{A} + f(\rho)\mathrm{e}^{\mathrm{i}\theta}, \tag{4.6}$$

where $\mu(\rho) = \mu_0 + \mu_1(\rho)$ is the inhomogeneous bifurcation parameter, $\mu_0 \equiv -K_3(\pi/\mathrm{d})^2 - \varepsilon_a E_z^2$ is the bifurcation parameter related to the electrical Fréedericksz transition, $\mu_1(\rho) \equiv \chi_a B_z^2(\rho, z_0)$ is the inhomogeneous modification of the reorientational transition, $\delta = (K_1 - K_2)/(K_1 + K_2)$ accounts for the elastic anisotropy of the liquid crystal, $\partial_\eta \equiv \partial_x + \mathrm{i}\partial_y$ is a differential operator in the complex plane, note that the laplacian satisfies $\nabla^2 = \partial_{\eta,\bar{\eta}}$, and $f(\rho) = 4\chi_a a^{1/2} B_\rho(\rho, z_0) B_z(\rho, z_0)/(\gamma\pi)$ accounts for the strength of the topological forcing. Figures 4.10 and 4.11 show the bifurcation parameter and the forcing as a function of the radial coordinate respectively. Notice that the vortices are placed at the zeros of the forcing and $f(\rho)$ is annulled at the origin and in the circumference of radius ρ^*.

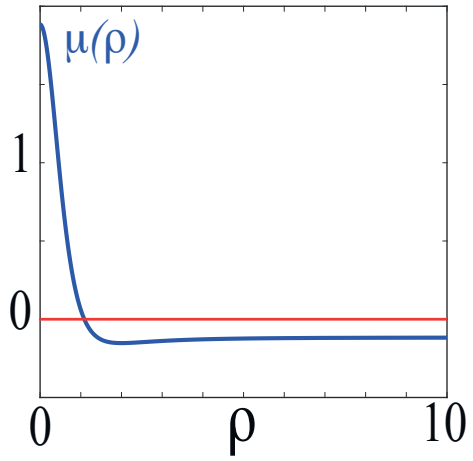

Figure 4.10: Profile of the inhomogeneous bifurcation parameter $\mu(\rho)$ as a function of the radial coordinate. Courtesy of Enrique Calisto.

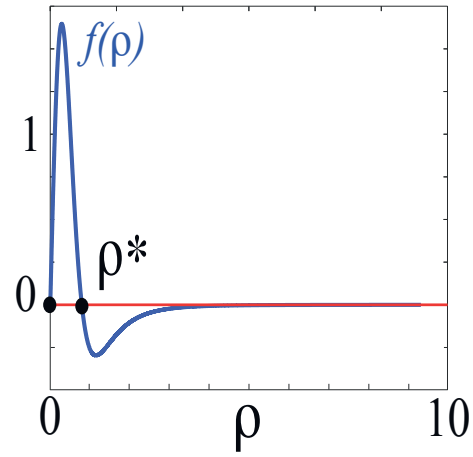

Figure 4.11: Profile of topological forcing strength $f(\rho)$ as a function of the radial coordinate. Courtesy of Enrique Calisto.

We renormalize $\rho = \sqrt{x^2 + y^2/z_0}$. Due to the dynamics are slow, we can apply the Fermi limit when $z_o \gg 1$ and neglect the spatial derivatives in the equation (4.6). Along with this,

we also neglect nonlinear terms and considering the regime below the electrical Freèdericksz transition $\mu_o \lesssim 0$, we obtain the following stationary solution (vortex Fermi approximation),

$$A(\rho) = \frac{-bB(\rho, z_o)B_\rho(\rho, z_o)}{\mu}. \tag{4.7}$$

Then, the system exhibits an analytical solution of the form $A \approx f(r)\mathrm{e}^{\mathrm{i}\theta}/\mu_o$ [46]. Indeed, this solution is characterizing by exhibiting a vortex at the center and also a circular defect line that circumscribes it.
Using a triangular finite element code with adaptive spatial and temporal steps, and a simulation box of dimensions 300 x 300 with Neumann boundary condition we did numerical simulations of model (4.6) with diferent conditions as shown in Figure 4.12, top panel corresponds to the polarized field $\psi(x, y) \equiv \mathrm{Re}(A)\,\mathrm{Im}(A)$ [10], bottom panel corresponds to the phase field $\Phi = arctan\,[\mathrm{Im}(A)/\,\mathrm{Re}(A)]$. For $\mu_o < 0$ we only detect the central vortex with a cross shape Figure 4.12c) and the ring that circumscribes the central vortex is only detected in the phase field. This ring has two singularities of opposite charges in its antipodes. This numerical observation is consistent with the experimental one observed for low frequency (see top panels in Fig.4.4). Increasing the bifurcation parameter, the central vortex swirls and the ring that encloses the amplitude notoriously show two vortices of opposite charges at the antipodes (see Figure 4.12d) which coincide with that we observe in the experiments Figures 4.5 and 4.7. Considering a larger bifurcation parameter and starting from $A = 0$, we see the vortex emerge at the center with a circular defect line that destabilizes into a set of vortices that begin to interact and annihilate in pairs Figure 4.12e). We note that a similar phenomenon we observe in the experiments Figure 4.6. Thus, the model Eq. (4.6) describes the emergence of a vortex triplet induced by the combined action of a close magnetic ring and electric field into a nematic liquid crystal layer.

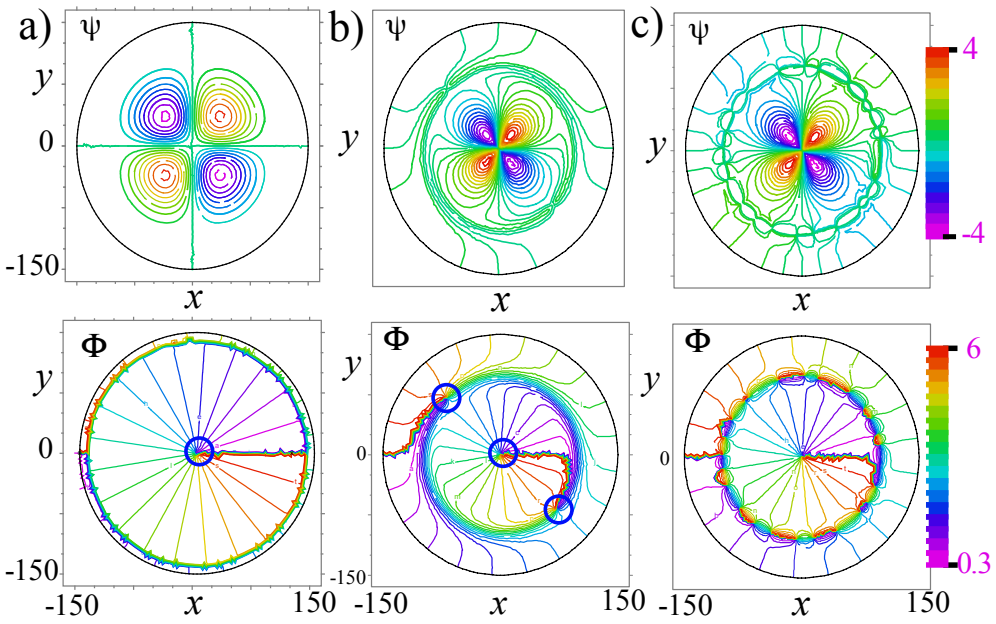

Figure 4.12: Numerical simulation of vortex triplex obtained from the topologically Driven Giznburg-Landau Eq. (4.6) with $z_0 = 28$, $\sigma = 28$, $m = 13000$, and $\delta = 0.1$. Contour plot of the polarized field $\psi(x, y) = Re(A)Im(A)$ (top panel) and phase field $\Phi(x, y) = \arctan[Im(A)/Re(A)]$ (bottom panel) of the complex amplitude A, below $\mu_0 < 0$ ($\mu_0 = -1$) (c) and above $\mu_0 > 0$ [$\mu_0 = 0.2$ (d) and $\mu_0 = 3.0$ (e)] the Fréedericksz voltage. Inserted circles highlight phase singularities. Courtesy of Enrique Calisto.

4.5 A new phenomenon

Unexpectedly, when we decrease the frequency to a fraction of a hertz, experimentally, the vortex triplet is destabilized from both the central vortex and the ring that circumscribes it by the induction of vortices, resulting in a front of vortices invading the system (see Fig. 4.13). A stationary oscillatory vortex lattice characterizes the equilibrium state of the system. When the oscillatory behavior of the electric field is included in model Eq. (4.12), it does not describe the phenomenon observed experimentally. However, we expect that this state corresponds to an exotic state similar to exotic states we found in chapter 3 but now it is generated by electric and magnetic field, following this thought it would be interesting considering inertia to model Eq. (4.12).

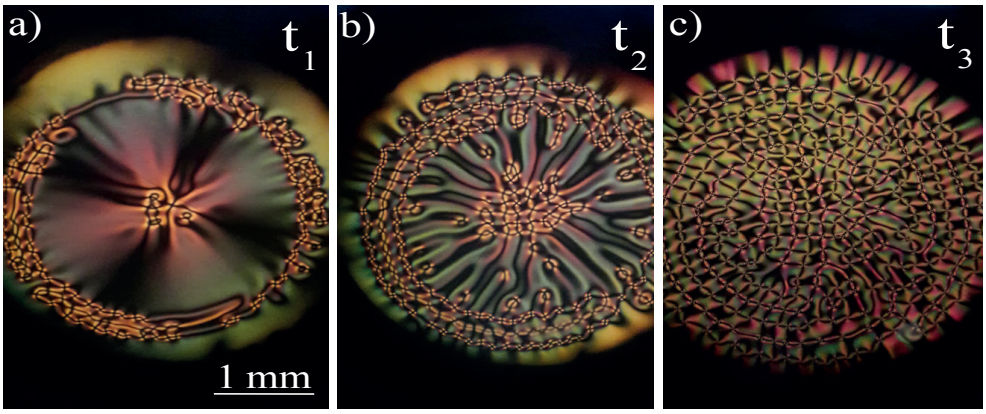

Figure 4.13: Vortex lattices. A temporal sequence of snapshots of the emergence of vortex lattice from a vortex triplet $t_0 < t_1 < t_2$, with $V_0 = 9.0$ Vpp and $\omega = 10$ mHz.

To describe qualitatively this phenomenon, analogously to what was done in chapter 3, we include in the model Eq. (4.6) a term of inertia, i.e. a second temporal derivate of amplitude A, and a temporally modulated bifurcation parameter term,

$$\partial_{tt}A + \lambda\partial_t A = \left[\mu(\rho) + \gamma\cos(2\pi f t)\right] A - |A|^2 A + \nabla^2 A + \delta\partial_{\eta\eta}\bar{A} + f(\rho)\mathrm{e}^{\mathrm{i}\theta}, \qquad (4.8)$$

where λ accounts for rotational viscosity, γ and f are the amplitude and the frequency of the forcing, respectively.
Numerical simulations of this model Eq.(4.8) were implement using a finite differences code with Runge-Kutta order-4 algorithm, with 200x200 points grid, spacing $\mathrm{d}x = 0.05$, and temporal increment $\mathrm{d}t = 0.02$.
Figure 4.14 shows numerical simulations of Eq.(4.8) left panel corresponds to $|A|$, center panel corresponds to $\mathrm{Re}(A)\,\mathrm{Im}(A)$ and right panel corresponds to $\mathrm{Phase}(A)$. Notice that $\mathrm{Re}(A)\,\mathrm{Im}(A)$ corresponds experimentally to use linear crossed polarizer. In the Figure 4.14 we can see a central vortice and vortices that surround it in a circular way, similar to that observed in Figures 4.13 a) and b). However, we still need to work on improving the model in order to better describe the phenomenon observed.

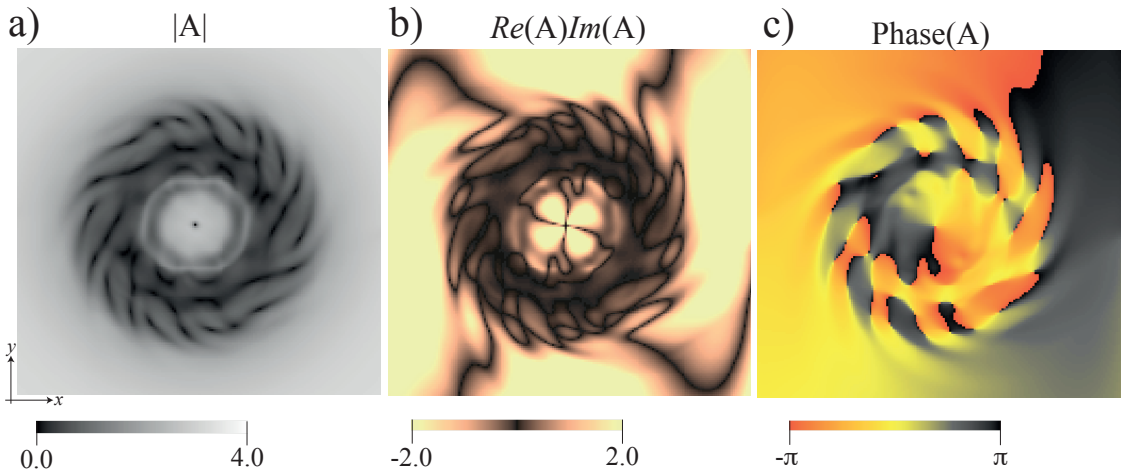

Figure 4.14: Numerical simulation of model Eq.(4.8). a) $|A|$, b) $\mathrm{Re}(A)\,\mathrm{Im}(A)$, and c) $\mathrm{Phase}(A)$.

In conclusion, We induce a stable vortex triplet in a homeotropic nematic liquid crystal cell by the combined application of the magnetic field of a magnetic ring and the uniform electric field. An amplitude equation with topological forcing valid close to the Fréederickzs transition allow us to reveal the origin of the vortex triplet. Theoretical findings show a quite fair agreement with experimental observations. When the frequency decreases the vortex triplet is destabilized and a vortex network is formed. This phenomenon is described qualitatively by the equation (4.8). However, a more detailed study is necessary to modify this model in order to better describe the observed phenomenon.

Chapter 5

Vortex nucleation by inherent fluctuations in nematic liquid crystal layers

In the last decades different studies have allowed to know more about the behavior of vortices in nematic liquid crystal. Pismen [8] showed that the interaction between two vortices of opposite topological charge at long-distance is proportional to the inverse of the distance between them. Besides, the interaction has a correction in mobility that, although slight, can be verified experimentally [27]. Later, Dierkieng [11] and Nagaya [49] showed that the density of vortices in a homogeneous liquid crystal cell as a function of time decreases as the inverse of time. Our recent work [50] has shown that the number of vortices in an inhomogeneous nematic liquid crystal cell decays as a function of time with a power law. Thus, the process of interaction and annihilation of vortices is well known, however the process of nucleation of vortices in liquid crystal is still a mystery. Hence, we are interested in studying what parameters influence in the nucleation of vortices and how important is the presence of fluctuations in this process.

5.1 Experimental Setup

To study vortex creation, we have consider a 15 μm thick cell,(SB100A150uT180 manufactured by instec) was filled with nematic liquid crystal LC BYVA- 01-5G (Instec) with negative dielectric anisotropy $\varepsilon_a = -4.89$, birefringence $\Delta n = n_e - n_o = 0.1$, rotation viscosity $\gamma = 204$ mPas, splay and bend elastic constant, respectively, $K_1 = 17.65$ pN and $K_3 = 21.39$ pN. This sample is placed inside a thermal stage (Linkam LTS420), which in turn is inserted inside a Leica microscope, in between the crossed linear polarizers. To capture the images a CMOS camera is connected to the microscope. A sinusoidal voltage with a frequency of 100 Hz is applied to the sample. Maintaining the temperature at 26 °C, the voltage is turned on, the dynamics of vortex creation and annihilation are recorded. The same procedure is carried out for a voltage sweep between 9.0 Vpp and 30.0 Vpp. Subsequently, the voltage is switched on at 15 Vpp and the dynamics of vortex creation and annihilation are recorded. The above procedure is repeated for a temperature scan between 25°C and 80°C.

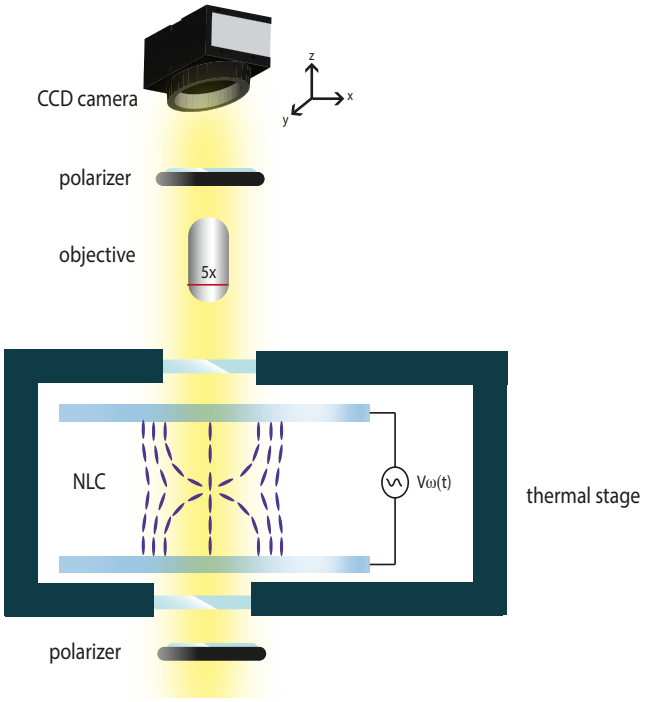

Figure 5.1: Schematic representation of experimental setup. Nematic liquid crystal cell is inserted in a thermal stage and iluminated by white light between two linear crossed polarizers. A a sinusoidal voltage is applied to the sample.

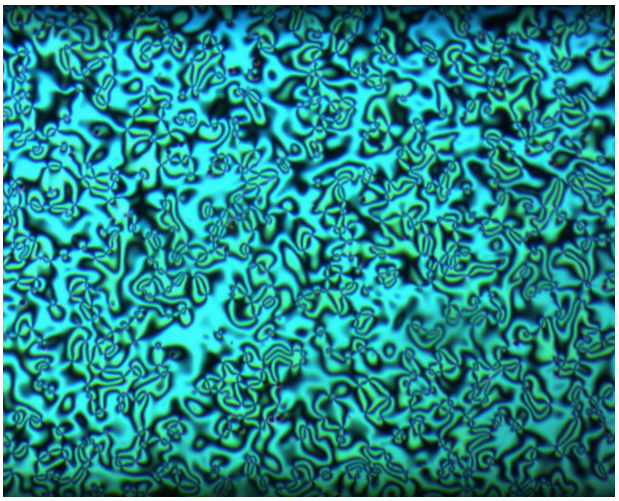

Figure 5.2: Emergence of vortices in nematic liquid crystal when the voltage in the experimental setup is turned on.

5.2 Theoretical description

To study vortex creation, we have incorporated non correleated white noise to Ginzburg Landau equation

$$\partial_t A = \mu A + \nabla^2 A + \delta \partial_{\eta\eta} \bar{A} - |A|^2 A + \xi(x,y,t)\sqrt{\eta}, \tag{5.1}$$

where $A = u + \mathrm{i}v$, $\partial_\eta = \partial_x + \mathrm{i}\partial_y$, and $\xi(x,y,t)$ is a complex white noise $\xi = \xi_u + \mathrm{i}\xi_v$ with $\langle \xi \rangle = 0$ and $\langle \xi | \xi^* \rangle = \delta(t-t')\delta(r-r')$. Then, neglecting nonlinear terms, we obtain

$$\partial_t u = \mu u + (\partial_{xx} + \partial_{yy})u + \delta(\partial_{xx} - \partial_{yy})u - 2\delta\partial_x\partial_y v + \xi_u(x,y,t)\sqrt{\eta}$$
$$\partial_t v = \mu v + (\partial_{xx} + \partial_{yy})v + \delta(\partial_{xx} - \partial_{yy})v + 2\delta\partial_x\partial_y u + \xi_v(x,y,t)\sqrt{\eta}$$

thus the deterministic part

$$\begin{pmatrix} \dot{u} \\ \dot{v} \end{pmatrix} = \begin{pmatrix} \mu + (\partial_{xx} + \partial_{yy}) + \delta(\partial_{xx} - \partial_{yy}) & -2\delta\partial_x\partial_y \\ 2\delta\partial_x\partial_y & \mu + (\partial_{xx} + \partial_{yy}) + \delta(\partial_{xx} - \partial_{yy}) \end{pmatrix} \begin{pmatrix} u \\ v \end{pmatrix}. \tag{5.2}$$

Using the following ansatz

$$\begin{pmatrix} u \\ v \end{pmatrix} = \begin{pmatrix} u_o \\ v_o \end{pmatrix} \mathrm{e}^{\mathrm{i}(k_x x + k_y y)} \mathrm{e}^{\sigma t} \tag{5.3}$$

then,

$$\sigma \begin{pmatrix} u_o \\ v_o \end{pmatrix} = \begin{pmatrix} (\mu - k_x^2(1+\mathrm{d}) - k_y^2(1-\mathrm{d})) & +2\delta k_x k_y \\ -2\delta k_x k_y & (\mu - k_x^2(1+\mathrm{d}) - k_y^2(1-\mathrm{d})) \end{pmatrix} \begin{pmatrix} u_o \\ v_0 \end{pmatrix} \tag{5.4}$$

defyning $\alpha = \mu - k_x^2(1+\mathrm{d}) - k_y^2(1-\mathrm{d})$, we calculate the Determinante

$$0 = Det \begin{pmatrix} \alpha - \sigma & +2\delta k_x k_y \\ -2\delta k_x k_y & \alpha - \sigma \end{pmatrix}, \tag{5.5}$$

we obtain

$$0 = (\alpha - \sigma)^2 + 4\delta^2 k_x^2 k_y^2, \tag{5.6}$$

Therefore, we have the following σ

$$\sigma = \alpha \pm 2\mathrm{i}\delta k_x k_y.$$

Considering only the real part

$$\mathrm{Re}\,(\sigma) = \mu - k_x^2(1+\mathrm{d}) - k_y^2(1-\mathrm{d}), \tag{5.7}$$

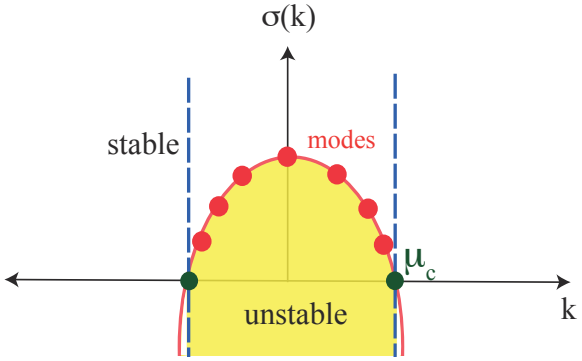

Figure 5.3: Curve of $\sigma(k)$. The red dots correspond to its modes, the green dots correspond to the critical modes μ_c, the latter are the modes that generate the greatest amount of vortices.

we looking for the critical values (see Figure 5.3, this shows the case for one dimension)

$$\mu_c = k_x^2(1+\mathrm{d}) + k_y^2(1-\mathrm{d}) \tag{5.8}$$

defyning $k_x = \frac{\pi}{L} n_x$ and $k_y = \frac{\pi}{L} n_y$ we calculate how many zeros we have in x cordinate

$$\mu = \frac{\pi^2}{L^2} n_x^2 (1+\delta), \tag{5.9}$$

$$n_x = \sqrt{\frac{L^2\mu}{\pi^2(1+\delta)}}. \tag{5.10}$$

Likewise, we calculate how many zero are created in y coordinate

$$\mu = \frac{\pi^2}{L^2} n_y^2 (1-\delta), \tag{5.11}$$

$$n_y = \frac{L}{\pi}\sqrt{\frac{\mu}{(1-\delta)}}, \tag{5.12}$$

Therefore, usign (5.10) and (5.12), the maximun number of zeros that we have in total is

$$N = n_x n_y = \frac{L^2\mu}{\pi^2\sqrt{(1-\delta^2)}}$$

The noise excites all modes equally, it is flat in Fourier space [51], then stable modes are damped and unstable modes grow and generate vortices. The critical mode is the one that generates more zeros that originate vortices Thus, we can say that the typical number of vortex N_o, created due to the fluctuations in a nematic liquid crystal has the form

$$N_o = \frac{A\mu}{\sqrt{(1-\delta^2)}} \tag{5.13}$$

5.3 Numerical Simulations

Numerical simulations of equation (5.1) were implemented using an Euler method algorithm, with a 100*100 points grid, spacing dx = 0.5, and temporal increment dt = 0.0025. This simulations have an initial condition $A(x,t) = 0$, Neumann boundary condition $\partial_\eta A = 0$ and the noise is modeled as Weiner process, i.e, as a normal distribution with standard deviation. To locate the vortices, the argument of $A(x,t)$ is integrated around a small closed path. If this integral is equal to 0 there are no vortices, if it is equal to ± 1 there is a vortex.
Numerical simulations were made by modifying different parameters of Ginzburg Landau with noise, equation (5.1), as described in the following paragraphs.

Numerical simulations were made leaving anisotropy δ and noise intensity level constant and modifying the value of the bifurcation parameter μ for 120 different values between 0 and 10. For each value of the bifurcation parameter, 30 repetitions were performed and for each repetition a different seed of random numbers was used for noise.

Analogously, numerical simulations were carried out leaving the bifurcation parameter μ and the noise intensity level constant, modifying the anisotropy value δ between 0 and 1, taking 20 repetitions for each value. Also, other simulations were performed leaving the bifurcation parameter μ and the anisotropy δ constant, modifying the noise intensity value between 10^{-3} and 10^{3}, taking 10 repetitions for each value.

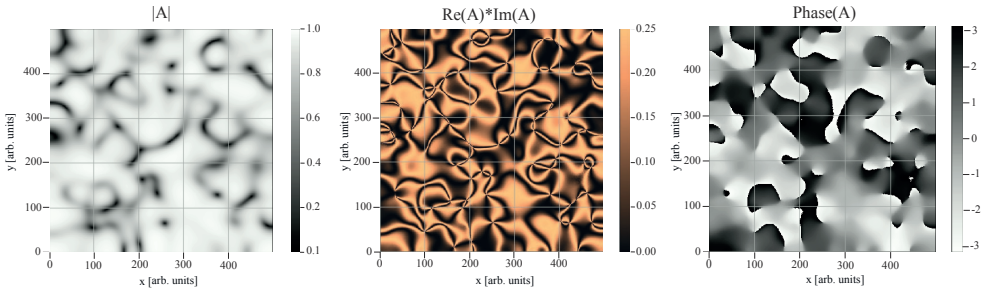

Figure 5.4: Numerical simulations of equation (5.1). Left, central and right panels correspond to $|A|$, $\mathrm{Re}(A) * \mathrm{Im}(A)$ and $Phase(A) = \arctan(\mathrm{Im}(A)/\mathrm{Re}(A))$ respectively. Courtesy of Esteban Aguilera.

5.4 Results

5.4.1 Number of vortices as a function of bifurcation parameter

The number of vortices created for different values of the bifurcation parameter μ was measured both experimentally and numerically. Figures 5.5 a) and b) shows the creation of vortices in a liquid crystal cell of 15 μm thickness for a voltage of 15 Vpp and 30 Vpp respectively. Figures 5.6 and 5.7 show the vortex number as a function of μ both experimental and numerical for different measurement times. Figure 5.6b) is for $t = 0.1$ s and Figure 5.7b) is for $t = 1.0$ s. In both figures we can see that in general the number of vortices created increases with increasing the voltage.

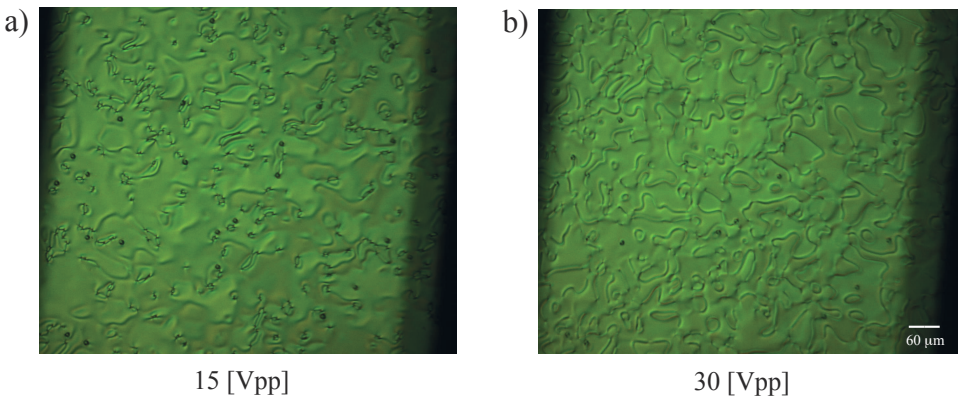

Figure 5.5: Vortices created in area 1.39 mm^2 in a 15 μm thickness nematic liquid crystal cell. a)15 [Vpp] sinusoidal voltage es applied with a frequency 100 [Hz], b) 30 [Vpp] sinusoidal voltage es applied with a frequency 100 [Hz].

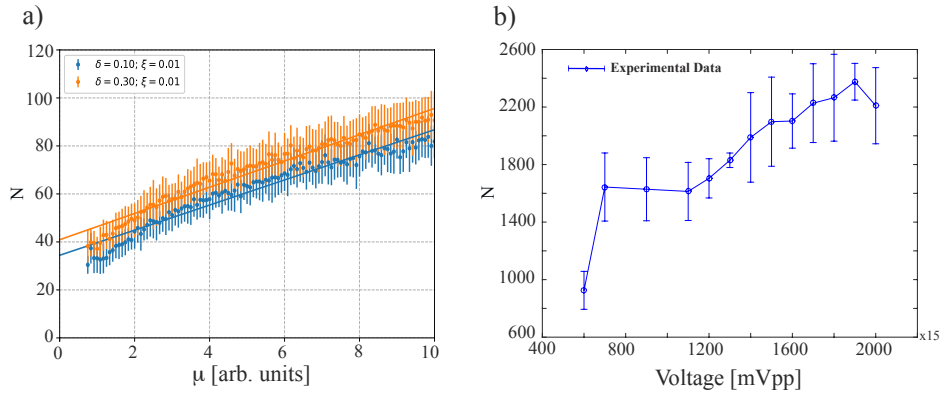

Figure 5.6: Number of vortices for different values of μ. a) Numerical results of equation (5.1) for time $t = 12$, orange dot correspond to $\delta = 0.1$ and $\xi = 0.01$, and blue dots correspond to $\delta = 0.3$ and $\xi = 0.01$, courtesy of Esteban Aguilera. b) Experimental result for a nematic liquid crystal cell with 15 μm of thickness at 26°C and frequency of voltage applied 100 Hz. This results are for a time $t = 0.1$ s.

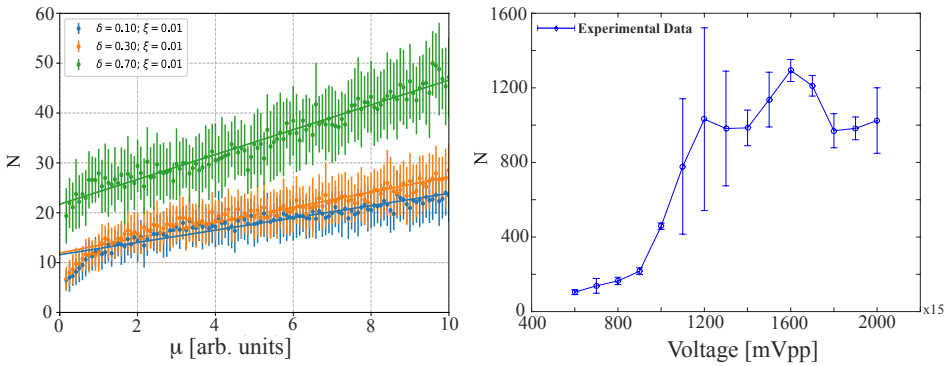

Figure 5.7: Number of vortices for different values of μ. a) Numerical results of equation (5.1) for time $t = 60$. Blue dots correspond to $\delta = 0.1$ and $\xi = 0.01$, orange dots correspond to $\delta = 0.3$ and $\xi = 0.01$, and green dots correspond to $\delta = 0.7$ and $\xi = 0.01$. Courtesy of Esteban Aguilera b)Experimental result for a nematic liquid crystal cell with 15 μm of thickness at 26°C and frequency of voltage applied 100 Hz. This results are for a time $t = 1.0$ s.

5.4.2 Number of vortices as a function of anisotropy

Figure 5.8 shows the number of vortices created for different values of anisotropy. This result is only numerical since experimentally it could not be measured due to the lack of control over the changes in anisotropy in a liquid crystal. To these results, we apply the fit $N = A/(1-\delta^2)^b + C$. We can observe in Figure 5.8a) that for short times, when the vortices are newly created, the exponent b is close to 0.5 for both $\mu = 1.0$ and $\mu = 10.0$, Then, we corroborate that our theory (5.13) is correct. For long time we can observe in figure 5.8b) that b is arround 1 and it differs substantionaly from our theoretical value (5.13), the reason

is that for long times, the processes of interaction and annihilation of vortices are present and non-linear terms also play a role in the dynamics of liquid crystals.

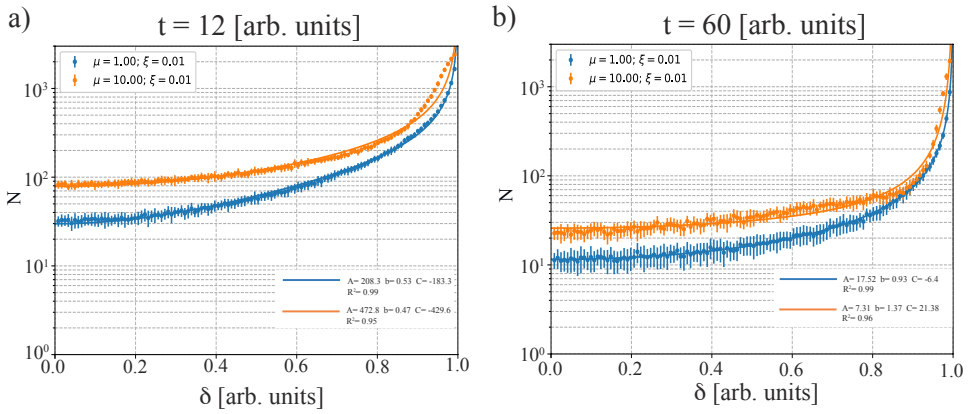

Figure 5.8: Number of vortices for different values of δ. a) Numerical results of equation (5.1) for time $t = 12$. Blue dots correspond to $\mu = 1.0$ and $\xi = 0.01$, orange dots correspond to $\mu = 10.0$ and $\xi = 0.01$. b) Numerical results of equation (5.1) for time $t = 60$. Blue dots correspond to $\mu = 1.0$ and $\xi = 0.01$, orange dots correspond to $\mu = 10.0$ and $\xi = 0.01$.

5.4.3 Number of vortices as a function of noise

Numerically, Figure 5.9 shows the number of vortices as a function of noise for different times. We can observe that in Figure 5.9a) the number of vortices created scales as a power law with the intensity of the noise. Therefore, the number of votices created increases with the intensity of noise. For a long time (t=60) after the creation of vortices, we can see that until $x\mathrm{i} = 10$ the number of these remains constant, and from $x\mathrm{i} = 10^1$ onwards it is observed that the vortex number grows as a power law such as shown in figure 5.9b) we note that, when the intesity of noise is $\xi = 12$ numerical simulations lost the physical sense.

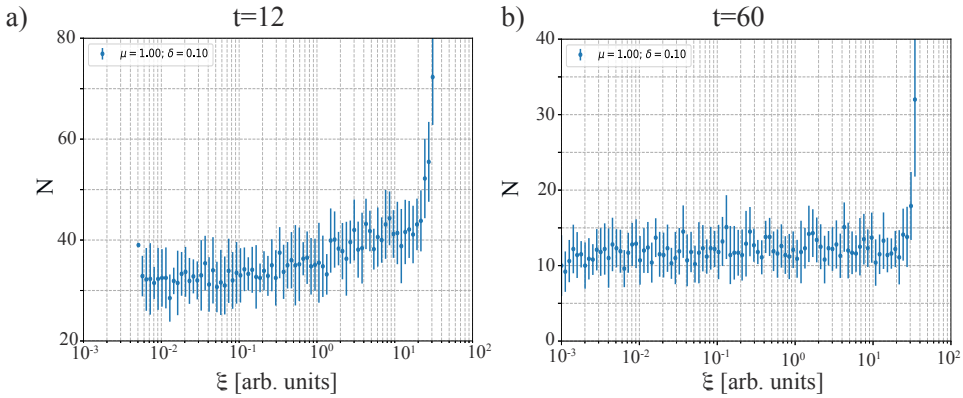

Figure 5.9: Number of vortices for different values of noise ξ. a) Numerical results of equation (5.1) for time $t = 12$, $\mu = 1.0$ and $\delta = 0.1$. b)Numerical results of equation (5.1) for time $t = 60$, $\mu = 1.0$ and $\delta = 0.1$. Courtesy of Esteban Aguilera.

5.4.4 Number of vortices as a function of temperature

The inherent fluctuations of the liquid crystal cells are dependent on temperature. Experimentally, the number of vortices was measured as a function of the temperature for different times since the votices are created (t = 0). Figure 5.12a) shows the creation of vortices for $t = 0.1$. The number of vortices increase when the temperature increases until it saturates at 70°C. Therefore, when the thermal fluctuations increase, the nucleation of vortices increases.

After 1 second, we can see in Figure 5.12b) that the number of vortices increases linearly with the temperature. Note that the vortex interaction and annihilation come into play in this regime. For a longer time (5 s), we can see in Figure 5.12c) that the number of vortices as a function of temperature decreases. This is due to the fact that increasing temperature, the number of vortices increases, and that the dynamics of vortices becomes faster. Therefore, the vortices are annihilated much quicker, as shown in Figures 5.10 and 5.11.

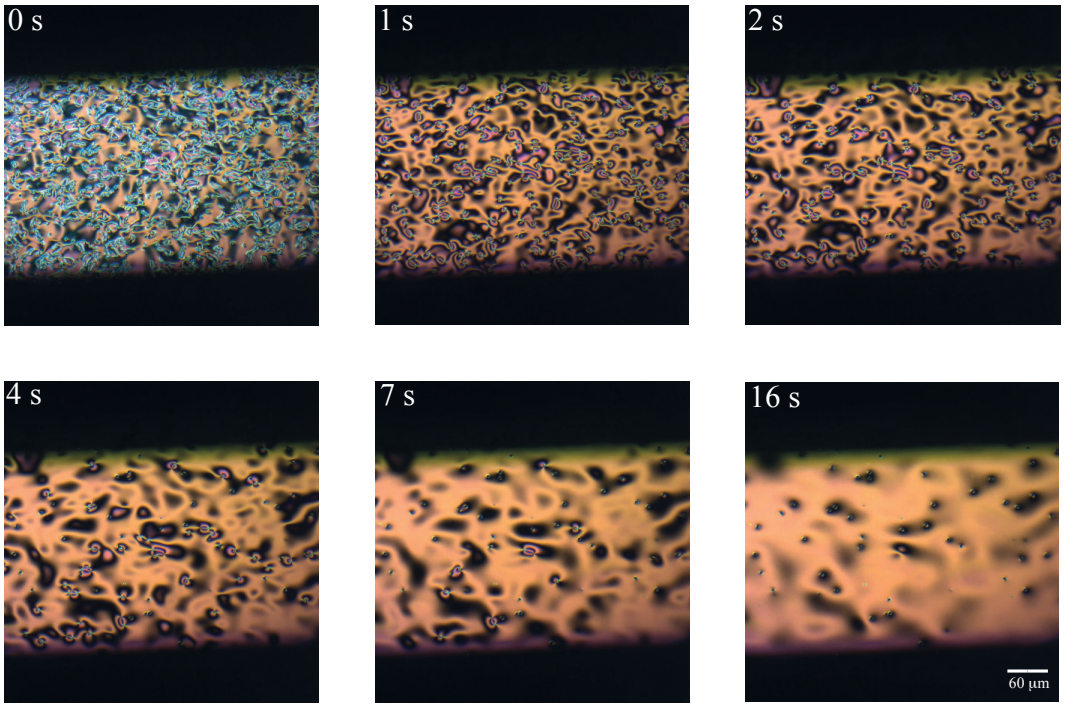

Figure 5.10: Temporal sequence of snapshots depicts umbilical defects dynamics in a nematic liquid crystal cell with 15 μm of thickness at 20°C. The sinusoidal voltage applied is 15 Vpp with a frequency of 100 Hz.

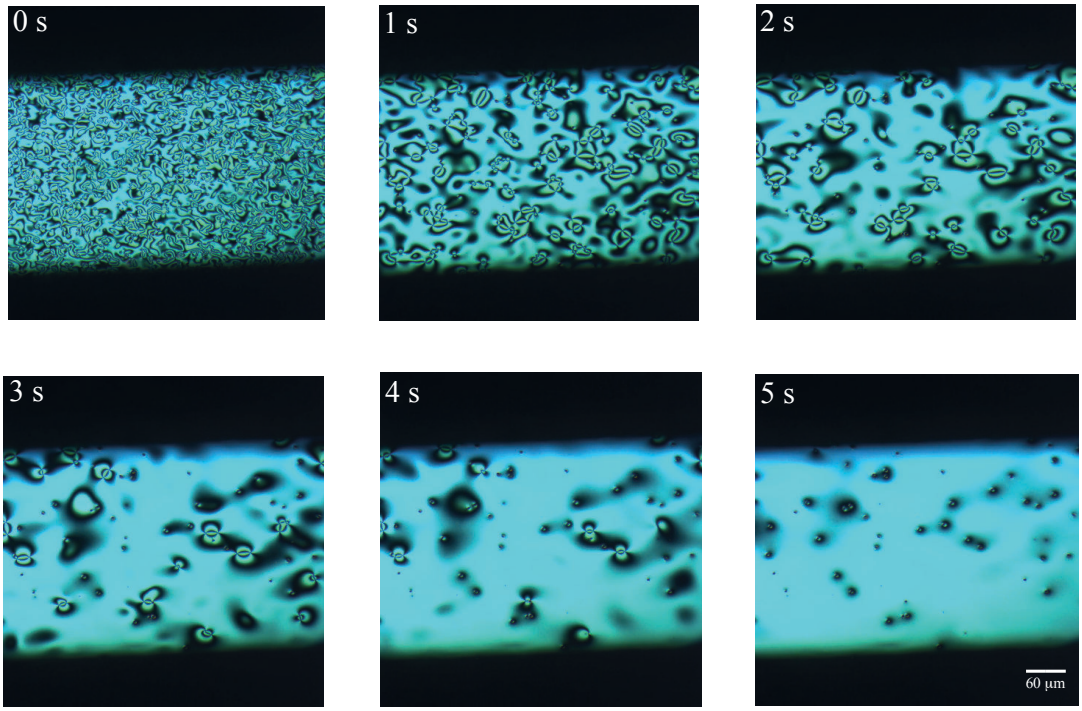

Figure 5.11: Temporal sequence of snapshots depicts umbilical defects dynamics in a nematic liquid crystal cell with 15 μm of thickness at 80°C. The sinusoidal voltage applied is 15 Vpp with a frequency of 100 Hz.

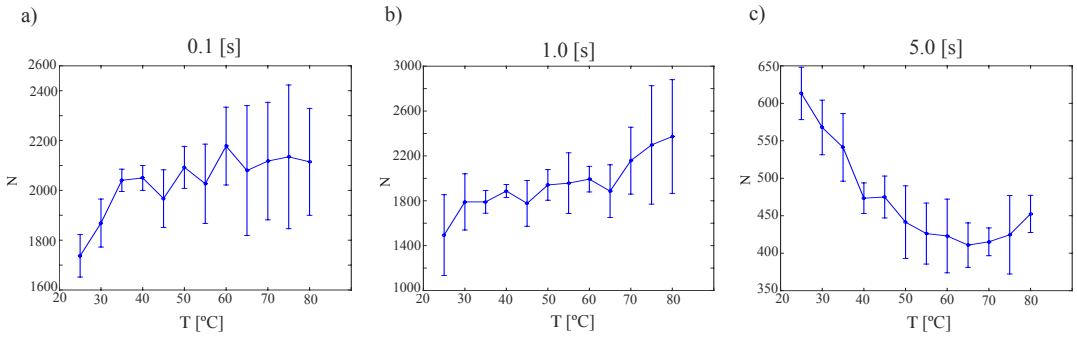

Figure 5.12: Number of vortices for different values of temperature T for a nematic liquid crystal cell with 15 μm of thickness with a sinusoidal voltage of 15 Vpp with frequency 100 Hz. a) For a initial time $t = 0.1$ s. b) For a time $t = 1.0$ s. c) For a time $t = 1.0$ s.

5.4.5 Number of vortices as a function of time

The number of vortices as a function of time was measured for different values of voltage, anisotropy, temperature, and thickness of the nematic liquid crystal cell. In Figure 5.13, we can see that both experimentally and numerically, the number of vortices as a function of time scale as a power law. Therefore, our numerical simulations describe the experiment results quite well.

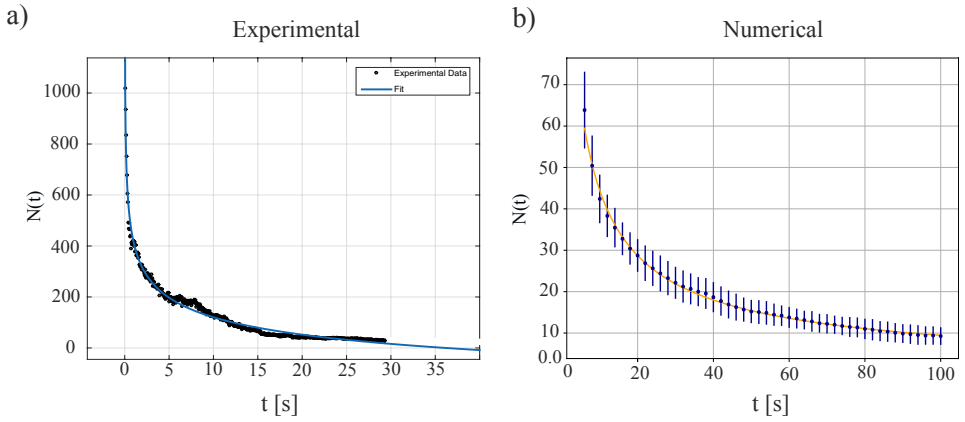

Figure 5.13: Number of vortices as a function of time t. a) Numerical results of equation (5.1) for $\mu = 1.5$ and $\delta = 0.1$, Courtesy of Esteban Aguilera. b)Experimental result for a nematic liquid crystal cell with 15 μm of thickness at 26°C and voltage applied of 15 Vpp with frequency of 100 Hz.

To study the number of vortices as a function of time, the fitting (2.5) from Chapter 2 was used,

$$N(t) = A(t)^{-b} + c, \tag{5.14}$$

where N corresponds to number of vortices, A, b, and c are constants parameters. Figure 5.14 corresponds to the graphs of the parameter A of the equation (5.14) for different values of the bifucation parameter. Panel a) corresponds to a nematic liquid crystal cell with 15 μm of thickness, panel b) corresponds to a nematic liquid crystal cell with 75 μm of thickness. panel c) corresponds to numerical simulations where the blue points are for $\delta = 0.10$ and $\xi = 0.01$ and orange points for $\delta = 0.30$ and $\xi = 0.01$.

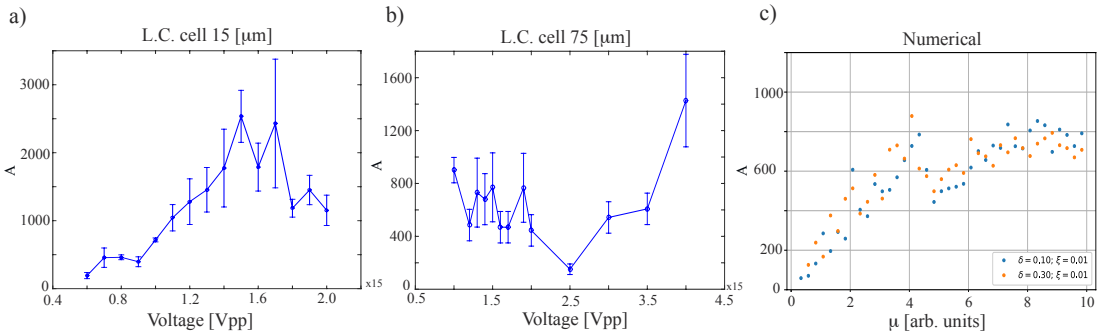

Figure 5.14: A for different values of μ. a)Experimental result for a nematic liquid crystal cell with 15 μm of thickness at 26°C and frequency of voltage applied 100 Hz. b) Experimental result for a nematic liquid crystal cell with 75 μm of thickness at 26°C and frequency of voltage applied 100 Hz. c) Numerical results of equation (5.1) where blue dots correspond to $\delta = 0.1$ and $\xi = 0.01$, orange dots correspond to $\delta = 0.3$ and $\xi = 0.01$.

Figure 5.15 corresponds to graphs of the parameter b of the 5.14 equation for different

values of the bifucation parameter μ. Panel a) corresponds to a 15 μm thick nematic liquid crystal cell, panel b) corresponds to a 75 μm thick nematic liquid crystal cell. Panel c) corresponds to numerical simulations where the blue points are for $\delta = 0.10$ and $\xi = 0.01$ and orange points for $\delta = 0.30$ and $\xi = 0.01$.

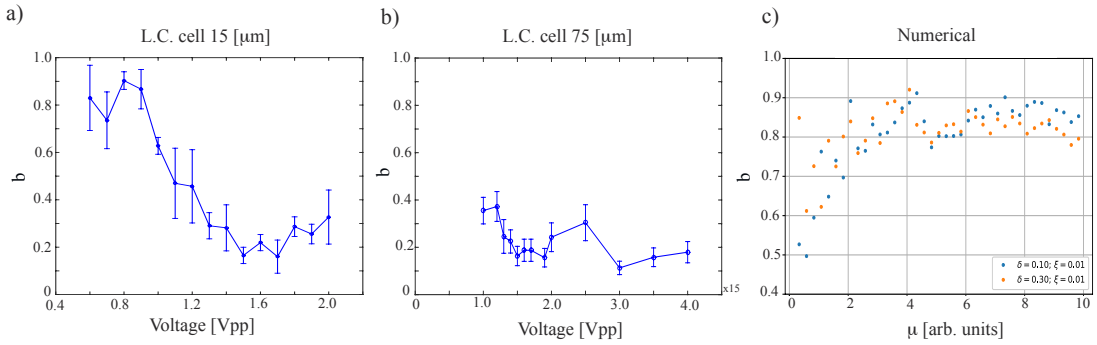

Figure 5.15: b for different values of μ. a)Experimental result for a nematic liquid crystal cell with 15 μm of thickness at 26°C and frequency of voltage applied 100 Hz. b) Experimental result for a nematic liquid crystal cell with 75 μm of thickness at 26°C and frequency of voltage applied 100 Hz. c) Numerical results of equation (5.1) where blue dots correspond to $\delta = 0.1$ and $\xi = 0.01$, orange dots correspond to $\delta = 0.3$ and $\xi = 0.01$.

Figure 5.16 corresponds to numerical results graphs of parameters A and b of the equation 5.14 for different values of anisotropy δ. Blue points are for $\delta = 0.10$ and $\xi = 0.01$ and orange points for $\delta = 0.30$ and $\xi = 0.01$.

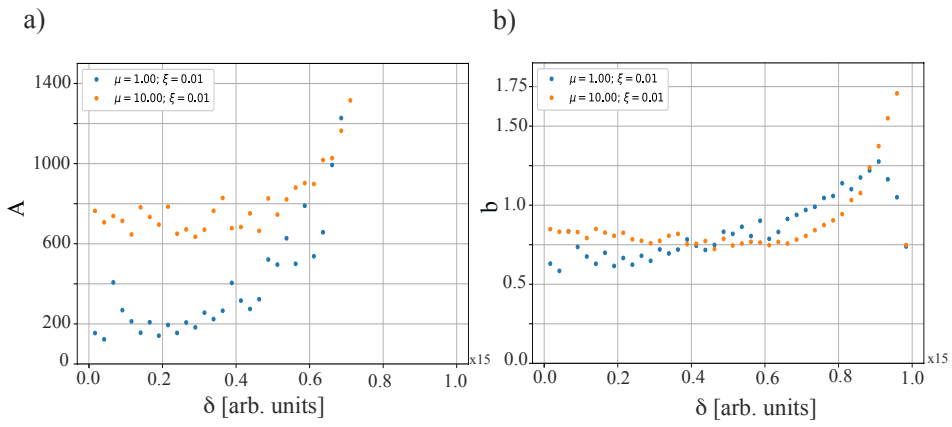

Figure 5.16: Numerical results of fit parameters for different values of anisotropy δ where blue dots correspond to $\mu = 1.0$ and $\xi = 0.01$ and orange dots correspond to $\mu = 10.0$ and $\xi = 0.01$. a)Plot of A v/s δ. b)Plot of b v/s δ. Courtesy of Esteban Aguilera.

Figure 5.17 corresponds to graphs of parameters A and b of the 5.14 equation for different values of temperature. This experimental results belong to a nematic liquid crystal cell with 15 μm thickness.

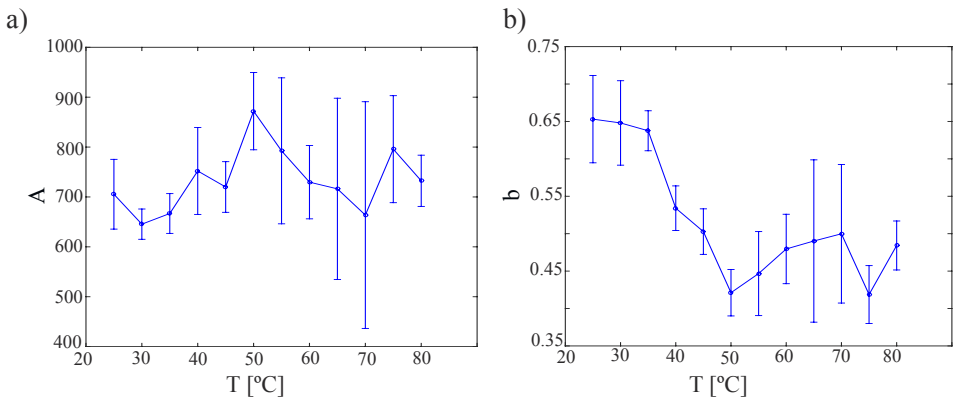

Figure 5.17: Experimental results of fit parameters for different values of temperature T for a nematic liquid crystal cell with 15 μm of thickness and a sinusoidal voltage applied of 15 Vpp with a frequency of 100 Hz. a) Plot of A v/s δ. b)Plot of b v/s δ.

In conclusion, we have shown that the thermal fluctuations are responsible for vortices nucleation in a nematic liquid crystal cell and the number of nucleated vortices is described by $N = \frac{A\mu}{\sqrt{(1-\delta^2)}} + C$. Therefore, the number of vortices created when the voltage, noise, and temperature increase and scales with anisotropy as $\sim 1/\sqrt{(1-\delta^2)}$. The number of vortices as a function of time scales as a power law whose exponent varies with the bifurcation, anisotropy, and temperature.

Chapter 6

Conclusions

In this dissertation, an experimental and theoretical study of the behavior of vortices in a nematic liquid crystal layer under the influence of electric and magnetic field was carried out.

Nematic liquid crystals layer with negative dielectric constant and homeotropic anchoring under the influence of a voltage are the ideal platform for studying the interaction of gas of topological vortices with opposite topological charges. One would expect that the dynamics of the vortices is characterized by a decreasing number in time, which follows a power law with critical exponent $\alpha = 1$, because the dominant interaction between the vortices is self-similar. Unexpectedly, we observe that this dynamics is persistent in thin cells of nematic liquid crystals that contain glass beads as spacers. However, the laws of the exponential decay in the number of vortices depend strongly on the distribution of the glass beads and their imperfections. Experimentally, we have characterized such a dynamics and demonstrated that the deformed glass beads attract vortices of opposite topological charges, presenting mainly a quadrupolar behavior. Theoretically, we have derived the modified power law for inhomogeneous samples, leading to $\alpha = 2/3$ exponent of the power law. The agreement with the exponents derived from the experimental observations is satisfactory over several zones of the analyzed samples. However, a complete agreement could not be reached because of the diversity of the beads and the consequent complexity of the induced vortex dynamics. Liquid crystal cells with spacers are fundamental in the development of displays of various electronic devices. The influence that the disperse beads, often used as spacers in the cell, can exert on the molecular reorientation is usually ignored. Our observations show that the inhomogeneities induced by the beads can play a relevant role in the dynamics of defects. Therefore, the study of the interaction between spacers and the surrounding liquid crystal can reveal important features of molecular behavior and should be taken into account for further improvements of liquid crystal devices.

Exotic states of matter have been found in a system with injection and dissipation of energy. In a nematic liquid crystal cell under the influence of a low frequency oscillatory electric field, topological transitions from no vortex state to vortex state in which vortices persist have been observed. Depending on the frequency and type of the forcing (harmonic, sawtooth, or square profiles), there is a critical frequency in which the vortices self-organize

forming square lattices, glassy states, and disordered vortex structures. To describe these topological transitions, the Ginzburg Landau equation with real coefficients was modified by adding terms of inertia, oscillating bifurcation parameter, and white noise. Numerical simulations of this model described qualitatively well the topological transitions observed and could be a start point for understanding and controlling the exotic states of matter. We continue to work on improving the model to fully describe the observed topological transitions. Because the phenomenon reported here is qualitative well described by a universal model Eq. (3.1), we expect that any temporally modulated vectorial field system of low dimensionality can exhibit topological transitions out of equilibrium. Furthermore, these findings could be a starting point for understanding and controlling the exotic states of matter. Because vortex lattices emerge spontaneously in single cells subjected to alternative low-frequency voltages, it opens up the possibility of new and novel applications of the generation of optical vortices.

The combined effect of the magnetic field of a magnetic ring and the uniform electric field onto a homeotropic nematic liquid crystal cell induces a stable vortex triplet. Based on a Ginzburg Landau equation with real coefficients and topological forcing close to the Fréedericksz transition, it was possible to reveal the origin of this vortex triplet. Numerical simulations of this model show a quite fair agreement between the proposed theory and the experimental observations. Unexpectedly, when the frequency of the applied voltage decrease, the vortex triplet destabilizes and form a stable vortex lattice. To describe the latter, a term of inertia is added to the Ginzburg Landau equation with real coefficients and topological forcing. Numerical simulations show that the proposed model describes qualitatively the experimental observations. This is a recent finding, future studies could improve this model to fully describe the phenomenon. This mechanism of manipulating and controlling vortices may be relevant to the development of optical tweezers and could enable the development of new q-plate technologies.

Thermal fluctuations are responsible for vortices nucleation in a nematic liquid crystal cell. The number of nucleated vortices is described by $N = \frac{A\mu}{\sqrt{(1-\delta^2)}} + C$. Therefore, the number of vortices created when the voltage, noise, and temperature increase and scales with anisotropy as $\sim 1/\sqrt{(1-\delta^2)}$. The amplitude equation allows us to characterize the number of vortices as a function of time scales as a power law whose exponent varies when the bifurcation, anisotropy, and temperature.

Bibliography

[1] Pierre-Gilles De Gennes and Jacques Prost. *The physics of liquid crystals*, volume 83. Oxford university press, 1993.

[2] S Chandrasekhar. Liquid crystals, (1992). *Cambridge University, Cambridge.*

[3] Patrick Oswald and Pawel Pieranski. *Nematic and cholesteric liquid crystals: concepts and physical properties illustrated by experiments*. CRC press, 2005.

[4] Iam-Choon Khoo. *Liquid crystals*, volume 64. John Wiley & Sons, 2007.

[5] Thomas Frisch. Spiral waves in nematic and cholesteric liquid crystals. *Physica D: Nonlinear Phenomena*, 84(3-4):601–614, 1995.

[6] Vsevolod Fréedericksz and V Zolina. Forces causing the orientation of an anisotropic liquid. *Transactions of the Faraday Society*, 29(140):919–930, 1933.

[7] A Rapini. Umbilics: static properties and shear-induced displacements. *Journal de Physique*, 34(7):629–633, 1973.

[8] Len M Pismen and Len M Pismen. *Vortices in nonlinear fields: from liquid crystals to superfluids, from non-equilibrium patterns to cosmic strings*, volume 100. Oxford University Press, 1999.

[9] Marcel G Clerc, Estefania Vidal-Henriquez, Juan Diego Davila, and Michał Kowalczyk. Symmetry breaking of nematic umbilical defects through an amplitude equation. *Physical Review E*, 90(1):012507, 2014.

[10] R Barboza, U Bortolozzo, MG Clerc, Stefania Residori, and Estefanía Vidal-Henriquez. Optical vortex induction via light–matter interaction in liquid-crystal media. *Advances in Optics and Photonics*, 7(3):635–683, 2015.

[11] I Dierking, O Marshall, J Wright, and N Bulleid. Annihilation dynamics of umbilical defects in nematic liquid crystals under applied electric fields. *Physical Review E*, 71(6):061709, 2005.

[12] David L Goodstein. *States of Matter*. Courier Corporation, 1985.

[13] Lev Davidovich Landau. On the theory of phase transitions. i. *Zh. Eksp. Teor. Fiz.*,

11:19, 1937.

[14] Lev Davidovich Landau, Evgenij Mihajlovič Lifšic, Evgenii Mikhailovich Lifshitz, and LP Pitaevskii. *Statistical physics: theory of the condensed state*, volume 9. Butterworth-Heinemann, 1980.

[15] Jorge V Jos. *40 years of Berezinskii-Kosterlitz-Thouless theory*. World Scientific, 2013.

[16] John Michael Kosterlitz and David James Thouless. Ordering, metastability and phase transitions in two-dimensional systems. *Journal of Physics C: Solid State Physics*, 6(7):1181, 1973.

[17] Jonathan Maps and RB Hallock. Experimental study of the kosterlitz-thouless transition in he 4 films. *Physical Review B*, 27(9):5491, 1983.

[18] VL Berezinskii. Violation of long range order in one-dimensional and two-dimensional systems with a continuous symmetry group. *Zh. Eksp. Teor. Fiz.[Sov. Phys–JETP// 59 [32], 907–920 [493–500](1970 [1971])*, 1971.

[19] Andrew N Pargellis, Susannah Green, and Bernard Yurke. Planar xy-model dynamics in a nematic liquid crystal system. *Physical Review E*, 49(5):4250, 1994.

[20] Tomoyuki Nagaya, Hiroshi Orihara, and Yoshihiro Ishibashi. Coarsening dynamics of+ 1 and-1 disclinations in two-dimensionally aligned nematics–spatial distribution of disclinations–. *Journal of the Physical Society of Japan*, 64(1):78–85, 1995.

[21] Atsuyuki Okabe. Spatial tessellations. *International Encyclopedia of Geography: People, the Earth, Environment and Technology: People, the Earth, Environment and Technology*, pages 1–11, 2016.

[22] Claude E Shannon. Xxii. programming a computer for playing chess. *The London, Edinburgh, and Dublin Philosophical Magazine and Journal of Science*, 41(314):256–275, 1950.

[23] Kohki Takatoh, Masanori Sakamoto, Ray Hasegawa, Mitsushiro Koden, Nobuyuki Itoh, and Masaki Hasegawa. *Alignment technology and applications of liquid crystal devices*. CRC Press, 2005.

[24] Holger Stark. Director field configurations around a spherical particle in a nematic liquid crystal. *The European Physical Journal B-Condensed Matter and Complex Systems*, 10(2):311–321, 1999.

[25] Brian Josephson. Possible new effect in superconducting tunneling. *Phys. Lett.*, 1:251–253, 1962.

[26] DJ Bishop and JD Reppy. Study of the superfluid transition in two-dimensional he 4 films. *Physical Review Letters*, 40(26):1727, 1978.

[27] R Barboza, T Sauma, U Bortolozzo, G Assanto, MG Clerc, and S Residori. Characteri-

zation of the vortex-pair interaction law and nonlinear mobility effects. *New Journal of Physics*, 15(1):013028, 2013.

[28] A Abrikosov. The magnetic properties of superconducting alloys j. *Phys. Chem. Solids*, 2:199–208, 1957.

[29] P Pieranski, E Dubois-Violette, and E Guyon. Heat convection in liquid crystals heated from above. *Physical Review Letters*, 30(16):736, 1973.

[30] Yuji Sasaki, VSR Jampani, Chiharu Tanaka, Nobutaka Sakurai, Shin Sakane, Khoa V Le, Fumito Araoka, and Hiroshi Orihara. Large-scale self-organization of reconfigurable topological defect networks in nematic liquid crystals. *Nature communications*, 7(1):1–13, 2016.

[31] LK Migara and Jang-Kun Song. Standing wave-mediated molecular reorientation and spontaneous formation of tunable, concentric defect arrays in liquid crystal cells. *NPG Asia Materials*, 10(1):e459–e459, 2018.

[32] EF Carr. Influence of electric fields on the molecular alignment in the liquid crystal p-(anisalamino)-phenyl acetate. *Molecular Crystals and Liquid Crystals*, 7(1):253–268, 1969.

[33] W Helfrich. Conduction-induced alignment of nematic liquid crystals: basic model and stability considerations. *The Journal of chemical physics*, 51(9):4092–4105, 1969.

[34] T Frisch, S Rica, P Coullet, and JM Gilli. Spiral waves in liquid crystal. *Physical review letters*, 72(10):1471, 1994.

[35] P Coullet and F Plaza. Excitable spiral waves in nematic liquid crystals. *International Journal of Bifurcation and Chaos*, 4(05):1173–1182, 1994.

[36] Igor S Aranson and Lorenz Kramer. The world of the complex ginzburg-landau equation. *Reviews of Modern Physics*, 74(1):99, 2002.

[37] Etienne Sandier and Sylvia Serfaty. *Vortices in the magnetic Ginzburg-Landau model*, volume 70. Springer Science & Business Media, 2008.

[38] Fabrice Bethuel, Haim Brezis, and Frederic Helein. *Ginzburg-Landau Vortices*, volume 13. Springer Science & Business Media, 2012.

[39] Etienne Brasselet, Naoki Murazawa, Hiroaki Misawa, and Saulius Juodkazis. Optical vortices from liquid crystal droplets. *Physical review letters*, 103(10):103903, 2009.

[40] Etienne Brasselet and Charles Loussert. Electrically controlled topological defects in liquid crystals as tunable spin-orbit encoders for photons. *Optics letters*, 36(5):719–721, 2011.

[41] R Barboza, U Bortolozzo, G Assanto, E Vidal-Henriquez, MG Clerc, and S Residori. Vortex induction via anisotropy stabilized light-matter interaction. *Physical review let-*

ters, 109(14):143901, 2012.

[42] Etienne Brasselet. Tunable optical vortex arrays from a single nematic topological defect. *Physical review letters*, 108(8):087801, 2012.

[43] Mohamed El Ketara and Etienne Brasselet. Self-induced nonlinear spin–orbit interaction of light in liquid crystals. *Optics letters*, 37(4):602–604, 2012.

[44] P Pieranski, B Yang, L-J Burtz, A Camu, and F Simonetti. Generation of umbilics by magnets and flows. *Liquid Crystals*, 40(12):1593–1608, 2013.

[45] Etienne Brasselet. Tunable high-resolution macroscopic self-engineered geometric phase optical elements. *Physical review letters*, 121(3):033901, 2018.

[46] Enrique Calisto, Marcel G Clerc, Michał Kowalczyk, and Panayotis Smyrnelis. On the origin of the optical vortex lattices in a nematic liquid crystal light valve. *Optics Letters*, 44(12):2947–2950, 2019.

[47] I. Lebedev. New manifestations of magnetism. *Tekhnika Molodezhi*, 2(6):[see, also, http://n–t.ru/tp/mr/mmk.htm, 1991.

[48] Enrique Augusto Calisto Leiva. Vortices induced by topological forcing in nematic liquid crystal layers. 2019.

[49] Tomoyuki Nagaya, Hideki Hotta, Hiroshi Orihara, and Yoshihiro Ishibashi. Observation of annihilation process of disclinations emerging from bubble domains. *Journal of the Physical Society of Japan*, 60(5):1572–1578, 1991.

[50] Valeska Zambra, Marcel G Clerc, Raouf Barboza, Umberto Bortolozzo, and Stefania Residori. Umbilical defect dynamics in an inhomogeneous nematic liquid crystal layer. *Physical Review E*, 101(6):062704, 2020.

[51] Crispin W Gardiner et al. *Handbook of stochastic methods*, volume 3. springer Berlin, 1985.

Appendix A
Coarsening Dynamics of Umbilical Defects in Inhomogeneous Medium

Publication Details

- Title: Coarsening Dynamics of Umbilical Defects in Inhomogeneous Medium
- Author: Raouf Barboza, Umberto Bortolozzo, Marcel G. Clerc, Stefania Residori and Valeska Zambra
- Published in: Nonlinear Dynamics: Materials, Theory and Experiments. Springer Proceedings in Physics, vol 173. Springer, Cham
- DOI: `https://doi.org/10.1007/978-3-319-24871-4_2`

Coarsening Dynamics of Umbilical Defects in Inhomogeneous Medium

Raouf Barboza, Umberto Bortolozzo, Marcel G. Clerc, Stefania Residori and Valeska Zambra

Abstract Non-equilibrium systems with coexistence of equilibria exhibit a rich and complex defects dynamics in order to reach a more stable configuration. Nematic liquid crystals layer with negative dielectric constant and homeotropic anchoring under the influence of a voltage are the ideal context for studying the interaction of gas of topological vortices. The number of vortices decreases with time. Experimentally, we show that the presence of imperfections drastically changes this coarsening law. Imperfections are achieved by considering glass beads inside the nematic liquid crystal sample. Depending on the disorder of these imperfections, the system exhibits different statistical evolution of the number of umbilical defects. The coarsening dynamics is persistent and is characterized by power laws with different exponents.

1 Introduction

Macroscopic systems under the influence of injection and dissipation of energy and momenta exhibit instabilities leading to spontaneous symmetry breaking and pattern

R. Barboza (✉) · M.G. Clerc
Departamento de Física, Facultad de Ciencias Físicas Y Matemáticas,
Universidad de Chile, Casilla 487-3, Santiago, Chile
e-mail: raouf.barboza@ing.uchile.cl

M.G. Clerc
e-mail: marcel@dfi.uchile.cl

U. Bortolozzo · S. Residori
Institut Nonlinéaire de Nice, Université de Nice-Sophia Antipolis, CNRS,
1361 Route des Lucioles, 06560 Valbonne, France
e-mail: umberto.bortolozzo@inln.cnrs.fr

S. Residori
e-mail: stefania.residori@inln.cnrs.fr

V. Zambra
Departamento de Física, Facultad de Ciencias, Universidad de Chile, Santiago, Chile
e-mail: valesk.za@gmail.com

M. Tlidi and M.G. Clerc (eds.), *Nonlinear Dynamics: Materials, Theory and Experiments*, Springer Proceedings in Physics 173,
DOI 10.1007/978-3-319-24871-4_2

formation [1]. Due to the inherent fluctuations of these macroscopic systems, different organizations may emerge in distinct regions of the same sample; hence, these spatial structures are usually characterized by domains, separated by interfaces, as grain boundaries, and defects or dislocations [2, 3]. Among others, defects in rotationally invariant two dimensional systems, i.e. vortices, attract a great deal of attention because of their universal character and intriguing topological properties. These defects have been observed in different systems such as fluids, superfluids, superconductors, liquid crystals, fluidized anisotropic granular matter, magnetic media, and optical dielectrics, to mention a few [4]. Vortices occur in complex fields and can be identified as topological defects, that is, point-like singularities which locally break rotational symmetry. They exhibit a zero intensity at the singular point with a phase spiraling around it. The topological charge is assigned by counting the number of spiral arms in the phase distribution, while the sign is given by the sense of the spiral rotation.

Nematic liquid crystals with negative anisotropic dielectric constant and homeotropic anchoring are a natural physical context where dissipative vortices can be observed and analyzed [5, 6]. In this context, the dissipative vortices are usually called umbilical defects. These defects in nematic liquid crystals have long been reported in the literature (see textbooks [5–7] and reference therein). Two types of stable vortices with opposite charges are observed, which are characterized by being attracted to (repelled by) the opposite (identical) topological charge. The nematic liquid crystal phase is characterized by rod-shaped molecules that have no positional order but tend to point in the same direction [5–7]. Then, the description of the nematic liquid crystal is given by a vector—the director **n**—which accounts for the molecular orientational order. The direction of this vector is irrelevant, only the orientation of **n** has a physical meaning. Note that the defects observed in this context are similar to those observed in magnetic systems, superfluids, superconductors, and Bose-Einstein condensates. However, these vortices exhibit a entirely different dynamic evolution due to the strongly dissipative nature of liquid crystals.

The vortex-like defects have accompanied liquid crystals since their discovery in 1889 by Lehmann [8], who called these structures *kernel*. Later, they were observed in a similar experimental setup by Friedel, who called them *noyaux* [9]. Moreover, he also resolved their detailed topological structure. From the theory of elasticity of nematic liquid crystals, Frank calculated the detailed structure of these defects [10]. Due to the fact that these defects break the orientational order and by analogy with dislocations in crystals of condensed matter, Frank called these defects *disclinations*. Despite the different names given to the observed vortices in this context, none of them were adopted by the community of liquid crystals. There the most widely used name for these defects is *nematic umbilical defects*. The term umbilics was coined by Rapini [11] and refers to the topological structure of the defect which corresponds to a string-like object in three dimensions. Because of the complex elasticity theory associated with nematic liquid crystals, characterized by three types of deformation (bend, twist and splay), the theoretical dynamic study of defects is a thorny task [5–7].

Based on weak nonlinear analysis, valid close to the orientational instability of the molecules (Fréedericksz transition [5, 6]), the dynamics of the director can be reduced at main order to the Ginzburg-Landau equation with real coefficients [12–14]. This amplitude equation allows to understand the emergence of different orientational domains, two types of stable vortices and their respective dynamics. Since the vortices have a $\pm 2\pi$ azimuthal phase jump (winding number), usually they are referred to as vortex "+" and "−", respectively. In this approach, both defects are indistinguishable in their amplitude and, as a result of the phase invariance of the Ginzburg-Landau equation, they account for a continuous family of solutions, characterized by a phase parameter [4]. From this model one can characterize the interaction of vortex pairs [4], which shows a good agreement with experimental observations [15]. From the interaction of defect pairs and through the use of self similarity statements, one can infer the law of number of defects as a function of time [16, 17]. This type of self-similar behavior is well-known as *coarsening process*, which is equivalent to the growth process of domains in phase separations transitions observed in metallic alloys [18]. Using the law of vortices interaction, one shows that the number of defects decreases inversely proportional to time, which it has been experimentally observed in nematic liquid crystal samples [19, 20]. Similarly, using XY phase model, one obtains the same decay law for the vortices number [19].

The aim of this manuscript is to investigate experimentally the persistence and coarsening law when inhomogeneities are considered in a liquid crystal sample. The inhomogeneities are achieved by considering glass beads inside a nematic liquid crystals sample with negative dielectric constant and homeotropic anchoring. Depending on the disorder of these glass beads, the system exhibits different statistical temporal evolution of number of umbilical defects. This evolution is found to exhibit power laws with different exponents.

2 Experimental Setup

Let us consider an interaction geometry in which, a uniform thin layer of nematic liquid crystal has the molecular director constrained to be normal to the two parallel bounding plates, direction which we later denote by z. Due to inherent elastic forces between the molecules, the alignment in the bulk will be uniform and parallel to z, this in order to minimize the elastic energy. When a low frequency ($\approx$100 kHz in our case) electric field is applied in the z direction, if the dielectric anisotropy of the liquid crystal is negative, the resulting electric torque will try to rotate the molecules away from the z-axis. Only over a critical threshold voltage, called Fréedericksz transition voltage [6], the molecules effectively tilt away from their equilibrium position. Due to the 2π degeneracy in the possible direction of orientation, defects called umbilics will be generated in the nematic layer [6, 11].

The observation of these umbilical defects and their dynamics was done by using two different types of liquid crystal cells about the same thickness. The first cell, uniform, is made of two ITO (Indium Tin Oxide, transparent conductor) coated glass

Fig. 1 Sketch of the experimental setup of a nematic liquid crystal layer with negative dielectric constant anisotropy and homeotropic anchoring under the influence of a voltage. The essential parts of the setup are emphasized. Crossed polarizers, either linear or circular are used to analyze the texture of the liquid crystal

slabs. The glass slabs are treated on the ITO side in order to promote orthogonal alignment of the liquid crystal molecules. This alignment is termed as homeotropic alignment or homeotropic anchoring [5–7]. The glass slabs are held together with thin sheet of polymer spacers such that, the treated faces form a gap in which the liquid crystal will be infiltrated later. The spacers, which fix the thickness of the gap are about 15 μm thick. The second cell, non uniform, from Instec Inc. (SB100A150uT180 liquid crystal cell), has the same homeotropic alignment. The spacing gap of the cell is achieved by sputtering spacer beads made of clear/transparent ceramics or glass onto the substrate of glass slab before assembly [21]. The diameter of these glass micro-spheres fixes the cell gap, and, for the chosen cell, it is about 15 μm. The two cells were filled by capillarity with the MLC-6608 nematic liquid crystal (from Merck) which has a negative dielectric anisotropy. Both cells are biased with low frequency sinusoidal voltage. The experimental setup is sketched in the figure Fig. 1. To achieve maximum resolution, a collimated white light (Köhler illumination) from a microscope condenser is sent onto the liquid crystal cell, the latter mounted on a translation stage. The texture of the liquid crystal is imaged on a CCD camera through a microscope objective and relay lenses.

As the cells contain liquid crystalline materials, which are an intrinsically birefringent in the nematic phase, two crossed polarizers, the first to polarize the illumination source and the second to analyze the polarization of the light coming from the cell, are used in order to recover averaged two dimensional texture of the liquid crystal layer. For simplicity the cell will be considered as a uniform, along the longitudinal z coordinate, uniaxial birefringent material with optical axis aligned in the xy plane at angle θ with the x axis, with retardation $\delta = 2\pi L(\tilde{n}_e - n_o)/\lambda$; L represents the thickness of the cell, λ the operating wavelength, n_o and $\tilde{n}_e$ respectively the ordinary refractive index and the average extraordinary refractive index over the longitudinal coordinate. The optical axis can be viewed as the averaged azimuthal direction of molecules in the xy plane, equivalently their projection onto the xy plane. The averaged extraordinary index $\tilde{n}_e$ is related to the tilt ψ of the molecules with respect the z axis by the expression

$$\tilde{n}_e = \int_0^L \frac{n_e n_o}{\sqrt{n_e^2 \cos^2 \psi + n_o^2 \sin^2 \psi}} dz. \tag{1}$$

The texture of the liquid crystal layer will vary accordingly with the spatial variation in the xy optical axis at angle θ representing the director orientation in the xy plane and δ the retardation which depends on the average tilt ψ of the molecules with respect to the z axis. Using Jones matrix formalism we can show that the intensity recorded using crossed linear polarizers, the polarizers axis are perpendicular to each other, is given by

$$I(x, y) = I_0 \sin^2 \frac{\delta(x, y)}{2} \sin^2 2\theta(x, y). \tag{2}$$

Likewise, the crossed circular polarizer configuration is achieved when two quarter wave plate (QWP) are inserted in the previous configuration, with the first waveplate at $\pm 45°$ with respect to the axis of the input polarizer, and the fast axis of the second wave-plate is orthogonal to the first one. In this case the recorded intensity writes as follow

$$I(x, y) = I_0 \sin^2 \frac{\delta(x, y)}{2} \tag{3}$$

We used both polarizing microscope imaging, depending on the feature we want to enhance of the umbilical defects dynamics.

3 Results and Discussions

To understand the coarsening dynamics of the vortices in homogeneous cell, we must first establish the vortex pair interaction law and then, by means of self-similarity properties, we can deduce a coarsening law of vortices.

3.1 Vortex-Pair Interaction Law

As we have mention before, close to the orientational instability of the molecules, the dynamics of the director can be reduced at main order to the Ginzburg-Landau equation with real coefficients. This amplitude equation admits stable vortex solutions with topological charge ± 1. The analysis of the vortex interaction law is complex because the energy associated with each vortex diverges logarithmically with the size of the system [5]. Thereby, the interaction between distant vortices has an infinite mobility [4]. However, in the case of considering that the system has a finite size, the mobility is finite and the vortex-pair interaction law can be approximated for long distances by the expression [4]

$$M\dot{r} = \frac{q}{r}, \tag{4}$$

where $r(t)$ is the vortex separation, q is the product of the topological charges of vortices ($q = \pm 1$), then it is positive (negative) when both vortex has the same (different) charge, and M stands for the vortex mobility which depends of the size of the system, the properties of the liquid crystal and the applied voltage. Thus the interaction between vortices is equivalent to overdamped particles with Keplerian type interaction potential. When the distances between the vortices is small enough—the order of the size of the vortex core—the previous dynamics is not valid. But in this case, vortices of opposite charge merge and disappear. In brief, the dynamics of interaction between vortices tries to homogenize the deformations of molecular orientation.

3.2 Vortex Coarsening Law

Considering a gas of n-vortices, the position of the ith-vortex is given by $\mathbf{r}_i$. Hence, the interaction between them is given by

$$M\dot{\mathbf{r}}_i = \sum_{i \neq j} \frac{q_{ij}}{r_{ij}^2}(\mathbf{r}_i - \mathbf{r}_j), \tag{5}$$

where $r_{ij} \equiv ||\mathbf{r}_i - \mathbf{r}_j||$ is the distance between the ith and jth-vortex, and q_{ij} is the product of the topological charges of vortices. Hence, the dynamics of a gas of n-vortices corresponds to overdamped n-body problem. It is worthy to note the above set of equations is invariant under the self-similarity transformation

$$\begin{aligned} \mathbf{r}_i &\to \lambda \mathbf{r}_i, \\ t &\to \lambda^2 t. \end{aligned} \tag{6}$$

Therefore, if one dilates or expands the space and time then the set of (5) are invariant.

Let us introduce $N(t)$, the number of vortices at time t. This number of vortices can be estimated as

$$N(t) = \frac{A}{\langle r \rangle^2}, \tag{7}$$

where A is the area of the sample under study and $\langle r \rangle$ is the average distance between vortices. Because the dynamics of vortices is given by the set of (5), also the average distance $\langle r \rangle$ and $N(t)$ is determined by this dynamics. Then, $\langle r \rangle$ and $N(t)$ should

also be self similar with transformation (6). Hence, $N(\lambda^2 t) = A/\lambda\langle r\rangle^2$. From the previous equality, one infers that the only possibility is that

$$N(t) = \frac{\beta}{t}, \tag{8}$$

with β a constant. Therefore, the number of defects decreases inversely proportional to time, *coarsening law*.

3.3 Experimental Observation of Coarsening Law in Uniform Cell

To verify the previous law, we have conducted several experimental analysis of the dynamics of vortex gas. This by applying a large enough voltage to the liquid crystal layer between two cross polarizers, which spontaneously generates hundreds umbilical defects in different positions as a result of thermal fluctuations and inhomogeneities in the system. The position of the umbilical defects are recognized by the intersection of four black curves [5]. Subsequently, the defects have a dynamic of attraction and repulsion following the interaction law (5). Figure 2 shows a temporal sequence of snapshots, which emphasizes the characteristic evolution of a gas of umbilical defects. From the temporal sequences and through an appropriate recognition software we can determine the number of vortices and their respective positions. Thus, we acquire the evolution of the number of vortices as a function of time. Figure 3 shows this evolution. From this plot, one concludes that the number of

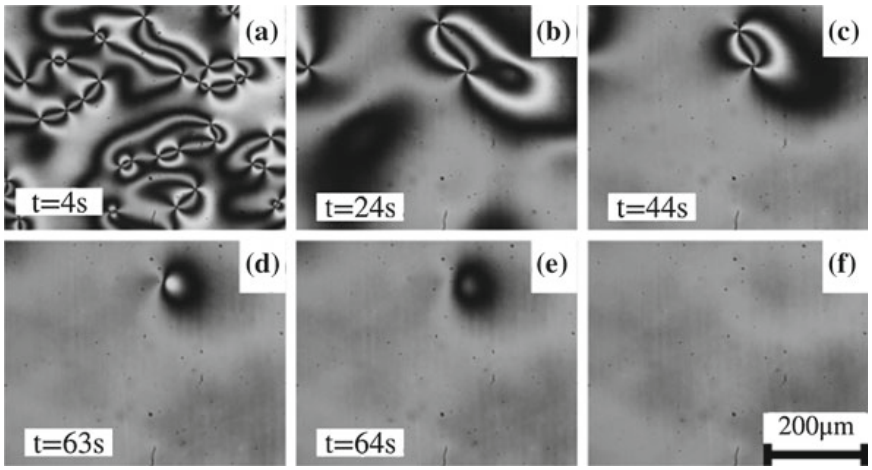

Fig. 2 Annihilation dynamics of umbilical defects in a uniform liquid crystal layer between two crossed linear polarizers. Temporal sequence of snapshots from the *left* to *right* and the *top* to *bottom* (**a**–**e**). The position of the umbilical defects are given by the intersection of four *black brushes*. Texture of the sample after the anihilation of all the defects (**f**)

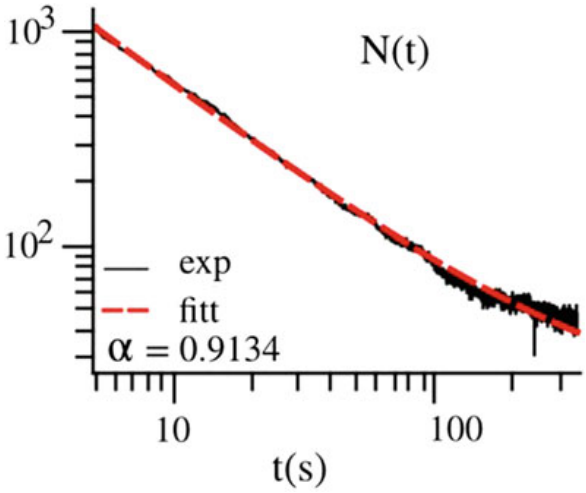

Fig. 3 Coarsening dynamics in a uniform cell. Number of umbilical defects as a function of time. The *solid black* and *dashed curve*, respectively, are the experimental evolution of $N(t)$ and the fitting *curve* $N_f(t) = \beta t^{-\alpha} + N_\infty$ with $\alpha = 0.9134 \pm 0.00124$, $\beta = 4.448 \times 10^3 \pm 10$ and $N_\infty = 17 \pm 0.22$

vortices decays as a function of time with a power law. To determine the exponent, we have considered the following fit

$$N_f(t) = \beta t^{-\alpha} + N_\infty, \tag{9}$$

where $\{\beta, \alpha, N_\infty\}$ are fitting parameters, which accounts for the features of the liquid crystal and cell under study. N_∞ stands for the number of imperfections of the system—which trap the vortices in given positions—and the inaccuracy of recognition method. Experimentally we found that in our samples, the exponent $\alpha = 0.9134$ is in reasonable agreement with the simplified description (5).

3.4 Experimental Observation of Coarsening Law in Inhomogeneous Cell

To investigate of the interaction of vortices in inhomogeneous media, we have conducted several experimental analysis of the dynamic of vortex gas in a liquid crystal layer with glass beads between two cross polarizers and applying a large enough voltage. Figure 4 shows a temporal sequence of snapshots with the characteristic evolution of a gas of umbilical defects in an inhomogeneous medium. The glass beads are emphasized by dashed circumferences. Again, the position of the umbilical defects are recognized by the intersection of four black curves. As we have observed in the temporal sequence of snapshots, when one applies a sufficiently large voltage in the liquid crystal layer a large number of vortices appear in different spatial positions, which are determined by the inherent fluctuations and imperfections in the cell. Following the emergence of these umbilical defects, they begin to repel or attract, causing the annihilation process of these defects. This process is characterized by the fact that initially close defects annihilate quickly, and then the more distant umbilical defects annihilate one another, but each time in a slower process, coarsening

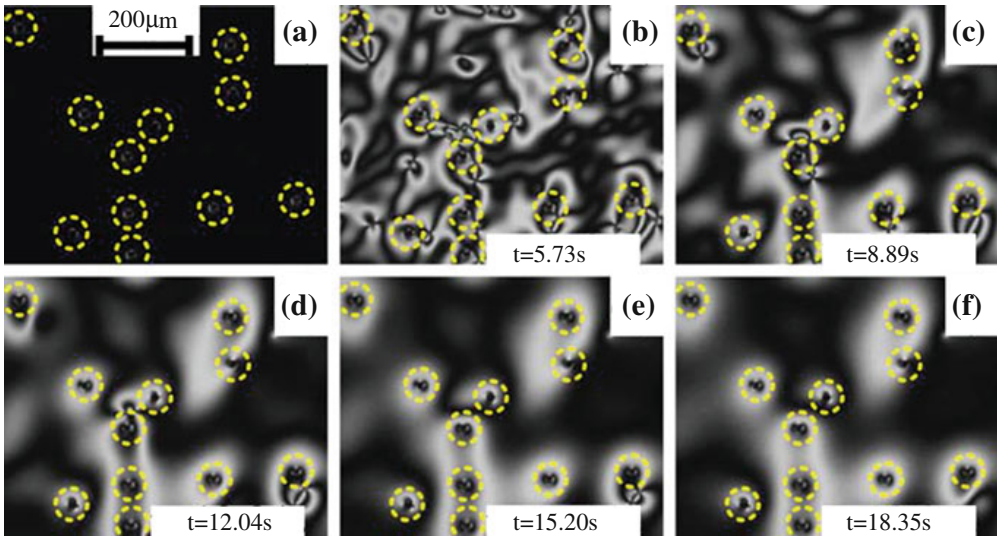

Fig. 4 Umbilical defects annihilation dynamics in a liquid crystal layer with glass beads between two linear crossed polarizers. Temporal sequence of snapshots from the *left* to *right*. The position of the umbilical defects are given by the intersection of four *black curves*

dynamics. The glass beads, as seen in the snapshots, remain motionless. However, the dynamics of vortices is strongly affected by the presence of glass beads. Figure 5 shows a glass bead attracting radially an umbilical defect . Both appear as dark spots as the cell is observed with circular crossed polarizers. In this experimental setup umbilical defects are recognized as small gray circles. Experimentally, this interaction is weaker than the interaction between umbilical defects. It is known that glass beads without surface treatment, generate homeotropic anchoring at their boundaries, that the liquid crystal molecules tend to be oriented normal to the glass beads [21, 22]. In addition, due to the fact that the glass beads are in contact with the glass plates of the sample, one expects a saturn ring like defect loop around each glass inclusion [21, 22]. The trajectory as consequence of the interaction between this defect and the umbilical one is depicted in Fig. 5. Likewise, the interactions between vortices are affected by the presence of the glass beads. Figure 6 illustrates the vortex interaction in presence of a close glass bead in a liquid crystal layer observed with circular crossed polarizers. Clearly from this trajectory, we note that the interaction of the umbilical defects is not a central force as those obtained by (4). Therefore, the interaction of vortices is modified and it is not clear if the process of coarsening is persistent.

Using an appropriate recognition software, based on particle tracking, we can determine the number of vortices and their respective positions. Figures 7c and 8c show the evolution of the number of umbilical defects as a function of time. In both graphs, we observe that the system exhibits coarsening process with power laws. These power laws are obtained by realizing several experiments. Hence, the coarsening dynamics is a persistent phenomenon, though depending on the distribution of the glass beads, we observe different power laws. To characterize the clustering

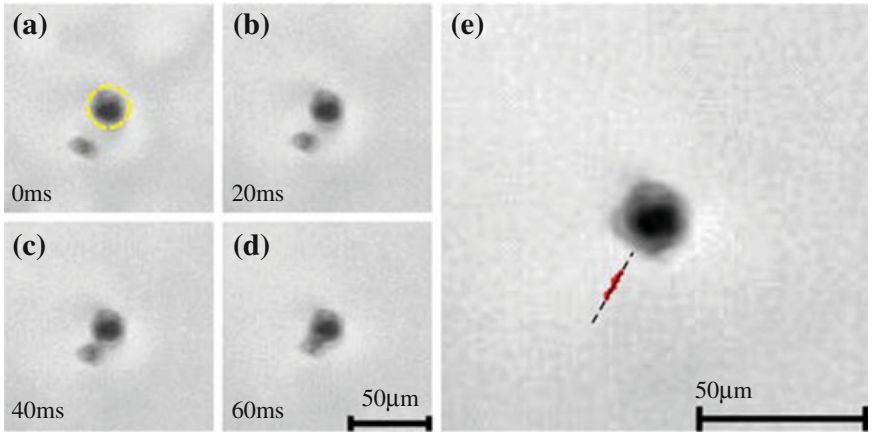

Fig. 5 Interaction between a glass bead and an umbilical defect in a liquid crystal layer with circular crossed polarizers. Temporal sequence of snapshots from (**a**) to (**e**). *Dashed circle* accounts for the glass bead. The small *gray circle* stands for the umbilical defect. In the *right panel*, the *dashed line* sums up the trajectory of the umbilical defect and points are the position of the defect

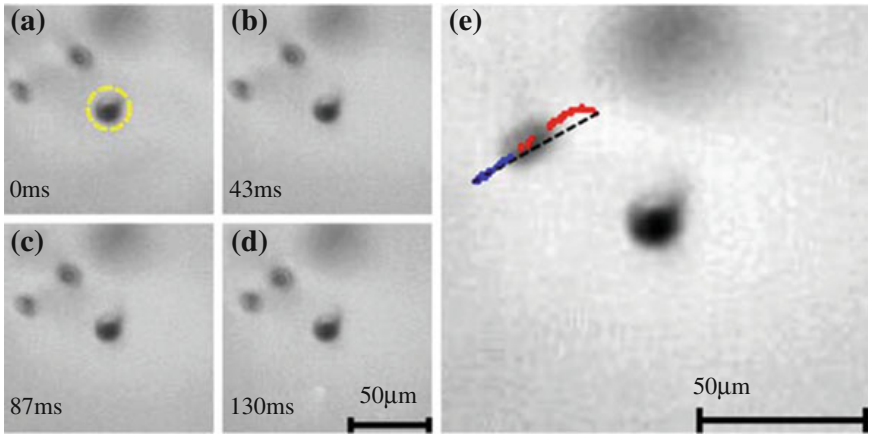

Fig. 6 Vortex interaction in presence of a glass bead in a liquid crystal layer with circular crossed polarizers. Temporal sequence of snapshots from (**a**) to (**e**). *Dashed circle* accounts for a glass bead. The small *gray circle* stands for the umbilical defects. In the *right panel*, the color points account for the trajectories of the umbilical defects, different colors account for the different defects, and the *dashed line* joints initially the defects

and distribution of the glass beads, we have computed the Voronoi diagram of glass beads in the different observed zones (cf. Figs. 7a and 8a) and their histogram of the mutual distance of the glass beads (cf. Figs. 7b and 8b). From these diagrams, we can measure the density of glass beads and we obtain for zone I and III, respectively, 13.630 and 20.803 glass beads per mm^2. Zone III is more ordered than zone I, since its histogram of the mutual distance is closer to a Rayleigh distribution around a length (cf. Fig. 7b) and the other is closer to a uniform distribution without a feature length. Analogously, from this distribution we can compute the Shannon entropy

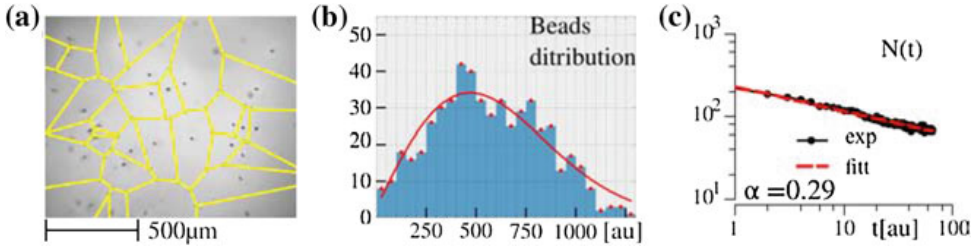

Fig. 7 Coarsening process of umbilical defects in an inhomogeneous medium, zone III. **a** Voronoi diagram of glass beads in the observed zone. **b** Histogram of the mutual distance of the glass beads. The *solid curve* is a fitting curve using a Rayleigh distribution. **c** Corresponding scaling curve of the number of defects vs normalized time. *Black* points stand for experimental observations and the *dashed line* corresponds to a fitting curve of the form $N(t) = \beta/t^{\alpha}$ with $\alpha = 0.29$

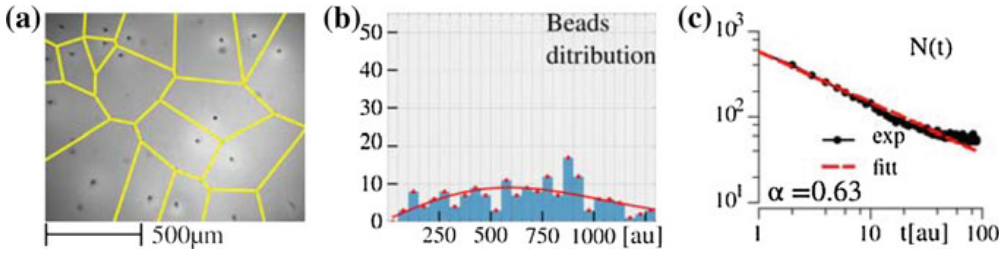

Fig. 8 Coarsening process of umbilical defects in an inhomogeneous medium, zone I. **a** Voronoi diagram of glass beads in the observed zone. **b** Histogram of the mutual distance of the glass beads. The *solid curve* is a *fitting curve* using a Rayleigh distribution. **c** Corresponding scaling *curve* of the number of defects vs normalized time. *Black* points stand for experimental observations and the *dashed line* corresponds to a *fitting curve* of the form $N(t) = \beta/t^{\alpha}$ with $\alpha = 0.63$

S_e and obtain for each zone, respectively $S_e(III) = 0.00767$ and $S_e(I) = 0.021$. Therefore, depending on the different configurations of the glass beads, the evolution of the number of defects as a function of time changes.

To measure the exponent of the coarsening laws, we have considered the following fitting curve $N(t) = \beta t^{-\alpha}$. Table 1 summarizes our results for different zones of our liquid crystal layer. Different zones of the sample exhibit different coarsening laws. However, from this table we are not able to establish a correlation between the

Table 1 Results over an observed area about 1.394 mm^2

Zone	Density (mm^2)	α	β	Entropy
I	13.630	0.63	597.0	0.0210
II	17.217	0.85	1800.0	0.0136
III	20.803	0.29	228.1	0.00767
IV	21.521	0.75	1286.0	0.0091
V	23.673	0.758	1286.0	0.00772
VI	27.977	0.73	187.0	0.0057

density of vortices, Shannon entropy, and spatial distributions with their coarsening exponents found experimentally.

4 Conclusions and Remarks

Far from equilibrium systems with coexistence of equilibria exhibit a rich and complex defects dynamics in order to reach a more stable configuration. This dynamic of defects can generate a rich variety of spatial textures. Defects in rotationally invariant two dimensional systems, attract a great deal of attention because of their universal character and intriguing topological properties. Nematic liquid crystals layer with negative dielectric constant and homeotropic anchoring under the influence of a voltage are the ideal context for studying the interaction of gas of topological vortices with opposite charges.

By considering a uniform sample of nematic liquid crystal layer under the influence of electrical voltage with high frequency, we observe that the number of vortices decrease inversely proportional to time. This coarsening dynamics results when vortices are more close, the interaction between them increases in a self-similarity manner. Experimentally, we show that the presence of imperfections in the liquid crystal layer drastically changes this coarsening process. Imperfections are achieved by considering glass beads inside the nematic liquid crystal sample. We observed that the coarsening process is persistent under the presence of spatial inhomogeneities. Depending on the disorder of these imperfections, the system exhibits different statistical evolution of number of umbilical defects. This evolution is characterized by power laws with different exponents.

From the theoretical point of view, one can model the effect of the glass beads as a screening effect, that is, the law of interaction of pairs of vortices, (4), is modified by considering an effective exponent, which is a function of the properties and distributions of the glass beads. This kind of effective dynamic is self-similar, then this could explain the observed coarsening dynamics.

Acknowledgments M.G.C. acknowledges the support of FONDECYT N 1150507. R.B. acknowledges the support of FONDECYT POSTDOCTORADO N. 3140577.

References

1. G. Nicolis, I. Prigogine, *Self-Organization in Non Equilibrium Systems* (Wiley, New York, 1977)
2. L.M. Pismen, *Patterns and Interfaces in Dissipative Dynamics* (Springer Series in Synergetics, Berlin, 2006)
3. M.C. Cross, P.C. Hohenberg, Pattern formation outside of equilibrium. Rev. Mod. Phys. **65**, 851–1112 (1993)
4. L.M. Pismen, *Vortices in Nonlinear Fields* (Clarendon press, Oxford, 1999)

5. S. Chandrasekhar, Liquid Crystals (Cambridge University Press, Cambridge, 1992)
6. P.G. de Gennes, J. Prost, The physics of Liquid Crystals, 2nd edn. (Oxford Science Publications, Clarendon Press, Oxford, 1993)
7. P. Oswald, P. Pieranski, Nematic and Cholesteric Liquid Crystals (Taylor & Francis Group, Boca Raton, 2005)
8. O. Lehmann, Über fliessende krystalle. Zeitsch Phys. Chem. 4, 462-472 (1889)
9. G. Friedel, The mesomorphic states of matter. Ann. Physique **18**, 273–474 (1922)
10. F.C. Frank, I. Liquid crystals. On the theory of liquid crystals. Discuss. Faraday Soc. 25, 19-28 (1958)
11. A. Rapini, Umbilics: static properties and shear-induced displacements. J. Physique **34**, 629–633 (1973)
12. T. Frisch, S. Rica, P. Coullet, J.M. Gilli, Spiral waves in liquid crystal. Phys. Rev. Lett. **72**, 1471–1474 (1994)
13. T. Frisch, Spiral waves in nematic and cholesteric liquid crystals. Phys. D **84**, 601–614 (1995)
14. M.G. Clerc, E. Vidal-Henriquez, J.D. Davila, M. Kowalczyk, Symmetry breaking of nematic umbilical defects through an amplitude equation. Phys. Rev. E **90**, 012507 (2014)
15. R. Barboza, T. Sauma, U. Bortolozzo, G. Assanto, M.G. Clerc, S. Residori, Characterization of the vortex-pair interaction law and nonlinear mobility effects. New J. Phys. **15**, 013028 (2013)
16. M. Argentina, M.G. Clerc, R. Rojas, E. Tirapegui, Coarsening dynamics of the one-dimensional Cahn-Hilliard model. Phys. Rev. E **71**, 046210 (2005)
17. M.G. Clerc, S. Coulibaly, L. Gordillo, N. Mujica, R. Navarro, Coalescence cascade of dissipative solitons in parametrically driven systems. Phys. Rev. E **84**, 036205 (2011)
18. L. Ratke, P.W. Voorhees, Growth and Coarsening: Ostwald Ripening in Material Processing (Springer Science and Business Media, 2013)
19. A.N. Pargellis, S. Green, B. Yurke, Planar XY-model dynamics in a nematic liquid crystal system. Phys. Rev. E 49, 42504257 (1994)
20. T. Nagaya, H. Orihara, Y. Ishibashi, Coarsening dynamics of +1 and -1 disclinations in two-dimensionally aligned nematics-spatial distribution of disclinations. J. Phys. Soc. Japan, 64, 7885 (1995)
21. M. Hasegawa, Alignment Technology and Applications of Liquid Crystal Devices (CRC Press), pp. 7–54
22. H. Stark, Director field configurations around a spherical particle in a nematic liquid crystal. Eur. Phys. J. B 10, 311321 (1999)

Appendix B

Vortex and glass bead interaction in nematic liquid crystal layer

Publication Details

- Title: Vortex and glass bead interaction in nematic liquid crystal layer
- Author: Valeska Zambra
- Published in: Journal of Physics: Conference Series
- DOI: 10.1088/1742-6596/1043/1/012005

Vortex and glass bead interaction in nematic liquid crystal layer

To cite this article: V. Zambra 2018 *J. Phys.: Conf. Ser.* **1043** 012005

IOP Conf. Series: Journal of Physics: Conf. Series **1043** (2018) 012005 doi:10.1088/1742-6596/1043/1/012005

Vortex and glass bead interaction in nematic liquid crystal layer

V. Zambra

Departamento de Física, Facultad de Ciencias, Universidad de Chile, Santiago, Chile

E-mail: valeska.zambra@ug.uchile.cl

Abstract. An homeotropically aligned liquid crystal layer driven by external electric or magnetic fields exhibit an intricate network of defects called *umbilics* or vortexes. Here, we report an experimental characterization of vortexes-glass bead interaction in nematic liquid crystal layer. The glass spheres, embedded in the liquid crystal, are found to be of two type: some of them attractive, with different strength of attraction; and most of them non-attractive. The attractive glass spheres pull the vortexes so that the distance decays approximately with the square root of time. The glass bead sphere induces an anisotropic force on the vortex. This force can be well approximate by an inverse power law of the distance between vortex and glass bead with exponent 3/4. The vortexes are attracted to a polar region of the attractive glass bead.

1. Introduction

Nematic liquid crystal layers with negative anisotropy and homeotropic anchoring under the influence of an external voltage can exhibit complex spatiotemporal dynamics textures [1]. The critical voltage from which one observes this intriguing dynamics is usually denominated as the Fréedericksz voltage [1, 2, 3]. Above the Fréedericksz voltage the liquid crystal molecules change their orientation. This phenomenon is a result of the imbalance between the intrinsic elastic torque and electric torque resulting from the applied field. Indeed, the electric field forces the molecules to reorient in orthogonal directions. In opposition, the elastic coupling tends to restore the molecules in the electric field direction. Hence, the molecules can be oriented with different direction with the similar angle with respect to the electric field, generating an overall highly nonuniform texture.

To monitor this texture, one can consider crossed linear polarizers. Figure 1 shows the typical *Schlieren*-like texture, where the dark brushes account for directions where the optical axis, to be precise the averaged direction of the molecule in the plane of the cell, parallel or orthogonal to either the polarizer or the analyzer. The dark brushes meet at the defects, *umbilical defects* [1, 2]. Around this defect, when one circles clockwise, the molecules rotate clockwise or anti-clockwise. From the mathematical point of view, these defects correspond to topological singularities of the averaged 2-D projection of the molecules onto the plane of the cell, which usually are named vortexes [4, 5]. Defects with molecules rotating in clockwise (anti-clockwise) sense are termed positive (negative) charge vortexes. Figure 1 depicts the umbilical defects with different topological charge. Indeed, the the spatiotemporal dynamics of the texture is governed by the dynamics of the vortexes. In the last decades the vortex dynamics have been study theoretical

and experimentally in details [4, 5, 6, 7]. The vortex dynamics are characterized by attraction (repulsion) between opposite (equal) charged vortexes. When the vortexes with opposite charge collide, they are annihilate and disappear [4, 6, 8]. An unified theory of these defects is based on the Ginzburg-Landau equation with real coefficients [4, 5, 9]. Based on this description, one can show that the pair interaction law of vortex is governed by a force, inversely proportional to the distance between the vortexes at a dominant order. A thorough study of the vortex interaction is performed in Ref. [8].

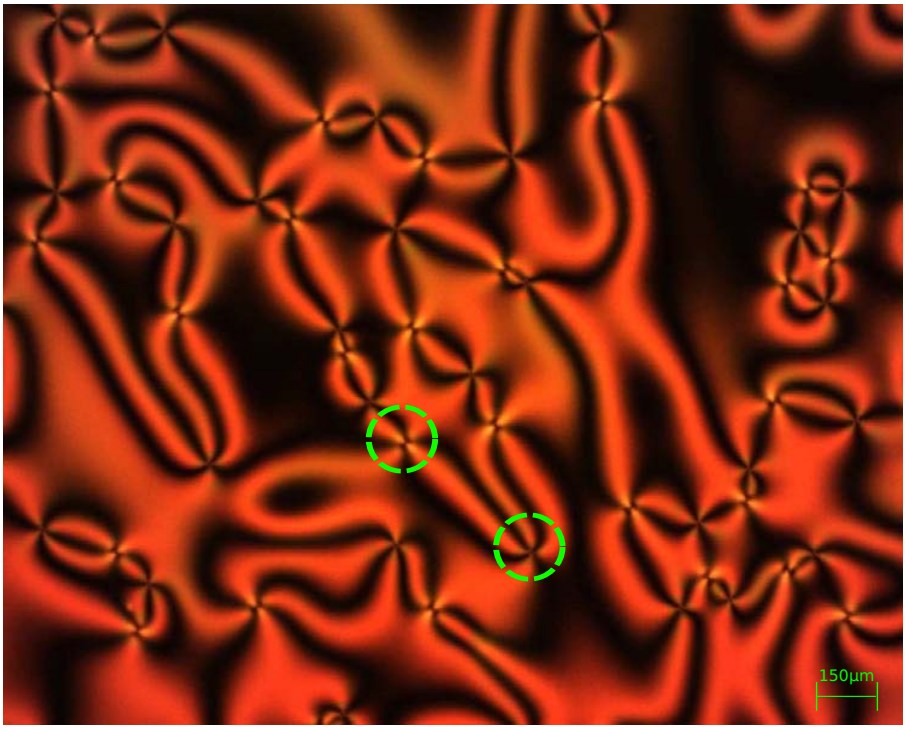

Figure 1. Gas of defects obtained from a biased uniform homeotropically aligned nematic liquid crystal layer. The dashed circumferences account for opposite topological charges. The optical micrograph is obtained using an Olympus BX51 microscope with crossed linear polarizers.

To study experimentally the umbilical defects dynamics, one can consider a nematic liquid crystal layer with negative anisotropy dielectric constant and homeotropic anchoring. To keep the thickness of the cell and avoid cell plates buckling, often one can use randomly distributed glass spheres between cell plates. These spheres are mono-disperse and have approximately the same diameter as the thickness of cell. It could be expected that the presence of glass beads does not affect the vortex dynamics. However, recently it has been shown that these glass beads change the average defects dynamics [10].

In this manuscript, the vortex-glass bead interaction is experimentally characterized. The glass bead have been found to be attractive or non-attractive. We observed that not all glass beads are attractive, at least for the sample and the regions of the sample so far observed, there are more non-attractive beads than attractive ones. The attractive glass bead approximatively pull the vortexes so that the distance decays with the square root of time. Hence, the glass bead induces a force on the vortex proportional to an inverse power law of the distance between them with exponent 3/4. This dynamics is not isotropic, that is, the vortexes are attracted and

annihilated to a polar region of the sphere.

2. Experimental Setup

We have considered a cell, 5B100A150UT180, manufactured by Instec. The cell is filled by capillarity with MLC − 6608 nematic liquid crystal that has negative anisotropy. The inner walls of this cell are chemically treated so that the molecules of liquid crystal are orthogonally aligned to the cell plates. This configuration is usually named *homeotropic anchoring* [1]. The glass plates of the cell have 15 μm of separation between them. To keep the thickness of the inner gap between the glass plates fixed, the cell is filled with monodisperse glass beads (clear/transparent ceramics) which are randomly distributed in the sample. The sample of liquid crystal is subjected to an external electric field in the vertical direction (z-axis), using a low frequency (100kHz) sinusoidal voltage (9V) produced by function generator (Agilent 33521A) with a high voltage amplifier (Tabor Electronics 9200).

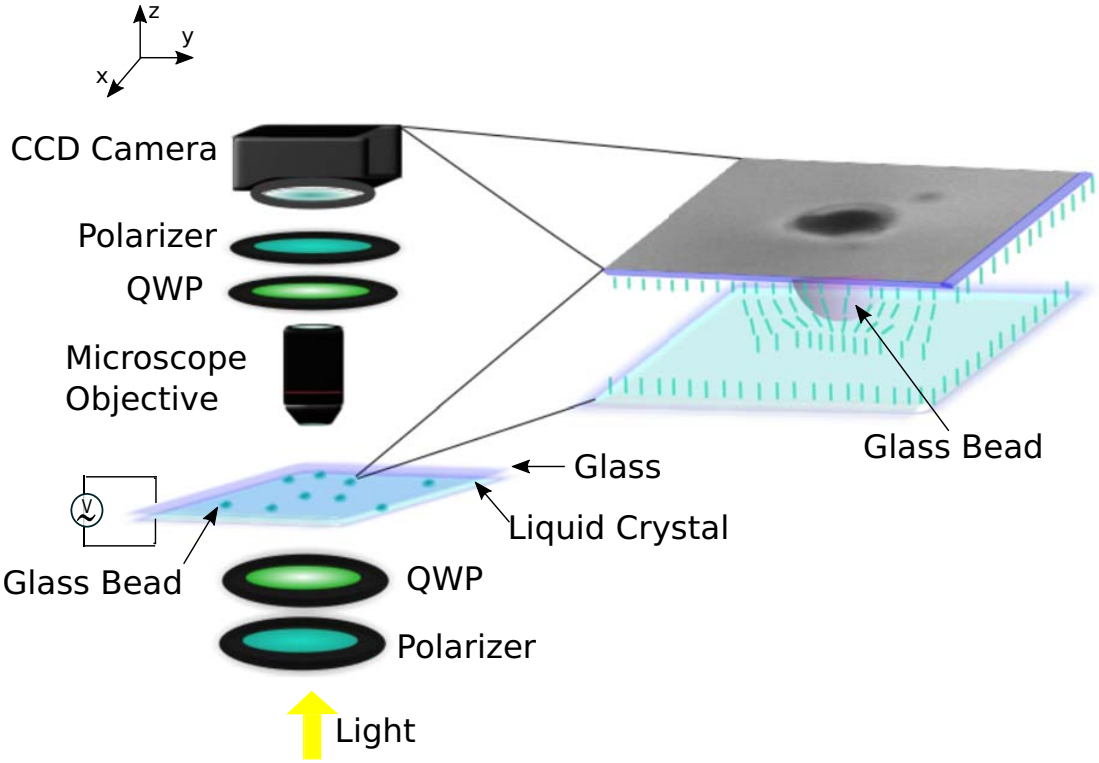

Figure 2. Sketch of the setup. The microscope, here represented by the objective, and accommodates a circular polarizer, bottom quarter-wave plate (QWP) and polarizer, and a circular analyzer, top polarizer and quarter-wave plate. The image of the cell is recorded via a CCD camera. The inset sketches the glass bead and a configuration of liquid crystal directors.

The imaging system used, see Figure 2, is a modified Motic 310 microscope equipped with a circular polarizer (bottom linear polarizer and quarter-wave plate) and a circular analyzer (top quarter-wave plate and polarizer). The light from the microscope condenser, that illuminate the cell mounted on the microscope stage, is filtered with a band-pass filter since the QWPs are designed to operate at $\lambda = 532$nm. Then, the texture of the sample is captured by a charge-coupled device (CCD camera). The images obtained by the CCD camera are recorded and then

analyzed with an image processing and analysis software Fiji (ImageJ)[12]. The position of the glass beads and the vortexes are extracted for further analysis.

3. Results

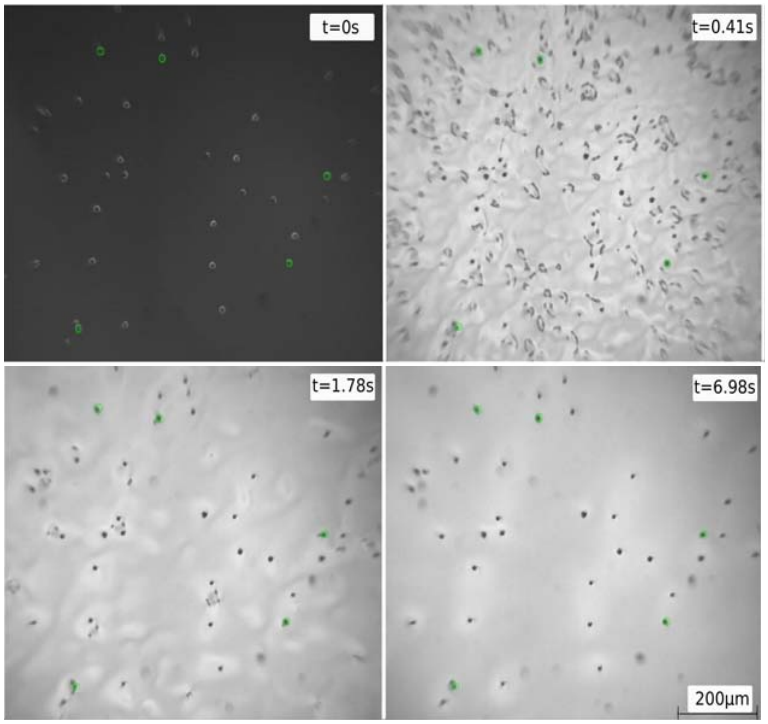

Figure 3. Vortexes dynamics in inhomogeneous medium. Sequence of temporal snapshots. Top left panel accounts for the liquid crystal layer without voltage. The gray and green-marked gray spheres correspond to glass beads. The green-marked spheres stand for attractive glass beads. Once the electric voltage is applied, a large number of vortexes are observed. Each vortex is identified as a black spot, which has a typical size of 5 μm, as illustrated in the top right panel. Subsequently, the vortexes of opposite charge are attracted to each other and annihilated, decreasing the density of vortexes (cf. bottom left panel). In this regime of dilute gas of vortexes, some of them are attracted by some glass beads. Finally, for a sufficiently long time all the vortexes disappear, see bottom right panel.

When a low frequency voltage with a sufficiently large amplitude greater than the Freédericksz voltage is applied to the nematic liquid crystal layer—which was previously described—the creation of vortexes is observed. Due to the presence of the glass beads in the sample, this process occurs in an inhomogeneous medium. The dynamics of vortexes is strongly affected by the glass beads [10]. We observe that there are attractive glass beads. Indeed, the attractive spheres pull the near vortexes. Figure 3 shows a typical observed vortex dynamics.

In the monitored region, there are 39 glass beads, only five of them are attractive. The density of glass non-attractive beads and attractive ones are 27 beads/mm^2 and 4 beads/mm^2, respectively. Hence, the proportion of attractive glass beads is 15%. Initially, a large number of vortexes are created, then the vortexes with opposite topological charges are attracted to each

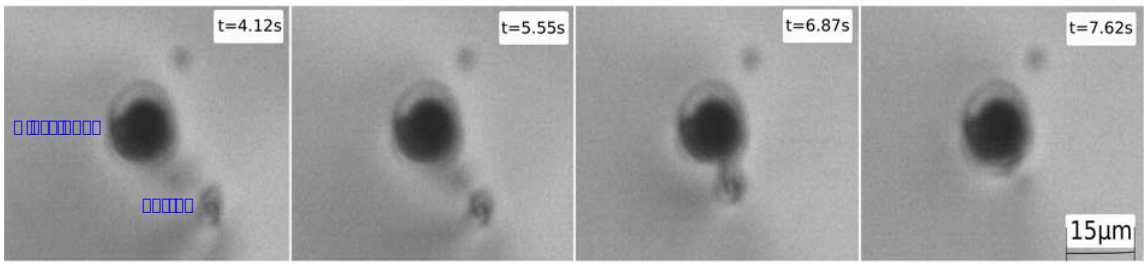

Figure 4. Vortex glass bead interaction. From the left to the right is presented a temporal sequence of snapshots. Initially, an attractive glass bead pulls a vortex. When a vortex collides with the attractive glass bead, it disappears (cf. right panel).

other and eventually annihilate and those with same charges are repel each other. As result of the vortex interaction, the density of vortex decreases with time. In this regime of dilute gas of vortexes, some of the defects are attracted by some glass beads. When a vortex collides with the attractive glass bead, it disappears. Figure 4 illustrates the vortex and glass bead interaction, showing a sequence of snapshots. To characterize this process we have considered a region around an attractive bead embedded in the nematic liquid crystal layer, region that is magnified 20 times. Notice that the vortex trajectory is not radial. In addition, the typical time of collision between vortexes is of the order 2.33 s. On the other hand, the typical time of collision between a vortex and glass bead is of the order of 13.0 s.

To illustrate the non attractive glass beads, we have identified a pair of glass beads, one attractive and one unattractive (see Fig. 5). In this figure is illustrated how a sphere attracts three vortexes. Note that also this attractive glass bead modifies the dynamics between vortexes. The non attractive glass bead presumably weakly repels the vortexes, however experimentally we have not been able to verify this property. The above assertion is based on the fact that vortexes motion close to this glass bead have never been observed in our case. Even, the vortexes that are observed close to this sphere move away. A detailed study of this repulsive phenomenon is in progress. In the next section, we will present a detailed study of the vortex attraction towards a glass bead.

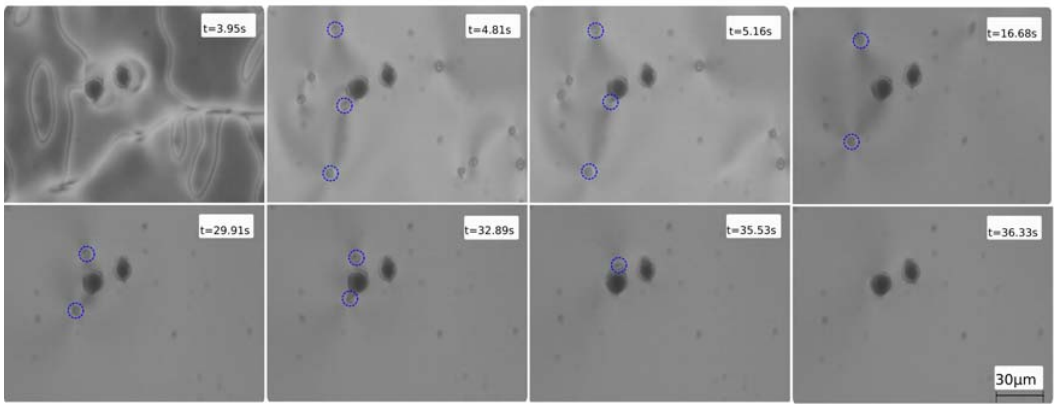

Figure 5. Attractive and non-attractive glass beads. From the left to the right is presented a temporal sequence of snapshots. The attractive sphere pulls three vortex. The vortexes that which are pulled by the attractive glass bead are highlighted with blue circular lines.

3.1. Experimental analysis of vortex and glass bead interaction

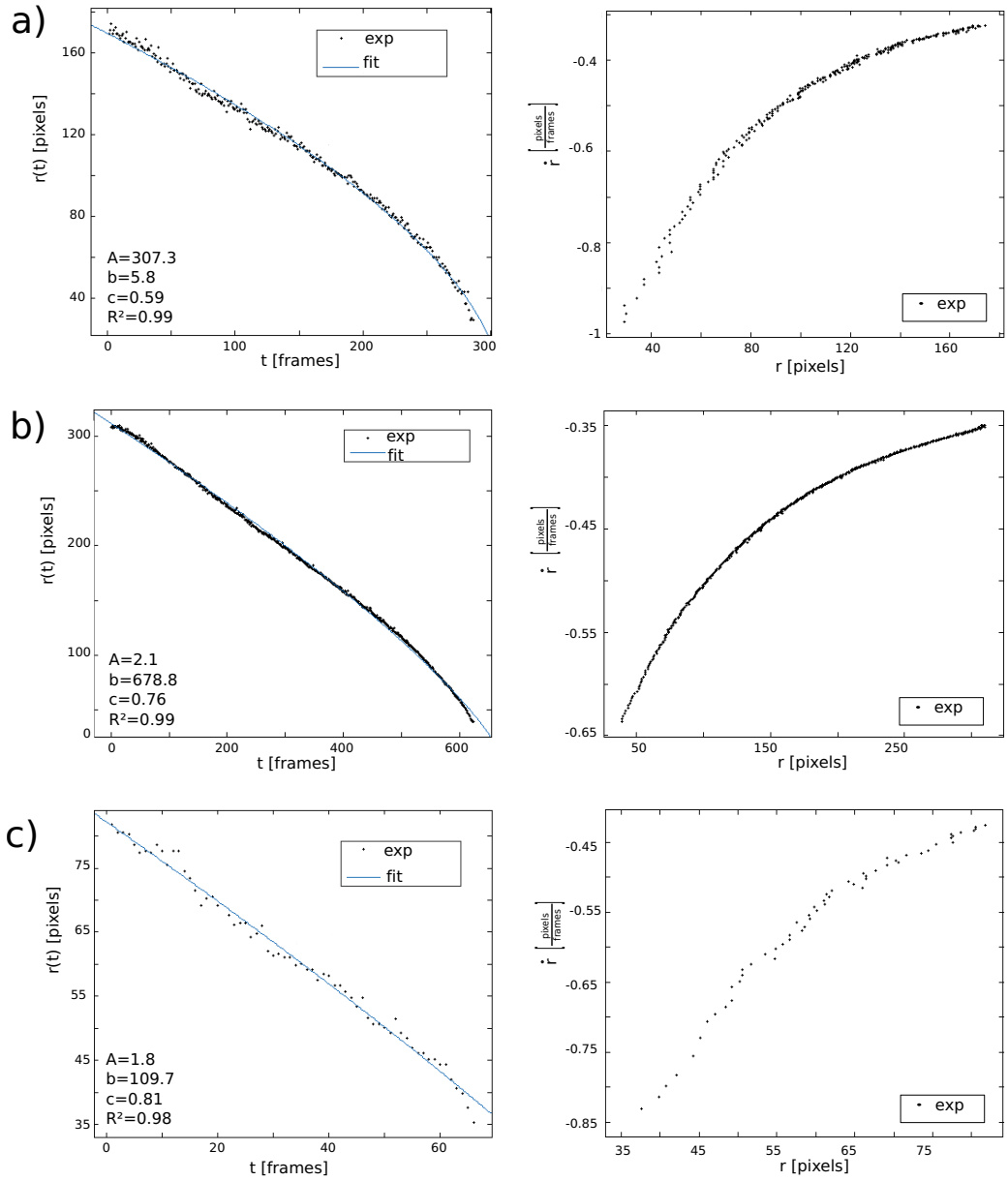

Figure 6. Interaction dynamics of vortex and glass bead. Points and continuous curves in the left panels, respectively, account for the experimental evolution of the distance between vortex and the glass bead as function of time for three experimental realizations and fitted curves using formula (2) with their respective adjustment R-square. Points and continuous curves in the right panels, respectively, stand for the experimental evolution and fit curves using formula (1) of the force as function of the vortex radial position (r) with respect to the attractive glass bead, where 1 pixel =0.254 μm and 1 frame= 0.06 s.

To characterize the interaction dynamics of vortex and glass bead, we have measured and monitored the distance between them. This distance was obtained by processing the glass beads and the vortexes positions, the latter determined from the analysis of a sequence of frames in the acquired video (fixed frame rate) using Fiji (ImageJ).

To carry on with this process, first an attractive spheres was identified via testing. Subsequently, an electric voltage is applied to the liquid crystal sample and the evolution of the vortexes attracted by the glass bead is studied. Later on, the external electrical voltage is turned off and the system is allowed to relax at equilibrium for a period of about 10 s. All this procedure is repeated several times to achieve an adequate statistical description. Left panels of figure 6 shows the experimental evolution of the distance between vortex and the glass bead as function of time for different experimental realizations.

The measurements are represented by the points cloud. Clearly from these measurements, one observes that the distance as a function of time has a well define evolution law. It is well-known that the vortex-pair interaction is characterized by an over-damped force that goes as the inverse of the distance between the vortexes [7]. Namely, the distance between opposite vortexes, $d(t)$, decreases as the square root of time, $d(t) = \kappa\sqrt{t_o - t}$ where t_o accounts for collision time and κ is an appropriated dimensional parameter. It is worthy to note that vortexes are characterized by the induced molecular distortion around vortex position [1]. Likewise, glass beads can generate molecular distortion in their own surrounding [11]. This molecular distortion generates interaction with the vortexes. Therefore, one would expect the attractive glass bead and the umbilical vortex interaction to be an over-damped force, $f(r)$, which is inversely proportional to a power of the distance, $r(t)$, between vortex and glass bead, that is,

$$\dot{r} = f(r) = -\frac{\gamma}{r^n}, \tag{1}$$

where γ is a dimension parameter and n is a real positive number. After straightforward calculations, one gets

$$r(t) = A(b - t)^c, \tag{2}$$

where b accounts for collision time, $A \equiv ((1 + n)\gamma)^{1/(1+n)}$ is a dimensional parameter, and $c \equiv 1/(1 + n)$.

In order to determine A, b and c from the experimental data, we will use formula (2) as a fit law. The continuous curves in left panels of figure 6 are the best fits of the experimental data for different realization. Note that there is a quite fair agreement between the experimental data and the fit law, formula (2). Note that the main source of fluctuations in the data is the detection algorithm of the vortexes.

Table 1 summarizes the fit parameters, using formula (2), of the vortex-glass bead interaction for 14 experimental realizations. We note that there is a trend between A and c. Indeed, when the c coefficient increases the A coefficient decreases. The b coefficient is related with the collision time of the vortex and the glass bead. The collision time is of the order of 13 seconds.

The above analyzes assume that the interaction is of a central nature. However, the trajectories of the vortexes to the glass bead are not radial.

Figure 7 shows the trajectories of different vortexes that move towards to glass bead, and the vortex glass bead interaction appears to be anisotropic. Experimentally, we observe that the vortexes collide with the glass bead in certain well define region which we termed as *south pole*. Probably, this anisotropic behavior is due to the fact that the deformation around the glass bead is not cylindrically symmetric, which could generate a deformation equivalent to a dipole. However, we have not detected vortexes that collide with the bead at its *north pole*. The detailed structure of the interaction is an open problem, and its understanding is in progress. Likewise, when the liquid crystal samples are not subjected to an external voltage and between to circular crossed polarizers, we observe that attractive and non-attractive glass beads exhibit

Table 1. Fit values, using formula (2), of the vortex-glass bead interaction for 14 experimental realizations.

cases	A	b	c	R^2
I	30.6	1027.0	0.26	0.98
II	22.2	29.2	0.29	0.99
III	16.5	74.1	0.35	0.99
IV	8.8	64.8	0.49	0.99
V	8.5	79.1	0.53	0.99
VI	7.4	127.8	0.54	0.99
VII	8.0	71.3	0.57	0.99
VIII	6.5	124.6	0.58	0.99
IX	5.8	307.3	0.59	0.99
X	5.0	108.7	0.63	0.99
XI	5.1	82.5	0.67	0.99
XII	2.1	678.8	0.76	0.99
XIII	1.8	109.7	0.81	0.99
XIV	0.4	369.6	0.91	0.99
Average	9.19	232.46	0.57	0.99

an asymmetrical and symmetric halo of light, respectively. The inset of Fig. 7 depicts the typical observed halo of light.

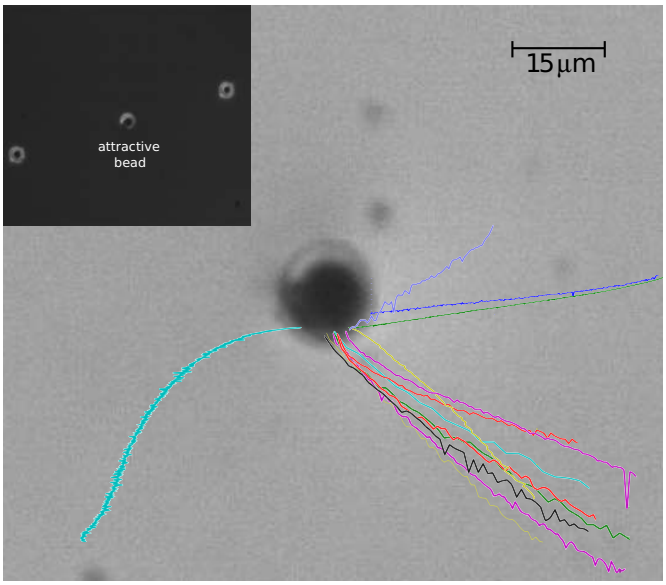

Figure 7. Anisotropic interaction between vortex and glass bead. Different colors account for different vortex trajectories. Inset accounts for the liquid crystal sample without external voltage and between to circular crossed polarizers. The attractive (glass bead in the middle) and non-attractive glass beads (glass beads outside) exhibit an asymmetrical and symmetric halo of light, respectively.

3.2. Vortex-glass bead force

Although the interaction is not isotropic, as a first approximation it will be considered isotropic. From the experimental data on the evolution of the distance between the vortex and the glass bead, one can deduce an evolution law using formula (2), see left panels of Fig. 6. Similarly, from the experimental data and fit curve one can reconstruct the interaction force between the vortex and the glass bead.

The points and the continuous curves in right panels of figure (6) show, respectively, the vortex speed ($\dot{r}$) as function of the distance (r) obtained from experimental data and theoretical fit, formula (1) for different experimental realization. From figure 6, one can infer that as the distance (r) increases, the interaction force is more abrupt. From this figure we can conclude that the force of interaction as function of the distance between the vortex and the glass bead is an inverse power law in good approximation.

To understand how the force changes as a function of time, from the fit expression of the temporal evolution of the distance between vortex and glass bead, formula (2), we can rebuild the interaction force as function of time,

$$f(t) = \dot{r} = -Ac\,(b-t)^{c-1}\,. \tag{3}$$

Rewriting this expression $f(t) = -C_1\,(b-t)^{(c-1)}$, where $C_1 = cA$. Considering the average value c from table 1, $\langle c\rangle = 0.57$, we obtain the average force of vortex-glass bead

$$\langle f(t)\rangle = -\frac{C_1}{(b-t)^{0.43}}. \tag{4}$$

Hence, the attractive glass bead spheres pull the vortexes so that the distance decays approximately as the inverse of the square root of the time to collision. On the other hand, the interaction force as a function of distance has the form given by formula (1), where average exponent is $\langle n\rangle = 0.75$. Therefore from these results, we conclude that when the distance between vortex pair and the distance between vortex and glass sphere are the same, the interaction between vortex and glass bead ($\approx 1/r^{3/4}$) is greater than the vortex pair interaction ($\approx 1/r$). However, we note that after the vortexes are created, the distance between vortex pair is less than distance between vortex and glass bead, hence, the main interaction is between vortex pair. Subsequently, when the remaining number of vortexes is reduced (diluted gas), they begin to interact with the attractive glass beads. This scenario is the one observed experimentally (cf. Fig. 3).

4. Conclusions and Remarks

Liquid crystal driven by external electric and magnetic fields exhibit an intricate network topological defects. These types of defects have attracted the attention of physicists, mathematicians, and engineers for their fundamental properties as macroscopic topological particles and for their potential applications in particular in communications, image processing and quantum computation [4, 5]. Here, we have reported an experimental characterization of vortex-glass bead interaction in nematic liquid crystal layer. The glass bead spheres can be classified in two type from the interaction point of view: attractive and non-attractive.

The attractive glass bead spheres pull the vortexes so that the distance decays as the square root of the time to collision. The glass bead sphere induces an anisotropic force on the vortex. This force can be well approximate by an inverse power law of the distance between vortex and glass bead with exponent 3/4. The vortexes are attracted to a polar region of the attractive glass bead. After the vortexes are created the main interaction is mediated by vortex pair interaction. Subsequently, when a reduced number of vortexes is left (diluted limit), they begin to interact with the attractive glass beads. This scenario is the one observed experimentally.

Still unknown the origin of these attractive force between vortex and glass bead. Certainly, the presence of glass bead generate deformation around itself. This deformation is responsible of vortex-glass bead interaction, and its characterization is in progress. Likewise, in the present study we have neglected the effect of distant vortexes (vortex pair interaction). In addition, mean field theory is not valid as consequence of long range interaction between vortexes. Hence, the presence of distant vortex can play a role. A systematic study of this issue is in progress. The role of non-attractive glass beads has not been performed, they are probably of repulsive type.

Acknowledgments
V.Z. thanks for fruitful comments and observations given by M.G. Clerc, R. Barboza, G. Gonzalez-Cortes, and M. Ferré.

5. References

[1] S. Chandrasekhar, 1977, *Liquid crystals of disc-like molecules* (Cambridge University press, Cambridge).
[2] P. G. de Gennes and J. Prost, 1974, *The Physics of Liquid Crystals* (Oxford University press, New York).
[3] P. Oswald, and P. Pieranski, 2005, *Nematic and cholesteric liquid crystals: concepts and physical properties illustrated by experiments* (CRC press, Boca Raton).
[4] L.M. Pismen, 1999, *Vortices in Nonlinear Fields: From Liquid Crystals to Superfluids, From Non-Equilibrium Patterns to Cosmic Strings* (Clarendon press, Oxford).
[5] F. Bethuel, H. Brezis, and F. Hélein, *Ginzburg-Landau Vortices* (Springer Science & Business Media, 2012).
[6] I. Dierking, *Textures of liquid crystals* (Wiley-VCH, Darmstadt, 2003).
[7] R. Barboza, U. Bortolozzo, G. Assanto, E. Vidal-Henriquez, M.G. Clerc, and S. Residori (2012), Vortex induction via anisotropy stabilized light-matter interaction, Phys. Rev. Lett. **109**, 143901.
[8] R. Barboza, T. Sauma, U. Bortolozzo, G. Assanto, M.G. Clerc, and S. Residori, (2013), *Characterization of the vortex-pair interaction law and nonlinear mobility effects*. New J. Phys. **15**, 013028.
[9] M.G. Clerc, E. Vidal-Henriquez, J.D. Davila, J.D., and M. Kowalczyk, *Symmetry breaking of nematic umbilical defects through an amplitude equation*, Phys. Rev. E, **90**, 012507 (2014).
[10] R. Barboza, U. Bortolozzo, M.G. Clerc, R. Residori, and V. Zambra, (2016), *Coarsening Dynamics of Umbilical Defects in Inhomogeneous Medium*, In Nonlinear Dynamics: Materials, Theory and Experiments (pp. 31-43). Springer International Publishing.
[11] M.A. Gharbi, M. Nobili, G. Prvot, P. Galatola, J.B. Fournier, and C. Blanc, (2011), *Behavior of colloidal particles at a nematic liquid crystal interface*, Soft Matter, **7**, 1467.
[12] J. Schindelin, I. Arganda-Carreras, E. Frise, et al., (2012), *Fiji: an open-source platform for biological-image analysis*, Nature methods, **9(7)**, 676-682.

Appendix C

Umbilical defect dynamics in an inhomogeneous nematic liquid crystal layer

Publication Details

- Title: Umbilical defect dynamics in an inhomogeneous nematic liquid crystal layer
- Author: Valeska Zambra, Marcel G. Clerc, Raouf Barboza, Umberto Bortolozzo, and Stefania Residori
- Published in: Physical Review E
- DOI: 10.1103/PhysRevE.101.062704

Umbilical defect dynamics in an inhomogeneous nematic liquid crystal layer

Valeska Zambra,[1,*] Marcel G. Clerc,[1,†] Raouf Barboza,[1,2,‡] Umberto Bortolozzo,[3,§] and Stefania Residori[4,3,‖]

[1]*Departamento de Física and Millennium Institute for Research in Optics, Facultad de Ciencias Físicas y Matemáticas, Universidad de Chile, Casilla 487–3, Santiago, Chile*

[2]*Dipartimento di Fisica, Università di Napoli Federico II, Complesso Universitario di Monte Sant'Angelo, Via Cintia, 80126 Napoli, Italy*

[3]*HOASYS, 1047 route des Dolines, 06560 Valbonne, France*

[4]*Institut de Physique de Nice, UMR7010, Université de Nice-Sophia Antipolis, CNRS, 1361 Route des Lucioles, 06560 Valbonne, France*

(Received 4 February 2020; accepted 22 May 2020; published 19 June 2020)

Electrically driven nematic liquid crystals layers are ideal contexts for studying the interactions of local topological defects, *umbilical defects*. In homogeneous samples the number of defects is expected to decrease inversely proportional to time as a result of defect-pair interaction law, so-called coarsening process. Experimentally, we characterize the coarsening dynamics in samples containing glass beads as spacers and show that the inclusion of such imperfections changes the exponent of the coarsening law. Moreover, we demonstrate that beads that are slightly deformed alter the surrounding molecular distribution and attract vortices of both topological charges, thus, presenting a mainly quadrupolar behavior. Theoretically, based on a model of vortices diluted in a dipolar medium, a $\frac{2}{3}$ exponent is inferred, which is consistent with the experimental observations.

DOI: 10.1103/PhysRevE.101.062704

I. INTRODUCTION

Irregularities in nature are one of the primary resources of the diversity of forms [1–6]. A paradigmatic example of these are fingerprints, which allow us to uniquely identify human beings. From a physical point of view, these correspond to the local or global loss of translation or rotation symmetry. Irregularities are commonly denominated defects. Depending on the geometrical shape of these irregularities they can be classified as localized or extended. Classical examples of localized and extended defects in condensed matter are dislocations and grain boundaries [7]. Defects are a consequence of the fact that systems out of equilibrium present the coexistence of spatially extended states [2–6]. Hence, irregularities connect different states. Among others, defects in rotationally invariant two-dimensional systems, i.e., vortices, attract a great deal of attention of the scientific community because of their universal character and intriguing topological properties [8]. These defects correspond to the local confluence of different orientational domains. Vortices have been observed in different physical contexts such as fluids, superfluids, superconductors, liquid crystals, fluidized anisotropic granular matter, magnetic media, optical dielectrics, and cosmology, to mention a few [8]. Mathematically, these solutions occur in complex fields and can be identified as pointlike singularities which locally break rotational symmetry. At a singular point, the amplitude of the order parameter is zero due to its single valuedness, and its phase changes continuously by an integer multiple of 2π around the singularity. The winding number, *topological charge*, is assigned by counting the number of phase jump around the phase singularity [8]. While the sign of the winding number is given by the sense of increment (positive) or decrement (negative) of phase jump [8]. As a convention, it is attributed to the positive (negative) value of the topological charge for the clockwise (anticlockwise) of the phase distribution. Indeed, vortices are topological defects since these solutions are created or destroyed by pairs with their respective opposite charge. Also, vortices can be induced by an external topological forcing [9–11].

Nematic liquid crystals are a soft matter material made of anisotropic rodlike shaped organic molecules [12–14], which results in strongly anisotropy media. In the nematic phase, the configuration of lowest energy is reached when all the rodlike molecules are on average aligned along one privileged direction. This privileged direction is usually imposed by the anchoring conditions of the recipient containing the liquid crystal [12–14]. Under the effect of sufficiently large external electric or magnetic fields, the molecules can be reoriented along or orthogonal to the direction of the applied field in order to minimize the free energy [15]. This reorientation generates the emergence of different domains and defects that separate them. In particular, nematic liquid crystal cells with negative anisotropic dielectric constant and homeotropic anchoring are a natural physical context where dissipative vortices and line defects can be observed and analyzed [12–14]. In this physical configuration, the dissipative vortices are usually called umbilical defects [16]. Due to the fact that these defects break the orientational order and by analogy with disclinations in crystals of condensed matter, Frank called these defects *disclination lines* [13,19]. These defects have accompanied liquid crystals since their discovery in 1889 by Lehmann [17] who called these intriguing localized structures as *kernels*. Likewise, they were observed in

*valesk.za@gmail.com
†marcel@dfi.uchile.cl
‡raouf.barboza@tut.fi
§umberto.bortolozzo@hoasys.fr
‖stefania.residori@hoasys.fr

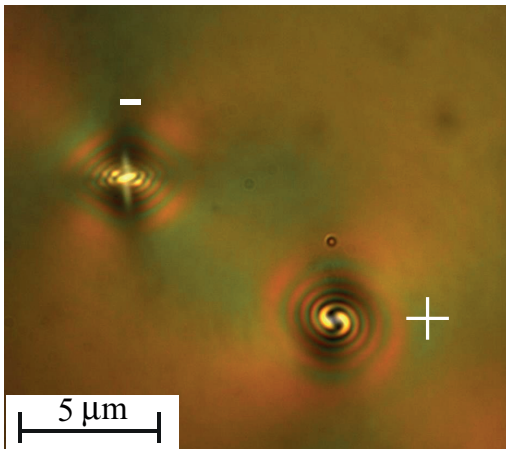

FIG. 1. Snapshot of umbilical defects of opposite charges observed in a nematic liquid crystal layer within circular crossed polarizers (CCP). Umbilical defect of positive (negative) charge has circular (square) shape.

a similar experimental setup by Friedel, who denominated these defects as *noyaux* [18]. Frank calculated the detailed structure of these defects based on the elasticity of nematic liquid crystals [19]. Despite the different designations given to the observed vortices in this physical framework, none of them were adopted by the liquid crystals community. There, the most widely used names are *nematic umbilical defects* and *disclination lines*. Henceforth, we will use the term umbilical defects, even though it is intended that these two names can be used indifferently.

The term umbilic defects was coined by Rapini [16] and refers to the structure of the defect which corresponds to a stringlike object in three dimensions. Umbilical defects in nematic liquid crystal layers have long been studied (see textbooks [12–14] and reference therein). Two types of stable defects with opposite charges are observed, which are characterized by being attracted to (repelled by) the opposite (identical) charge. Figure 1 shows the typical umbilical defects observed in the microscope using circular crossed polarizers. Note that such defects observed in liquid crystals are structurally similar to those found in magnetic systems, superfluids, superconductors, and Bose-Einstein condensates. However, umbilical defects are dissipative states, that is, they exhibit an entirely different dynamical evolution due to the strongly dissipative nature of liquid crystals.

Due to the complexity of the elastic theory of liquid crystals, the analytical study of the umbilical defects is inaccessible [12,13]. Weak nonlinear analysis, valid close to the orientational instability of the molecules, allows describing the dynamics of a nematic liquid crystal layer by the Ginzburg-Landau equation with real coefficients [10,11,20–23]. This amplitude equation has gathered a great interest by describing several physical systems such as fluids, superfluids, superconductors, liquid crystals, magnetic media, and optical cavities, to mention a few (see the textbook [8] and reference therein). Indeed, this amplitude equation describes the onset of a degenerate stationary instability with rotational invariance [4] or a stripe pattern instability in anisotropic systems [5,24]. Hence, the dynamics described by this model is common to a wide class of physical systems. The Ginzburg-Landau equation with real coefficients allows understanding the emergence of different orientational domains, two types of stable vortices with a positive and negative charge and their respective dynamics. In this approach, both local defects are indistinguishable in their amplitude magnitude. As a result of the phase invariance of this amplitude equation, they account for a continuous family of solutions, characterized by a phase parameter [8]. Besides, one can characterize analytically the vortex-pair interaction [8], which is in agreement with experimental evidence [22].

In a first approximation, the vortex-pair interaction is described by an overdamping system with force proportional to the inverse of their distance [12,25]. Experimental observations provide asymptotically agreement with this approach [26–29]. In general, the law of the number of defects as a function of time can be derived based on defect-pair interaction law and self-similarity statements [30,31]. The resulting self-similar behavior is well known as a *coarsening* process, in analogy with domain growth in metallic alloy phase separations [32] and in foam drainage [33]. Using the vortices' interaction law, one can show that the number of defects in homogeneous nematic samples decreases inversely proportional to time, which has been previously observed [26,29,34]. Likewise, using phase XY model, one obtains the same decay law for the vortices' number [29].

To study the coarsening dynamics in inhomogeneous nematic samples, we use cells in which the thickness of the liquid crystal layer is fixed by monodispersed glass microspheres spread randomly inside the sample. By characterizing the creation and interaction process of umbilical defects, we show that the presence of the beads alters the coarsening law. Indeed, even though most of the glass beads do not affect the vortices' dynamics, those that are more geometrically deformed attract vortices of both topological charges, presenting mainly a quadrupolar behavior, an interaction weaker than the usual interaction between dipolar vortices. This effect actively modifies the collective behavior of the vortex system and alters the scaling law [35]. Depending on the different disordered configurations of beads, the system exhibits different statistical temporal evolutions of the number of defects, exhibiting power laws with different exponents. Theoretically, based on a model of vortices diluted in a dipolar medium and self-similarity, a coarsening law with exponent $\frac{2}{3}$ is inferred. This critical exponent shows a good agreement with the experimental observations.

II. EXPERIMENTAL SETUP

To study the dynamics of umbilical defects, we consider two different types of liquid crystal cells with approximately the same thickness. The first cell, *homogeneous sample*, is made of two indium tin oxide (ITO, transparent conductor) coated glass slabs. The glass slabs are treated on the ITO side to promote orthogonal alignment of the liquid crystal molecules; this alignment is termed as homeotropic anchoring [12–14]. The glass slabs are held together with a thin sheet of polymer spacers such that, the treated faces form a gap in which the liquid crystal is, then, infiltrated.

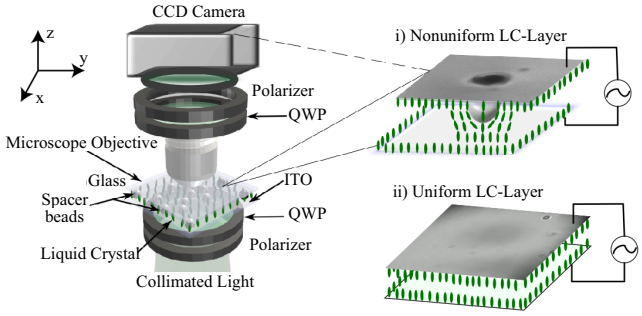

FIG. 2. Schematic representation of the experimental setup of a nematic liquid crystal layer with negative dielectric constant and homeotropic anchoring under the influence of a vertical voltage. The essential parts of the setup are emphasized. Crossed polarizers, either linear or circular, are used in order to analyze the liquid crystal texture. Two types of liquid crystal cells have been studied: (i) homogeneous and (ii) inhomogeneous (with glass beads) sample.

The spacers fix the thickness of the gap, which is about 15 μm thin. The second cell, *inhomogeneous sample*, from Instec Inc. (SB100A150uT180 liquid crystal cell), also has a homeotropic alignment. The spacing gap is achieved by sputtering spacer beads made of microsphere clear and transparent ceramics or glass onto the cell substrate before assembly [36]. The diameter of the microspheres fixes the cell gap, which is about 15 μm for the chosen cell. Both cells were filled by capillarity with MLC-6608 nematic liquid crystal (from Merck), characterized by a negative dielectric anisotropy. Figure 2 depicts the experimental setup. To achieve maximum contrast, resolution, a collimated white light (Köhler type illumination) from a microscope condenser is sent onto the liquid crystal cell, the latter mounted on a translation stage. The texture of the liquid crystal is imaged on a CCD camera through a microscope objective and relay lenses.

From here on, we will denote by $\hat{z}$ the normal to the glass plates. Due to inherent elastic forces between the molecules, in a certain temperature range, the absence of external stimulus, to minimize the elastic free energy, the alignment in the bulk of the liquid crystal layer will be uniform, thus parallel to the $\hat{z}$ direction in order to accommodate that of the boundaries. Both cells are biased with a low-frequency sinusoidal voltage ($\approx$100 Hz) and are operated at room temperature where the liquid crystal is in the nematic phase. The resulting electric torque will tend to rotate the molecules away from the z axis. Over a critical threshold voltage, called Fréedericksz transition voltage [12–15], the molecules tilt away from their vertical position. Due to the 2π azimuthal degeneracy in possible directions of orientation, different domains, and umbilical defects will be generated in the nematic liquid crystal layer where the orientation can not be topologically smoothed out [12–14,16–19].

The cells contain liquid crystals that are intrinsically birefringent in the nematic phase. Two crossed polarizers, the first to polarize the illumination source and the second to analyze the polarization of the light exiting the cell, are used to recover the averaged two-dimensional texture of the liquid crystal layer, where the average is along $\hat{z}$. Indeed, with a good approximation, the cell can be considered as a two-dimensional (2D) uniaxial birefringent material with varying optical axis aligned in the xy plane at an angle $\theta(x, y)$ with the x axis and providing a phase retardation $\delta(x, y) = 2\pi L(\tilde{n}_e - n_o)/\lambda$. Here, L represents the thickness of the liquid crystal layer, λ the operating wavelength of the illumination source, and $\{n_o, \tilde{n}_e\}$ the ordinary and, respectively, extraordinary refractive index averaged over the longitudinal coordinate. The optical axis can be viewed as the averaged azimuthal direction of the molecules in the xy plane or, equivalently, their projection onto the xy plane. The averaged extraordinary index $\tilde{n}_e$ is related to n_0, n_e (the extraordinary refractive index of fields polarized along the optical axis) and the tilt ψ of the molecules with respect to the z axis by [12,14]

$$\tilde{n}_e = \int_0^L \frac{n_e n_o}{\sqrt{n_e^2 \cos^2\psi + n_o^2 \sin^2\psi}} dz. \tag{1}$$

To probe the evolution of the texture of the liquid crystalline layer, hence, the dynamics of the defects, we rely on polarizing optical microscopy techniques based on crossed linear polarizers (CLP). By using Jones matrix formalism [37], the intensity is given by [37]

$$I_{\mathrm{CLP}}(x, y) = I_0 \sin^2 \frac{\delta(x, y)}{2} \sin^2 2\theta(x, y), \tag{2}$$

where I_0 is the maximum input intensity. Likewise, the crossed circular polarizer (CCP) configuration is achieved when two quarter wave plates are inserted in the previous configuration, with the first wave plate at $\pm 45^\circ$ with respect to the axis of the input polarizer, and the fast axis of the second wave plate orthogonal to the first one. In this case, the intensity after the cell depends as follow on the phase retardation [37]

$$I_{\mathrm{CCP}}(x, y) = I_0 \sin^2 \frac{\delta(x, y)}{2}. \tag{3}$$

In the experiment both imaging configurations, either CLP or CCP, are used with the polarizing microscope, depending on the defect features that we want to emphasize, either position or charge.

In the Ginzburg-Landau theoretical framework, positive and negative defects are indistinguishable, that is, they are supposed to look the same for CLP and CCP. However, due to the anisotropy of the elastic constants of liquid crystals, they can be distinguished under appropriate conditions. Figure 1 shows two umbilics, one with positive and the other with negative charge. The micrograph is taken with crossed circular polarizers. Note that the defect with positive charge has a circular shape, while the negatively charged umbilic has a square shape [38]. These geometrical features allow us to distinguish the sign of the topological charges. Note that these geometric features persist under linear crossed polarizers [38].

III. RESULTS AND DISCUSSIONS

First, in order to figure out the coarsening dynamics of the vortices in a homogeneous cell, we proceed as follows: we start with establishing the vortex-pair interaction law and, then, by using its self-similarity properties, we deduce the coarsening law.

A. Vortex-pair interaction law

Based on the Ginzburg-Landau equation with real coefficients that describes liquid crystal dissipative dynamics, the fine analysis of the vortex interaction law is a daunting task due to the logarithmic divergence of the energy associated with each vortex and the vortex-pair interaction with the size of the system [8,12]. In the case of finite size systems, the vortex-pair interaction law can be approximated for long distances by [8]

$$M\dot{\mathbf{r}} = \frac{q}{||\mathbf{r}||}\hat{r}, \tag{4}$$

where $\mathbf{r}(\mathbf{t})$ is the vector that joins the positions between vortices, $||\mathbf{r}||$ is the magnitude of the vector $\mathbf{r}$, $\hat{r} \equiv \mathbf{r}/||\mathbf{r}||$ is a unitary vector, q is the product of the topological charges of interacting vortices ($q = \pm 1$), then it is positive (negative) when both vortices have the same (different) charge, and M stands for the vortex mobility which depends on the size of the system, the properties of the liquid crystal, and the applied voltage. When one considers the effect of the phase of one vortex on the other, mobility depends logarithmically in $\dot{r}$ [5]. However, this correction is weak [22] and can be neglected when fine interaction between defects is not of concern and only collective effects are of interest. Thus, the constant mobility approximation is appropriate in the interpretation of the experimental results [39]. Hence, the interaction between vortices is equivalent to overdamped particles with a force inversely proportional to their distance. Note that when the vortex distance is small, of the order of the vortex core, the previous model for dynamics is no longer valid. In this case, vortices of opposite charge merge and disappear together.

In brief, the dynamics of interaction between vortices tend to homogenize the deformations of molecular orientation in order to minimize the free energy of the system. As we have mentioned, experimental characterization of the vortex-pair interaction provides a fair agreement with the previous results [22,26,28,29].

B. Theoretical derivation of the coarsening law for a diluted gas of vortices

In the context of dilute gases of n vortices in a homogeneous medium, the interaction between defects is governed by

$$M\dot{\mathbf{r}}_i = \sum_{j\neq i}^{n} \frac{q_{ij}}{r_{ij}}\hat{r}_{ij}, \qquad i = \{1, 2, \ldots, n\} \tag{5}$$

where $r_{ij} \equiv ||\mathbf{r}_i - \mathbf{r}_j||$ is the distance between the ith and jth vortex, $\hat{r}_{ij}$ in the unitary vector directed from jth to ith vortex, and q_{ij} is the, respective, product of the topological charges of vortices. Hence, the dynamics of a gas of n vortices corresponds to an overdamped n-body problem. Note that the above set of equations is invariant under the self-similarity transformation

$$\begin{aligned} \mathbf{r}_i &\to \lambda \mathbf{r}_i, \\ t &\to \lambda^2 t. \end{aligned} \tag{6}$$

If one dilates or expands time and space, using the above scaling, then, the set of Eqs. (5) are invariant. We can introduce $N(t)$, the number of vortices at time t, which can be estimated as

$$N(t) = \frac{A}{\langle r\rangle^2}, \tag{7}$$

where A is the area of the sample under study, and $\langle r\rangle$ is the average distance between vortices. Because the set of Eqs. (5) governs the vortices dynamics, the average distance $\langle r\rangle$ and $N(t)$ are determined by the vortices' evolution. Then, $\langle r\rangle$ and $N(t)$ should also be self-similar with transformation (6). Hence, $N(\lambda^2 t) = A/\lambda^2\langle r\rangle^2$. From the previous equality, one infers that the only possibility is that the number of vortices scales as

$$N(t) = \frac{\beta}{t}, \tag{8}$$

with β a dimensional constant. Indeed, the number of defects decreases inversely proportional to time, so-called *coarsening law*. Experimentally, this law was, indeed, observed and validated in nematic liquid crystal samples [29,34].

C. Vortex creation and annihilation in a homogeneous liquid crystal cell: Experimental observations

To investigate the creation and annihilation process of vortices, we have conducted several experimental analyses on the vortex gas dynamics. We apply a large enough voltage to the liquid crystal layer in-between crossed polarizers, which spontaneously generates hundreds of umbilical defects in random positions as a result of thermal fluctuations and inherent inhomogeneities in the system. Initially, the emergence of vortices is preceded by the appearance of domain walls [cf. Fig. 3(b)], which are created by thermal fluctuations. These domain walls are unstable, generating the emergence of topological defects of charges $\pm\frac{1}{2}$, which move along the domain walls. These topological defects are characterized by the joint of two black brushes [39]. Figure 3(c) illustrates the different observed local and global defects. These defects with half topological charge are characterized by the joint of two arms and a domain wall. Collisions of these defects with the same topological charge generate umbilical defects and with different charges cancel each other out. After this rapid transient, a dilute vortex gas is established in the system [cf. Fig. 3(d)]. Thanks to the crossed linear polarizers, the position of the umbilical defects is recognized by the interception of four black curves [12]. Subsequently, the defects exhibit a dynamic of attraction and repulsion following the interaction law (5). Figure 3 shows a temporal sequence of snapshots, which emphasize the natural evolution of the defect gas. From the temporal sequences and through an appropriate recognition software (open source Java image processing program Fiji), we can determine the number of vortices and their respective positions. Thus, we acquire the evolution of the number of vortices $N(t)$ as a function of time. Figure 3(f) summarizes the temporal evolution of $N(t)$ starting from the switch-on of the driving voltage V_0. From this temporal evolution, one can separate the process in two stages: one associated with the creation of vortices, *growth stage*, and, later, a second regime characterized by the process of decay of the number of vortices, *coarsening stage*.

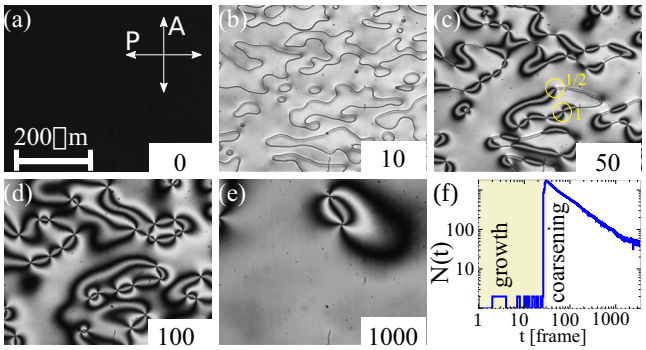

FIG. 3. Creation and annihilation dynamics of umbilical defects in a homogeneous nematic liquid crystal layer under two crossed linear polarizers. The temporal sequence of snapshots from left to right and top to bottom (a)–(e) corresponds to driving the cell from zero voltage to a voltage V_0 beyond the Fréedericksz transition threshold. The bottom numbers in each panel account for the respective frame. The temporal increment of each frame corresponds to 400 μs. The interception of four black brushes gives the position of umbilical defects with topological charge ± 1. (a) Liquid crystal cell without applied voltage, showing the orientation, respectively, of the polarizer (P) and analyzer (A). (b) Emergence of orientational domains after 800 μs the voltage is switched to $V_0 = 15\ V_{\rm rms}$. (c) Creation of vortices through reorganization of domains; circumferences and respective numbers account for the different topological charge of the defects. The interception of two black brushes gives the position of the defects with topological charge $\pm\frac{1}{2}$. (d) Diluted gas of vortices. (e) Vortex pair and (f) temporal evolution of the number of vortices $N(t)$.

D. Experimental determination of the coarsenin lawg in homogeneous cells

Based on the Ginzburg-Landau model, one expects the number of defects to decay with a power law. Figure 4 depicts the typical evolution of the number of umbilical defects as a function of time for a nematic liquid crystal layer driven to $V_0 = 70$ V with a frequency of 100 Hz. To compute and monitor the number of vortices in given time we have used an image processing package. From this plot, one infers that the

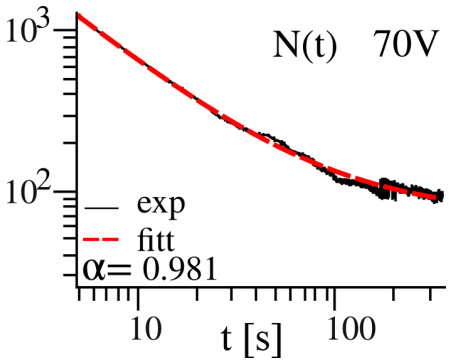

FIG. 4. Coarsening dynamics in a homogeneous cell. Number of umbilical defects as a function of time. The solid black and dashed curves are, respectively, the experimental evolution of $N(t)$ and the fitting curve $N_f(t) = \beta t^{-\alpha} + N_\infty$ with $\alpha = 0.981 \pm 0.001$, $\beta = 5.7 \times 10^3 \pm 2 \times 10^2$, and $N_\infty = 70 \pm 2$.

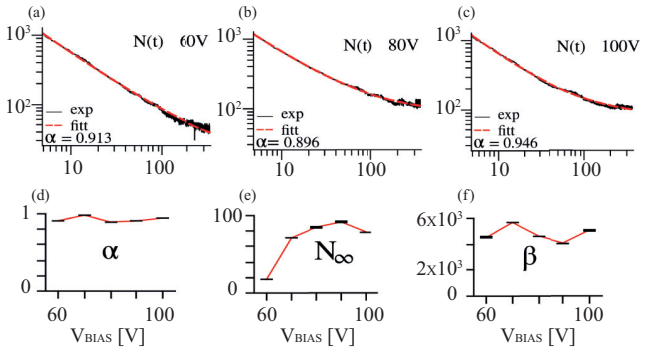

FIG. 5. Number of umbilical defects as a function of time. Coarsening process of umbilical defects in a homogeneous cell with different driven voltages (a) $V_0 = 60$ V, (b) $V_0 = 80$ V, (d) $V_0 = 100$ V, using the same frequency 100 Hz. The black and red curves account for the experimental data and fitting curve formula (9), respectively. Critical fitting exponent α (d), asymptotic number of vortices N_∞ (d), and β (e) as function of applied voltage.

number of vortices decays as a function of time with a power law. To determine the exponent of this coarsening process, we have considered the following fitting function:

$$N_f(t) = \beta t^{-\alpha} + N_\infty, \tag{9}$$

where $\{\beta, \alpha, N_\infty\}$ are fitting parameters, which account for the features of the liquid crystal and the cell under study. N_∞ stands for the imperfections of the system, which causes the vortices to become trapped in given positions, and the inaccuracy of the recognition method. Experimentally, we found that in the homogeneous samples under study the exponent $\alpha = 0.981$ provides a quite good agreement with the simplified description (5). Hence, this type of particle-type approach to the vortex dynamics in a homogeneous liquid crystal layer, ignoring the process of collision and nonlinear effect of mobility, gives a fair description of the average evolution of the vortices.

To study carefully the coarsening process, we have conducted a series of experiments with different voltages and the same frequency (100 Hz). Similar behaviors for the evolution of the vortex number are observed. Figure 5 summarizes the coarsening process for different voltages. From this analysis, we conclude that for different voltages the system exhibits a coarsening behavior. In particular, the critical exponent is close to $\alpha \sim 1$, which is consistent with the theory of the Ginzburg-Landau amplitude equation with real coefficients. Hence, this simplified theory of liquid crystal dynamics [21,23] appropriately accounts for the process of coarsening in a homogeneous nematic liquid crystal sample. In the next section, we will analyze the effect of inhomogeneities in the coarsening dynamics by using the inclusion of glass beads in the sample.

E. Experimental determination of the coarsening law in inhomogeneous liquid crystal cells

To investigate the interaction of the umbilics in the presence of randomly distributed inclusions in disordered liquid crystal media, we have conducted several experimental

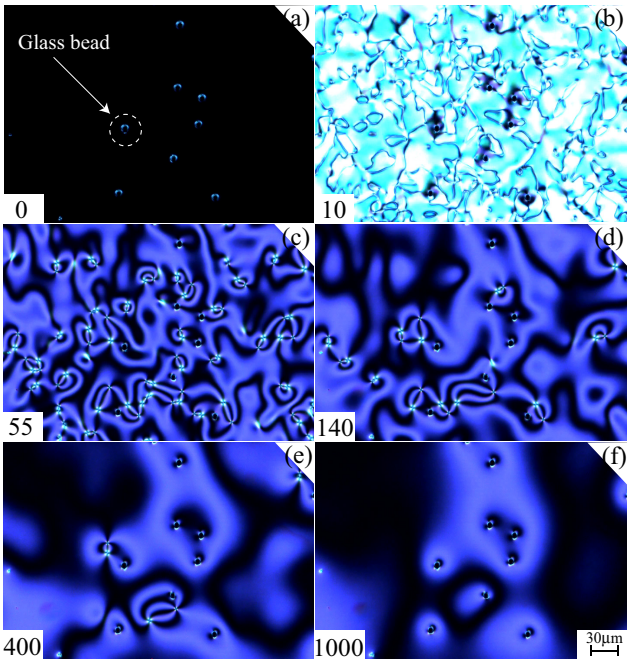

FIG. 6. Umbilical defect annihilation dynamics in an inhomogeneous liquid crystal cell with glass beads and in-between two linear crossed polarizers. Temporal sequence of snapshots from left to right and top to bottom depicts the vortex evolution starting from the switch-on of the driving voltage. The temporal increment of each frame corresponds to 0.33 s. The position of the umbilical defects is given by the interception of four black brushes. The white dashed circumference accounts for the position of a glass bead.

analyses of the vortex gas dynamics in a liquid crystal sample with glass beads. The inhomogeneous cell is observed in-between two crossed polarizers and by applying a large enough, beyond the Fréedericksz threshold, voltage. The glass beads are microspheres with a monodisperse distribution and a size of 15 μm. Figure 6(a) shows the liquid crystal cell without having an applied voltage. Because the anchoring is of the homeotropic type, under crossed polarizers the sample should appear as completely dark. However, the presence of glass beads distorts the configuration of the molecules in their surroundings. Hence, glass beads are detected by this molecular deformation reorientation, which changes the light polarization locally around each glass bead [see Fig. 6(a)]. As we mentioned earlier, the beads are randomly distributed. When a voltage is applied, initially, the emergence of domains is observed [see Fig. 6(b)], but now the process is affected by the presence of glass beads [35]. Later, the system is accompanied by the emergence of a gas of umbilical defects, as it is depicted in Fig. 6(c). Subsequently, the defect interaction dominates the dynamics, which is characterized by the constant decrease in the number of defects. Figure 6 shows a temporal sequence of snapshots depicting the vortex interaction in the cell. The natural question that emerges is, therefore, whether the coarsening dynamics is persistent under the inclusion of inhomogeneities in random positions.

To answer this question, we analyze the images with the particle tracking process, which allows us to determine the number of vortices and their respective positions. Figures 7(c) and 7(f) show the temporal evolution of the number of umbilical defects as a function of time for different zones of the liquid crystal sample. Each zone has an area of 1.43 mm^2 (cf. Fig. 7). In both graphs, we observe that the system exhibits a coarsening process with a power law, however, with different exponents. These power laws are obtained by realizing several experimental realizations (10 repetitions were performed for each parameter to obtain the characteristic exponents). Hence, the observed coarsening dynamics can be considered as a persistent phenomenon [35]. Nevertheless, depending on the distribution of the glass beads, we observe different power laws (cf. Fig. 7). Notice that the exponent deviates from the exponent determined by the law derived from the theory of the Ginzburg-Landau model for a homogeneous medium. Therefore, we can conclude that the presence, density, and distribution of glass beads affect the coarsening dynamics. The main effect, as we will see later, is produced by a small amount of deformed beads that interact and attract vortices.

TABLE I. Results of the measured bead density, computed fitting exponents, and entropy over an area of approximately 1.394 mm^2 on different observation zones.

Zone	**Density** (mm^2)	α	β	N_∞	**Entropy**
I	13.630	0.60	604.2	12.85	0.0210
II	17.217	0.88	1782.0	20.33	0.0136
III	20.803	0.25	246.4	22.44	0.00767
IV	21.521	0.71	1285.0	17.87	0.0091
V	23.673	0.70	1404.0	25.74	0.00772
VI	27.977	0.82	162.7	18.09	0.0057

To characterize the clustering and distribution of the glass beads, we have computed the Voronoi tessellation [40] of the glass beads in different observed zones [cf. Figs. 7(a) and 7(d)]. The respective histogram of the bead mutual distance is also computed on each observation zone [cf. Figs. 7(b) and 7(e)]. From these diagrams, we can measure the density of the beads and we obtain for zones I and III, respectively, 13.630 and 20.803 beads per mm^2. However, the number of attractive beads in each zone was not characterized. Zone III is more ordered than zone I since its histogram of the mutual distance is closer to a Rayleigh distribution around a length [cf. Fig. 7(b)] while the other is closer to a flat distribution without a feature length [see Fig. 7(e)]. Analogously, from this distribution we can compute the Shannon or information entropy S_e and obtain for each zone, respectively, $S_e(\mathrm{III}) = 0.00767$ and $S_e(\mathrm{I}) = 0.021$. Therefore, the evolution of the number of defects as a function of time changes depending on the different configurations of the glass beads.

To measure the exponents of the coarsening laws, we have considered the following fitting curve $N(t) = \beta t^{-\alpha} + N_\infty$. Table I summarizes our results for different observation zones of the liquid crystal layer under study. Different coarsening laws are obtained over different zones of the sample. However, from this table, we are not able to establish a correlation between the density of vortices, Shannon entropy, and spatial distributions with their coarsening exponents found experimentally. This is because of not only the spatial distribution of

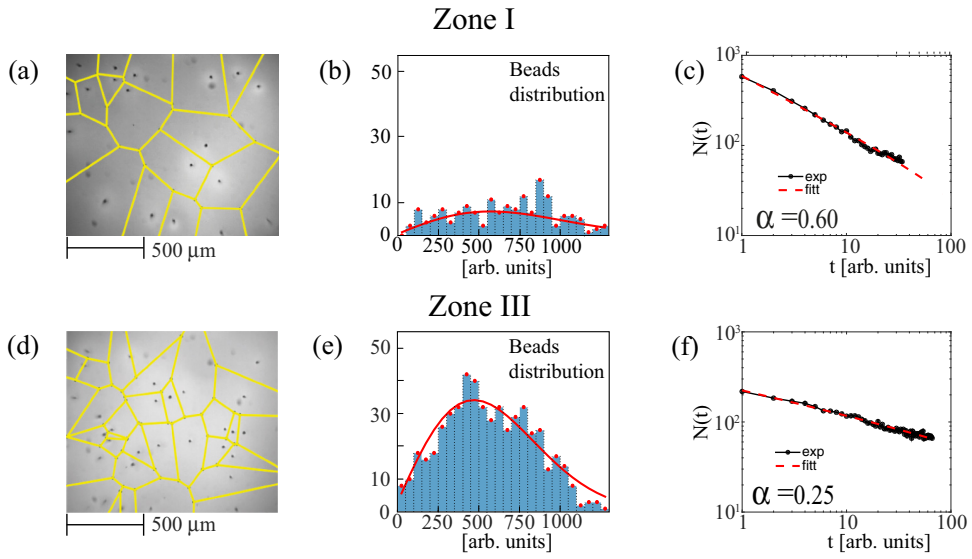

FIG. 7. Coarsening process of umbilical defects in an inhomogeneous sample analyzed over different observation zones, I and III. (a), (d) Voronoi diagram of glass beads in the observed zone, I and III, respectively. (b), (e) Histogram of the mutual distance of the glass beads. The solid curve is a fitting curve using a Rayleigh distribution. (c), (f) Corresponding scaling curves of the number of defects vs normalized time. Black points stand for the experimental data, dashed lines correspond to fitting curves of the form $N(t) = \beta/t^{\alpha} + N_{\infty}$ with $\alpha = 0.60$ and 0.25, respectively.

the glass beads matters but also how many of the glass beads are attractive or not. The effects due to the shape of the glass beads, and consequent vortex attraction, will be highlighted in the next section.

F. Defect dynamics in presence of a glass bead

The presence of the spherical spacers causes local deformation of the nematic director. Depending on their structure, the spacers can behave as localized potentials on the generated defects. Figure 8(a) shows a temporal sequence of snapshots of the vortex dynamics in the presence of a glass bead. Here, it is depicted the evolution of the umbilical defects under the influence of the bead. Figure 8(b) depicts the trajectories of the vortices. The dashed points (red) emphasize the positions of the vortices in different moments. In the temporal sequence, it is observed the temporal evolution of a pair of vortices with a positive and negative charge [cf. Fig. 8(b)]. Unexpectedly, both defects are attracted by the glass bead. From the trajectories, it appears clear that the vortex interaction is stronger than the vortex-bead interaction. Indeed, the vortices move close to the straight line that joins both vortices (see the dashed line in Fig. 8). However, close to the glass bead the trajectories are deflected and reoriented toward the center of the spacer. Finally, both vortices collide with the spacer and disappear. Hence, the observations show that the presence of inhomogeneities strongly affects the vortex dynamics and interactions.

To figure out the interaction between the vortices and the glass bead, we have repeated the experiment many times (∼50 experimental realizations) and monitored the collision of vortices, both with positive and negative charges, with the glass bead. This analysis is achieved by using circular crossed polarizers, which allows us distinguishing both topological charges with more precision. Figure 9 summarizes the different collision points between the vortices and the bead. The red (blue) points account for the collision points of positive

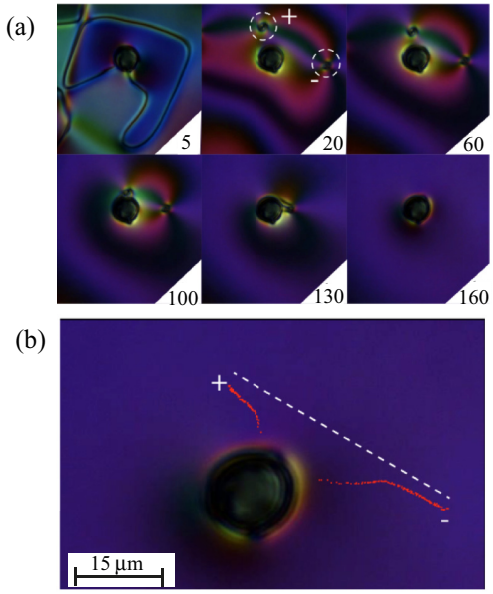

FIG. 8. Interaction between a glass bead and umbilical defects observed under linear crossed polarizers. (a) Sequences of temporal snapshots. The bottom numbers in each panel account for the respective frame. The temporal increment of each frame corresponds to 0.07 s. Umbilical defects of a positive (circular shape) and negative (square shape) charge under circular crossed polarizers are recognized and monitored. The dashed circles account for the umbilical defects. (b) Trajectory of the vortices: the dashed points (red) indicate the trajectory of defects, the dashed straight line accounts for the initial distance between defects.

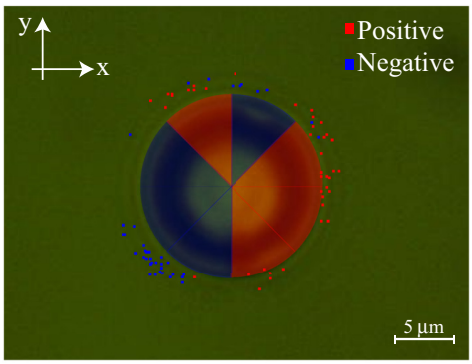

FIG. 9. Quadrupolar structure generated by a glass bead in the liquid crystal medium. Experimental characterization of the collision points of the umbilical defects for different experimental realizations. In most of the realizations only one defect collides with the bead. The dark (blue) and light (red) points account for the collision points of positive, respectively, negative vortices. The color areas highlight the different collision regions of the bead.

(negative) vortices. From this figure, it is possible to infer that the glass bead has a quadrupolar structure. Namely, the vortices of a given charge prefer to collide in certain parts of the bead. Note that the observed poles are not symmetric, which is a manifestation that dipolar terms are also relevant in the interactions. Experimentally, the vortex-bead interaction is weaker than the interaction between the umbilical defects. It is well known that glass beads without surface treatment generate homeotropic anchoring at their boundaries, that is, the liquid crystal molecules tend to be oriented normal to the surface of the glass bead [36,41]. In addition, due to the fact that the glass bead is in contact with the glass plates of the sample, one expects a Saturn-ring-like defect loop to appear around each glass inclusion [36,41]. Figure 10 shows a schematic representation of the director field lines induced by a perfect spherical glass bead and a slightly deformed bead. When the glass bead is perfectly spherical, it generates a defect in the center, which is canceled with the equivalent charge caused by the Saturn ring. In Fig. 10, the induced charge is represented by a central point (blue) and the Saturn ring by a closed curve (green). Therefore, perfectly spherical glass beads cause the net charge to cancel out, that is, the

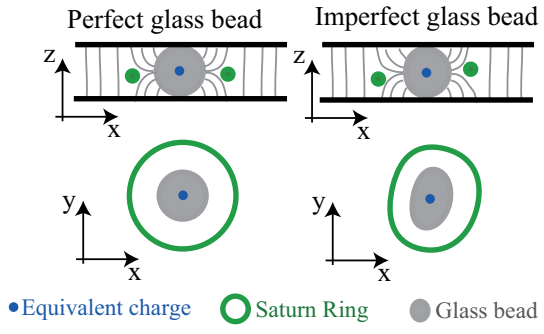

FIG. 10. Schematic representation of the director field lines induced by a perfect spherical bead (left panel) and a slightly deformed bead (right panel). Upper and lower panels show a side and top view of the correspondingly induced defects.

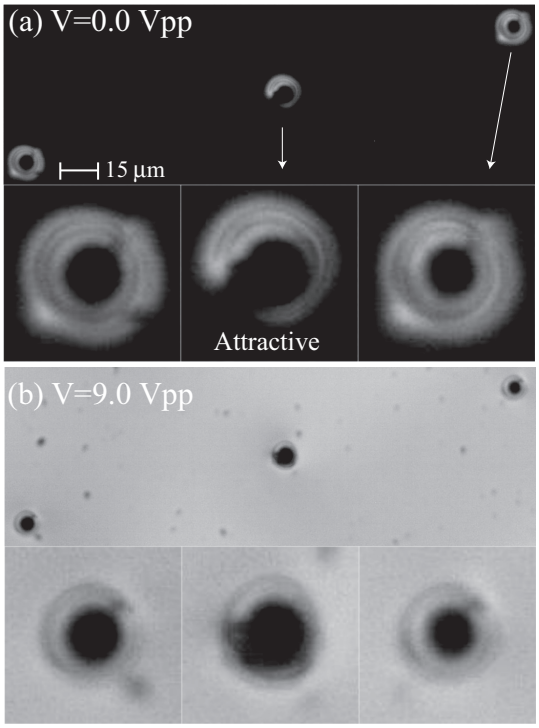

FIG. 11. Optical micrograph of active and passive glass beads. Snapshots of a liquid crystal sample within linear crossed polarizers without (top panel) and with (bottom panel) voltage. The lateral beads are passive, while the central bead is active.

equivalent charge of the Saturn ring coincides with the charge induced in the center. These glass beads are characterized by not attracting vortices so that we name them as *passive beads*. In contrast, deformed glass beads generate equivalent multipolar charges (dipoles, quadrupole, and so forth), which are neutral but affect the dynamics of their surroundings. In particular, these glass beads with multipolar charges are characterized by attracting and annihilating vortices and we name them *active beads*. Experimentally, these glass beads with multipolar charges can be detected since when no voltage is applied to the sample under cross polarizers, the perfect and imperfect glass beads generate perfect rings or deformed curves of light, respectively. Figure 11 shows three glass beads with and without voltage, in which one can identify the deformed glass bead (central). Only this central glass bead attracts vortices.

In brief, spherical glass beads do not attract or repel umbilical defects. On the other hand, when the glass beads are not perfect, the equivalent charge of the glass bead and that of the Saturn ring do not coincide, creating a multipolar charge for the interaction with the defects. Hence, the interaction of an imperfect glass bead and umbilical defect can be modeled by

$$M\dot{\mathbf{r}} = q\left[\frac{\vec{d}}{||\mathbf{r}||^2} - \frac{\vec{d}\cdot\mathbf{r}}{||\mathbf{r}||^4}\mathbf{r}\right] + q\left[\frac{\vec{l}^2}{||\mathbf{r}||^4}\mathbf{r} + \frac{2\vec{l}(\vec{l}\cdot\mathbf{r})}{||\mathbf{r}||^4}\right], \quad (10)$$

where $\mathbf{r}(\mathbf{t})$ is the vector that joins the position between the glass bead and the vortex, $||\mathbf{r}||$ is the magnitude of the vector $\mathbf{r}$, $\vec{d}$ is a vector that characterizes the dipolar interaction, q is

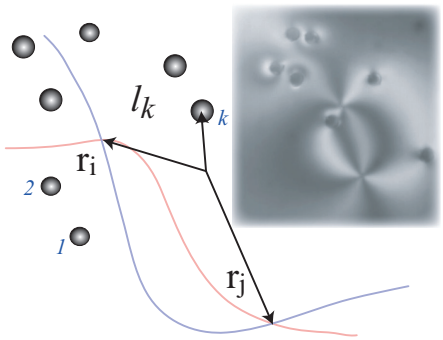

FIG. 12. Schematic representation of the vortex-pair interaction in the presence of glass beads. The index k accounts for the kth glass bead. $\mathbf{r_i}$ is the vector position of ith vortex. $\mathbf{l_k}$ is the vector position of the kth glass bead. The inset is an experimental snapshot obtained with the sample in-between crossed linear polarizers.

the topological charge of the interacting vortex, $\vec{l}$ is a vector that characterizes the quadrupolar interaction, and M stands for the vortex mobility. Note that the vectors $\vec{l}$ and $\vec{d}$ are not necessary parallels. On the right-hand side of Eq. (10), the first and second parentheses terms account, respectively, for the dipolar and quadrupolar interactions. Note that the dipolar and quadrupole interactions decay with the square and the cubic inverse of the distance between the vortices and the beads, respectively. From the experimental observations, we deduce that the quadrupole interaction is more dominant in the interaction ($\vec{d} \ll \vec{l}$, see Fig. 9). It is important to note that most of the glass beads do not attract vortices. However, the strength and direction parameters change each bead. Then, a detailed characterization of the vortex dynamics in a medium with spacers is a complex problem.

IV. SCREENING EFFECT AND COARSENING

The experimental observations show that some glass beads exert a force, either attractive or repulsive, on the vortices. Such a force is a power of the inverse of the distance between the bead and the vortices and has a different strength depending on the particular active bead considered. In order to shed light on the statistical vortex dynamics, let us consider two vortices in the presence of N' glass beads, as depicted in Fig. 12. For the sake of simplicity, we consider that glass beads are dominantly dipolar, *dipolar medium*.

Furthermore, we will use a similar strategy to derive third Kepler's law in the solar system, which is based on the fact that the n-body interaction (not self-similar) is approximated by the two-body interaction (self-similar), from which the third Kepler's law is inferred [42]. Let us consider a vortex gas in the presence of randomly distributed beads, which is described by

$$M\dot{\mathbf{r}}_\mathbf{i} = \sum_{j}^{N-1} \frac{q_{ij}}{||\mathbf{r_i}-\mathbf{r_j}||^2}(\mathbf{r_i}-\mathbf{r_j}) + \sum_{k=1}^{N'}\left[\frac{Q_{ik}\vec{d}_k}{||\mathbf{r_i}-\mathbf{l_k}||^2} - \frac{Q_{ik}[(\mathbf{r_i}-\mathbf{l_k})\cdot\vec{d}_k]}{||\mathbf{r_i}-\mathbf{l_k}||^4}(\mathbf{r_i}-\mathbf{l_k})\right], \quad (11)$$

where $\mathbf{r_i}$ stands for the position vector of ith vortex (cf. Fig. 12), M is the vortex mobility, q_{ij} is the product of the topological charges of the ith and jth vortices, Q_{ik} is the intensity of the interaction between the vortex, N and N' account for the number of vortices and beads and the kth bead, $\mathbf{l_k}$ and $\vec{d}_k$ are the vector position and the dipolar vector of kth glass bead, respectively.

Let us consider the limit of diluted vortices, that is, the distance between vortices $r \approx ||\mathbf{r_i}-\mathbf{r_j}||$ is much greater than the distance between a vortex and glass beads surrounding it ($||\mathbf{r_i}-\mathbf{r_j}| \gg ||\mathbf{r_i}-\mathbf{l_k}||$). Hence, the nearby glass beads dominate the dynamics of vortices, that is,

$$M\dot{\mathbf{r}}_\mathbf{i} \approx \sum_{k=1}^{N'} \frac{Q_{ik}}{||\mathbf{r_i}-\mathbf{l_k}||^2}\vec{d}_k + \sum_{k=1}^{N'} \frac{Q_{ik}(\mathbf{r_i}-\mathbf{l_k})\cdot\vec{d}_k}{||\mathbf{r_i}-\mathbf{l_k}||^4}(\mathbf{r_i}-\mathbf{l_k}). \quad (12)$$

In this limit, the dynamics of the vortices is not self-similar, however, when performing the transformation of spatial and temporal dilation

$$\mathbf{r_i} \to \lambda\mathbf{r_i}, \qquad t \to \lambda^3 t. \quad (13)$$

Eq. (15) takes the form

$$M\dot{\mathbf{r}}_\mathbf{i} \approx \sum_{k=1}^{N'} \frac{Q_{ik}\vec{d}_k}{||\mathbf{r_i}-\frac{\mathbf{l_k}}{\lambda}||^2} + \sum_{k=1}^{N'} \frac{Q_{ik}(\mathbf{r_i}-\frac{\mathbf{l_k}}{\lambda})\cdot\vec{d}_k}{||\mathbf{r_i}-\frac{\mathbf{l_k}}{\lambda}||^4}\left(\mathbf{r_i}-\frac{\mathbf{l_k}}{\lambda}\right). \quad (14)$$

The coarsening process is governed for large times and distances; therefore, one can consider λ to be large ($\lambda \gg 1$). Then, the above equation is rewritten

$$M\dot{\mathbf{r}}_\mathbf{i} \approx \sum_{k=1}^{N'} \frac{Q_{ik}\vec{d}_k}{||\mathbf{r_i}||^2} + \sum_{k=1}^{N'} Q_{ik}\frac{\mathbf{r_i}\cdot\vec{d}_k}{||\mathbf{r_i}||^4}\mathbf{r_i} + O\left(\frac{1}{\lambda}\right), \quad (15)$$

so that, if one dilates space and time on large scales, the equivalent set of Eqs. (5) are invariant at the dominant order. Furthermore, the vortex gas in such a disordered medium satisfies an effective dynamics governed by the previous interaction law. As we have mentioned before, the number of vortices at time t can be expressed as $N(t) = A/\langle r\rangle^2$, where A is the area of the sample under study and $\langle r\rangle$ is the average distance between vortices. Then, $\langle r\rangle$ and $N(t)$ should also be self-similar with the transformation (13). Hence, $N(\lambda^3 t) = A/\lambda^2\langle r\rangle^2$, and we obtain

$$N(t) = \frac{\beta_0}{t^{2/3}}, \quad (16)$$

where β_0 is constant. From this scaling law we obtain that the number of defects decreases with a $\alpha = -\frac{2}{3}$ power. Experimentally, several zones show exponents close to $-\frac{2}{3}$ (see Table I). Note that all the investigated zones, except zone III, show an exponent within 20% error from the $-\frac{2}{3}$ theoretical prediction. However, the dynamics of submerged vortices in an environment full of beads with various imperfections is much more complicated, as illustrated by the experimental results, and a full agreement over all the investigated zones could not be reached.

V. CONCLUSIONS AND REMARKS

Far from equilibrium systems with the coexistence of equilibria exhibit rich and complex defect dynamics in order to reach a more stable configuration. This dynamics of defects generates a rich variety of spatial textures. Defects in rotationally invariant two-dimensional systems attract a great deal of attention because of their universal character and intriguing topological properties. Nematic liquid crystals layer with negative dielectric constant and homeotropic anchoring under the influence of a voltage are the ideal context for studying the interaction of gas of topological vortices with opposite topological charges. One expects the dynamics of the vortices being characterized by a decreasing number in time, which follows a power law with critical exponent $\alpha = 1$ because the dominant interaction between the vortices is self-similar. Unexpectedly, we observe that this dynamics is persistent in thin cells of nematic liquid crystals that contain glass beads as spacers. However, the laws of the exponential decay in the number of vortices depend strongly on the distribution of the glass beads and their imperfections. Experimentally, we have characterized such a dynamics and demonstrated that the deformed glass beads attract vortices of opposite topological charges, presenting mainly a quadrupolar behavior. Theoretically, we have derived the modified power law for inhomogeneous samples, leading to $\alpha = \frac{2}{3}$ exponent of the power law. The agreement with the exponents derived from the experimental observations is satisfactory over several zones of the analyzed samples. However, a complete agreement could not be reached because of the diversity of the beads and the consequent complexity of the induced vortex dynamics.

Liquid crystal cells with spacers are fundamental in the development of displays of various electronic devices. The influence that the disperse beads, often used as spacers in the cell, can exert on the molecular reorientation is usually ignored. Our observations show that the inhomogeneities induced by the beads can play a relevant role in the dynamics of defects. Therefore, the study of the interaction between spacers and the surrounding liquid crystal can reveal important features of molecular behavior and could be taken into account for further improvements of liquid crystal devices.

ACKNOWLEDGMENTS

M.G.C. and V.Z. acknowledge financial support from the Millennium Institute for Research in Optics and FONDECYT Project No. 1180903.

[1] P. Ball, *The Self-Made Tapestry: Pattern Formation in Nature* (Oxford University Press, New York, 1999).
[2] P. Glansdorff and I. Prigogine, *Thermodynamic Theory of Structures, Stability and Fluctuations* (Wiley, New York, 1971).
[3] G. Nicolis and I. Prigogine, *Self-Organization in Non Equilibrium Systems* (Wiley, New York, 1977).
[4] M. C. Cross and P. C. Hohenberg, Rev. Mod. Phys. **65**, 851 (1993).
[5] L. M. Pismen, *Patterns and Interfaces in Dissipative Dynamics, Springer Series in Synergetics* (Springer, Berlin, 2006).
[6] M. Cross and H. Greenside, *Pattern Formation and Dynamics in Nonequilibrium Systems* (Cambridge University Press, New York, 2009).
[7] C. Kittel, *Introduction to Solid State Physics* (Wiley, New York, 1976).
[8] L. M. Pismen, *Vortices in Nonlinear Fields* (Clarendon, Oxford 1999).
[9] R. Barboza, U. Bortolozzo, G. Assanto, E. Vidal-Henriquez, M. G. Clerc, and S. Residori, Vortex Induction via Anisotropy Stabilized Light-Matter Interaction, Phys. Rev. Lett. **109**, 143901 (2012).
[10] R. Barboza, U. Bortolozzo, S. Residori, and E. Vidal-Henriquez, Optical vortex induction via light–matter interaction in liquid-crystal media, Adv. Opt. Photonics **7**, 635 (2015).
[11] E. Calisto, M. G. Clerc, M. Kowalczyk, and P. Smyrnelis, On the origin of the optical vortex lattices in an nematic liquid crystal light valve, Opt. Lett. **44**, 2947 (2019).
[12] S. Chandrasekhar, *Liquid Crystals* (Cambridge University Press, Cambridge 1992).
[13] P. G. de Gennes and J. Prost, *The Physics of Liquid Crystals*, 2nd ed. (Clarendon, Oxford, 1993).
[14] P. Oswald and P. Pieranski, *Nematic and Cholesteric Liquid Crystals* (Taylor & Francis, Boca Raton, FL, 2005)
[15] V. Freedericksz and V. Zolina, Forces causing the orientation of an anisotropic liquid, Trans. Faraday Soc. **29**, 919 (1927).
[16] A. Rapini, Umbilics: static properties and shear-induced displacements, J. Phys. (Paris) **34**, 629 (1973).
[17] O. Lehmann, Über fliessende krystalle, Z. Phys. Chem. **4U**, 462 (1889).
[18] G. Friedel, Les états mésomorphes de la matière Ann. Phys. (Paris) **18**, 273 (1922).
[19] F. C. Frank, Liquid crystals. On the theory of liquid crystals, Discuss. Faraday Soc. **25**, 19 (1958).
[20] T. Frisch, S. Rica, P. Coullet, and J. M. Gilli, Spiral Waves in Liquid Crystal, Phys. Rev. Lett. **72**, 1471 (1994).
[21] T. Frisch, Spiral waves in nematic and cholesteric liquid crystals, Phys. D (Amsterdam) **84**, 601 (1995).
[22] R. Barboza, T. Sauma, U. Bortolozzo, G., Assanto, M. G. Clerc, and S. Residori, Characterization of the vortex-pair interaction law and nonlinear mobility effects, New J. Phys. **15**, 013028 (2013).
[23] M. G. Clerc, E. Vidal-Henriquez, J. D. Davila, and M. Kowalczyk, Symmetry breaking of nematic umbilical defects through an amplitude equation, Phys. Rev. E **90**, 012507 (2014).
[24] E. Bodenschatz, W. Pesch, and L. Kramer, Structure and dynamics of dislocations in an anisotropic pattern-forming systems, Phys. D (Amsterdam) **32**, 135 (1988).
[25] F. Bethuel, H. Brezis, and F. Hélein, *Ginzburg-Landau Vortices* (Springer, New York, 2004).
[26] T. Nagaya, H. Hotta, H. Orihara, and Y. Ishibashi, Observation of annihilation process of disclinations emerging from bubble domains, J. Phys. Soc. Jpn. **60**, 1572 (1991).

[27] D. K. Ding and E. L. Thomas, Structures of point integer disclinations and their annihilation behavior in thermotropic liquid crystal polyesters, Mol. Cryst. Liq. Cryst. **241**, 103 (1994).

[28] I. Dierking, O. Marshall, J. Wright, and N. Bulleid, Annihilation dynamics of umbilical defects in nematic liquid crystals under applied electric fields, Phys. Rev. E **71**, 061709 (2005).

[29] A. N. Pargellis, S. Green, and B. Yurke, Planar XY-model dynamics in a nematic liquid crystal system, Phys. Rev. E **49**, 4250 (1994).

[30] M. Argentina, M. G. Clerc, R. Rojas, and E. Tirapegui, Coarsening dynamics of the one-dimensional Cahn-Hilliard model, Phys. Rev. E **71**, 046210 (2005).

[31] M. G. Clerc, S. Coulibaly, L. Gordillo, N. Mujica, and R. Navarro, Coalescence cascade of dissipative solitons in parametrically driven systems, Phys. Rev. E **84**, 036205 (2011).

[32] L. Ratke and P. W. Voorhees, *Growth and Coarsening: Ostwald Ripening in Material Processing* (Springer, New York, 2013).

[33] S. Hilgenfeldt, S. A. Koehler, and H. A. Stone, Dynamics of Coarsening Foams: Accelerated and Self-Limiting Drainage, Phys. Rev. Lett. **86**, 4704 (2001).

[34] T. Nagaya, H. Orihara, and Y. Ishibashi, Coarsening dynamics of +1 and -1 disclinations in two-dimensionally aligned nematics? Spatial distribution of disclinations, J. Phys. Soc. Jpn. **64**, 78 (1995).

[35] R. Barboza, U. Bortolozzo, M. G. Clerc, S. Residori, and V. Zambra, Coarsening dynamics of umbilical defects in inhomogeneous medium, in *Nonlinear Dynamics: Materials, Theory and Experiments* (Springer, Cham, 2016), pp. 31–43.

[36] K. Takatoh, M. Sakamoto, R. Hasegawa, M. Koden, N. Itoh, and M Hasegawa, *Alignment Technology and Applications of Liquid Crystal Devices* (CRC Press, Boca Raton, 2005), pp. 7–54.

[37] A. Gerrard and J. M. Burch, *Introduction to Matrix Methods in Optics* (Dover, New York, 1975).

[38] R. B. Meyer, On the existence of even indexed disclinations in nematic liquid crystals, Philos. Mag. **27**, 405 (1973).

[39] I. Dierking, Anisotropy in the annihilation dynamics of umbilic defects in nematic liquid crystals, Phys. Rev. E **85**, 021703 (2012).

[40] A. Okabe, N. Boots, K. Sugihara, and S. N. Chiu, *Spatial Tessellations: Concepts and Applications of Voronoi Diagrams* (Wiley, Chichester, 2009).

[41] H. Stark, Director field configurations around a spherical particle in a nematic liquid crystal, Eur. Phys. J. B **10**, 311 (1999).

[42] L. D. Landau and E. M. Lifshiftz, *Mechanics* (Pergamon, Oxford, 1976).

Appendix D

Exotic states of matter in an oscillatory driven liquid crystal cell

Publication Details

- Title: Exotic states of matter in an oscillatory driven liquid crystal cell
- Author: Marcel G. Clerc, Michal Kowalczyk, and Valeska Zambra
- Submited to: Scientific Reports

Exotic states of matter in an oscillatory driven liquid crystal cell

Marcel G. Clerc,[1] Michal Kowalczyk,[2] and Valeska Zambra[1]

[1] *Departamento de Física and Millennium Institute for Research in Optics, FCFM, Universidad de Chile, Casilla 487-3, Santiago, Chile.*

[2] *Departamento de Ingeniería Matemática and Centro de Modelamiento Matemático (UMI 2807 CNRS), Universidad de Chile, Casilla 170 Correo 3, Santiago, Chile*

Abstract. Matter under different equilibrium conditions of pressure and temperature exhibits different states such as solid, liquid, gas, and plasma. Exotic states of matter, such as Bose-Einstein condensates, superfluidity, chiral magnets, superconductivity, and liquid crystalline blue phases are observed in thermodynamic equilibrium. Rather than being a result of an aggregation of matter, their emergence is due to a change of a topological state of the system. Here we investigate topological states of matter in a system with injection and dissipation of energy. In an experiment involving a liquid crystal cell under the influence of a low-frequency oscillatory electric field, we observe a transition from non-vortex state to a state in which vortices persist. Depending on the period and the type of the forcing, the vortices self-organise forming square lattices, glassy states, and disordered vortex structures. Based on a stochastic amplitude equation, we recognise the origin of the transition as the balance between stochastic creation and deterministic annihilation of vortices. Our results show that the matter maintained out of equilibrium by means of the temporal modulation of parameters can exhibit exotic states.

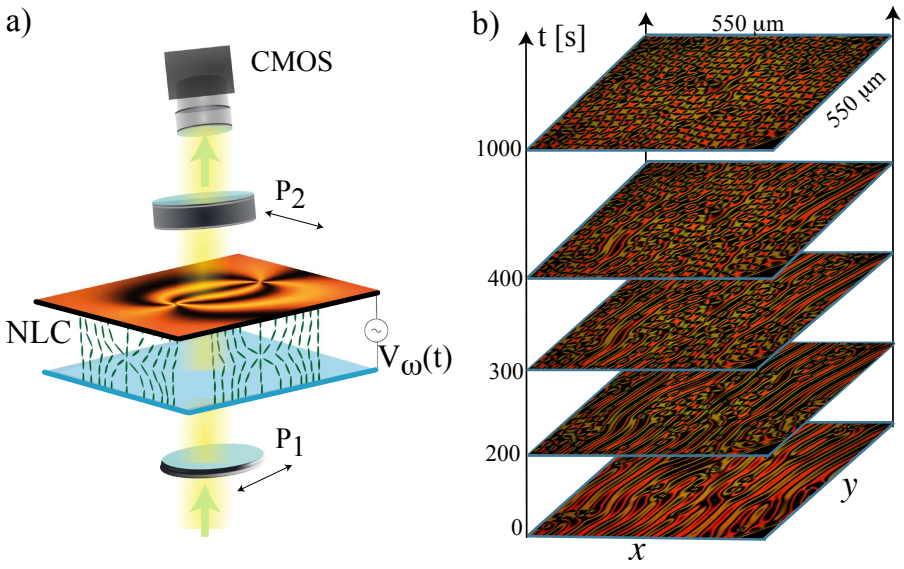

Figure 1. Liquid crystal cell under a temporarily modulated potential exhibits creation and self-organisation of vortices. (a) Schematic representation of the experimental setup. Liquid crystal cell (NLC) with homeotropic anchoring is illuminated by white light between two crossed polarisers (P_1 and P_2). The horizontal snapshot shows a pair of vortices with opposite charges. (b) The temporal sequence of snapshots in the region of self-organised vortices, at frequency 0.335 Hz and voltage amplitude 13.5 Vpp. From experimental snapshots, both figures were created using Inkscape 1.0.

I. INTRODUCTION

Solid, liquid, gas, and plasma are different states of the matter[1] distinguished from each other by mechanical, optical, and other properties. Other examples of states of aggregation of matter include glassy and liquid crystal states. Still different are exotic states such as Bose-Einstein condensates [2], superfluidity [3], superconductivity [6], chiral magnets [4], and liquid crystalline blue phases [5] that are a topological state rather than an aggregation of matter. The topological transitions of the matter were discovered at the beginning of the 70s by Berezinskii [7] and Kosterlitz and Thouless [8], who showed that a low dimensional system described by a physical vector order parameter in thermodynamic equilibrium undergoes a transition from a homogeneous state without vorticity to a state in which vorticity persists. In the homogeneous state all vectors are unidirectionally ordered but under suitable conditions they realign forming regions where both their orientations and magnitudes vary. Because of topological constraints at some isolated points called vortices [9] the vector field vanishes and the vector phase becomes undefined. The winding number (topological charge) is introduced to characterise the physical vector field around a vortex [9]. This number is an integer representing the total number of times that the vector field winds around the origin while varying along a closed, counterclockwise oriented curve around the singular point. Topological stability of the system implies that the total winding number of the system must be preserved which means that the vortices are created or annihilated by pairs of opposite topological charges. Vortices creations and and annihilation process are, respectively, due to thermal fluctuations and free energy minimisation [10, 11], hence at a critical temperature at which they are balanced the systems undergoes a topological transition [7, 8]. Exotic states of matter such as Bose-Einstein, superconductivity, chiral magnets, and superfluidity are usually observed at low temperatures, however liquid crystalline blue phases have been observed at room temperature [12].

An ideal material to investigate vortex dynamics are liquid crystals in thin films [5, 13]. One of the most studied vortices are the so-called umbilical defects or disclination lines [5, 13, 14]. In thermodynamic equilibrium and homogeneous media, the vortices tend to annihilate by pairs to minimise the free energy of the system. The above dynamics can be modified by means of incorporation of inhomogeneities, which can attract and trap umbilical defects [15, 16]. Properly distributed inhomogeneities may permit the formation of topology lattice [15]. Likewise, considering inhomogeneous anchoring allows attracting and trapping umbilical defects and creating vortex lattices [17, 18]. A similar effect can be achieved by the introduction of inhomogeneous electrodes [19–22]. The combined use of magnets and uniform electric field can induce umbilical defects and lattices [23]. The vortex lattices describe above are induced by the combination of the forcing and inhomogeneities. However, the emergence of spontaneous

topological lattices has also been achieved by means of thermal gradients [24] or by doping with ionic impurity [20], which induces charge motions. This is known as the Carr-Helfrichh mechanism [5]. This article aims to study exotic states of matter with injection and dissipation of energy. This type of physical context usually is denominated as out of equilibrium systems [25, 26]. Based on an experiment involving a nematic liquid crystal cell under the influence of a low-frequency oscillatory electric field, we observe a transition from non-vortex state to a state in which vortices persist. Depending on the frequency and the type of the forcing, the vortices self-organise forming square lattices, glassy states, and disordered vortex structures. Theoretically, a stochastic amplitude equation allows us to reveal the origin of the transition in terms of the balance between stochastic creation and deterministic annihilation of vortices.

II. RESULTS

Experimental observations of a topological transition in a driven liquid crystal cell. Liquid crystals are composed of rod-like organic molecules [5, 13, 14] which, as a result of intermolecular interaction, for specific temperature ranges are arranged to have a similar molecular orientation. This results in a strong anisotropy of all their physical properties, especially optical characteristics [27]. The configuration of lowest energy is reached when all rod-like molecules are aligned along one averaged direction, orientational order without a positional one, denoted by the director vector $\mathbf{n}$ [5, 13, 27]. This state is usually called the nematic phase. In the case of a thin film with negative dielectric anisotropy and molecular anchoring perpendicular to the walls of the sample, application of an electric field in the vertical direction leads to the appearance of vortices, umbilic defects or disclination lines [5, 13, 14]. Figure 1b shows the spatiotemporal evolution of vortex arrangements experimentally observed by applying a voltage $V(t) = V\sin(2\pi f t)$ with a given frequency f, i.e, harmonic voltage signal. To avoid charges accumulation effects in the thin film (capacity effects), a high frequency oscillatory electric field (kHz) is usually used. Under these conditions in a homogeneous liquid crystal cell the emergence of gas of disordered vortices is followed by the subsequent annihilation by pairs, and terminates in a homogenous, non-vortex state [10, 11, 13]. Thus the vortices are a transient phenomenon. Surprisingly, when the frequency of the electric field that we applied to the homogeneous liquid crystal cell decreases to fractions of Hz starting from a critical value of the frequency, the system exhibits a topological transition after which the annihilation and creation are balanced, and the vortices persist (see video 1 in supplementary materials). Hence, the bifurcation parameter of this transition is the frequency f of the drive voltage. Figure 2 shows the average number of vortices as a function of frequency counted stroboscopically in each oscillation cycle with the standard deviation determined along the way. This transition is obtained by considering a sawtooth signal for the voltage applied to the sample. From this chart, one deduces that the transition is of continuous nature (supercritical bifurcation) and that there is a critical frequency f_c from which the number of vortices in average becomes permanent over time (frequency $< f_c$). We note that as the frequency decreases the number of vortices increases to a particular critical value and subsequently decreases monotonically until it vanishes at low frequencies, which is a manifestation of a sort of resonance for the process of creation and destruction of topological defects. Notice that periodically driven voltage only induces umbilical defects, no other defects are observed. The application of a low-frequency electric field induces charge movements due to the weak anisotropic conductivity of the liquid crystal [5]. The accumulation of charges can induce a molecular reorientation, Carr-Helfrich mechanism [5], which in turn modifies the interaction between umbilical defects and can even generate a lattice arrangement of them [24].

Using a thermal control microscope stage, the temperature of the liquid crystal sample can be changed and controlled adequately. When the temperature at which the experiments are made is varied, we observe that critical frequency transition f_c grows monotonically with it as illustrated in Figure 2c. The tendency to increase the transition frequency at higher temperatures is due to the increasing the rate of vortex creation (fluctuations), while the process of vortices annihilation remains unchanged (deterministic). Therefore, the topological transition induced by temporal voltage modulation is observed throughout the mesophase stability range of the nematic liquid crystal under study.

Theoretical description of the topological transition. To understand the origin of this topological transition out of equilibrium, we consider a prototype model, the Ginzburg-Landau equation [28], that describes the emergence of topological defects in fluids, superfluids, superconductors, liquid crystals, chiral magnets, fluidised anisotropic granular matter, and magnetic media [9, 28]. The real Ginzburg-Landau equation describe the pattern formation in anisotropic media [29]. Likewise, this model describes vortex solutions in nematic liquid crystal layers with external electric or magnetic forcing and homeotropic boundary conditions [30–33], and the formation of spiral waves in a nematic liquid crystal subjected to a rotating magnetic [30, 32] or electric field [31]. Note that this Ginzburg-Landau equation with real coefficients is derived from the elastic theory of liquid crystals [30–34]. The order parameter accounts for the balance between the elastic and electric force. Besides, this model describes the process of interaction and annihilation of vortices at constant electric field and temperature [11]. To account for the additional ingredients

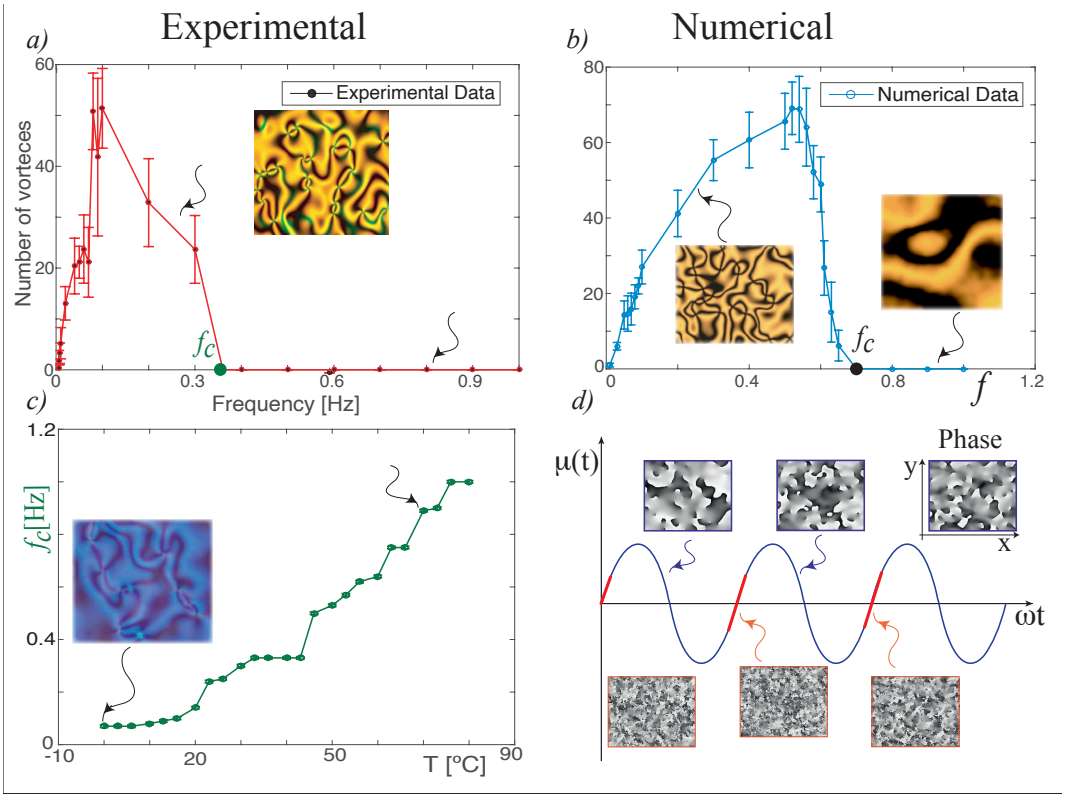

Figure 2. Bifurcation diagram of topological transition out of equilibrium (a) experimental and (b) numerical using model Eq. (1). The experimental bifurcation diagram is obtained with a sawtooth forcing with a fixed amplitude voltage 15 Vpp. (c) Critical frequency $f_c(T)$ as a function of temperature with a fixed amplitude voltage 15 Vpp. The insets account for the respective snapshots in the different regions. (d) Evolution of the temporal bifurcation parameter $\mu(t)$ and characterisation of the regimes of creation (red curve) and interaction (blue curve) of vortices. Inserts show the phase obtained numerically in the different creation and interaction regimes. From experimental snapshots, both figures were created using Inkscape 1.0.

of the observed topological transition (cf. Fig. 2), we must incorporate the oscillatory nature of the electrical voltage applied to the liquid crystal sample and include the inherent fluctuations due to temperature. This leads to the stochastic Ginzburg-Landau equation with oscillatory coefficients, that is,

$$\partial_t A = [\mu_0 + \gamma\cos(2\pi f t)]\, A - |A|^2 A + \nabla^2 A + \sqrt{T}\zeta(\vec{r},t), \tag{1}$$

where $A(\vec{r},t)$ is a complex order parameter, t and $\vec{r}$ describe time and the transversal coordinate vector that characterises the thin film, μ_o is the uniform bifurcation parameter, γ and f are the amplitude and the frequency of the forcing, respectively, which account for the oscillatory electric field. The function $\mu(t) = \mu_0 + \gamma\cos(2\pi f t)$ is the temporal modulated bifurcation parameter. By ∇^2 we denote the Laplace operator. The constant T accounts for the thermal intensity and $\zeta(\vec{r},t)$ is a spatiotemporal white noise of zero mean value, $\langle\zeta(\vec{r},t)\rangle = 0$, and no spatial or temporal memory. Namely, the stochastic term has the spatiotemporal correlation $\langle\zeta(\vec{r},t)\zeta(\vec{r}',t')\rangle = \delta(\vec{r}-\vec{r}')\delta(t-t')$ where δ are Dirac delta functions.

In the high-frequency regime, $f \to \infty$, this model becomes the Ginzburg-Landau equation with real coefficients. This equation is characterised by a constant effective bifurcation parameter $\mu_0 + 3\gamma^2/2(2\pi f)^2$ obtained through the rapid oscillation method [35]. In this limit the vortices do not persist and the annihilation of the defects of opposite charges dominates their creation [9, 11], since the system tries to optimise the effective free energy. Figure 2b shows this happening for frequency values up to order one. In this regimen, for large enough temporary evolution, the number of vortices on average is zero. By decreasing the frequency further to a critical value f_c, the average number of vortices stabilises over time. The topological transition obtained numerically using Eq. (1) has a qualitative behaviour similar to that observed experimentally, see top panels in Fig. 2. Notice that as the frequency decreases ($f < f_c$) the number of vortices increases to a particular critical value and subsequently decreases monotonically until it vanishes at low frequencies, which manifests an excellent qualitative agreement with the experimental observations.

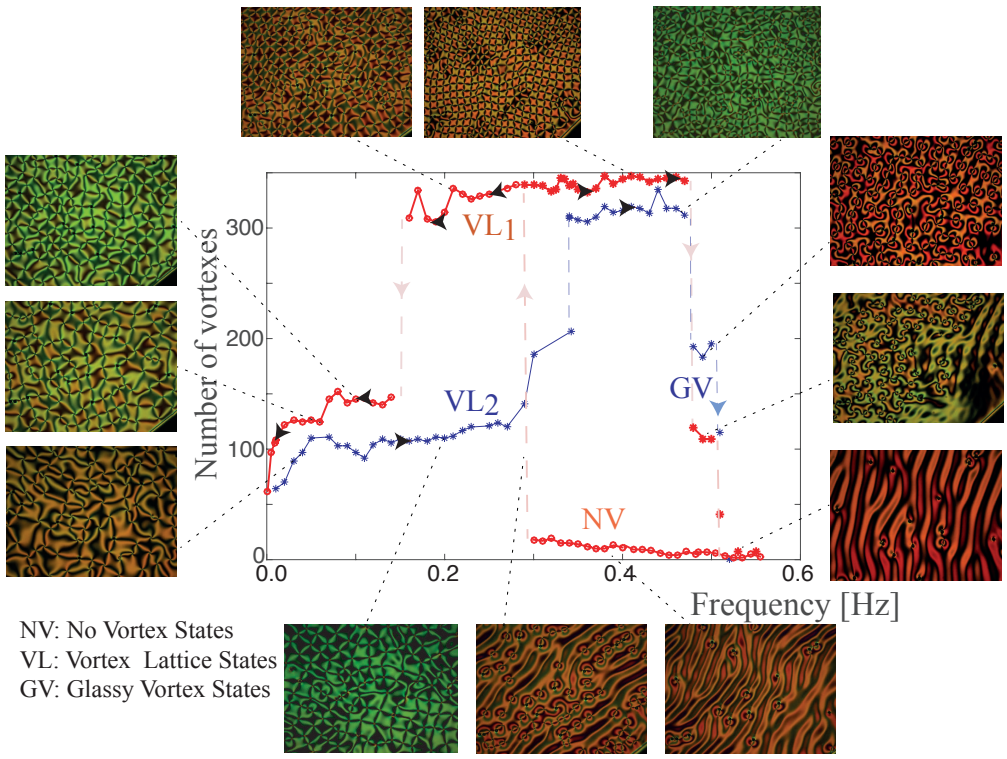

Figure 3. Experimental bifurcation diagram of topological transition out of equilibrium under harmonic forcing. The liquid crystal cell exhibits three states: non-vortex (NV), vortex lattice (VL) and glassy vortex (GV) states. The arrows indicate the direction of increase or decrease of the voltage. The insets show snapshots in the respective parameter ranges. From experimental snapshots, figures were created using Inkscape 1.0.

Hence, experimentally and numerically a sort of resonance is observed for the process of creation and destruction of topological defects.

The simulation allows us to identify the location of the vortices through $\pm 2\pi$ jumps of the phase of the amplitude. Comparing the evolution of the system and the profile of the bifurcation parameter function $\mu(t)$ two characteristic regions are identified. Namely, a creation and annihilation region. Creation of vortices occurs in the intervals of time where $\mu(t)$ is small and growing (red curve in Fig. 2d), these vortices later interact even when $\mu(t) < 0$ (blue curve in Fig. 2d). The region of creation and annihilation are govern by stochastic fluctuations and deterministic evolution, respectively. The vortex creation time interval decreases as the forcing frequency increases and for high frequencies the creation process is inefficient. Hence, the persistence of vortices is a consequence of the balance between the processes of creation (stochastic) and their interaction (deterministic).

Topological transition with harmonic driven forcing. In experiments we have implemented various types of periodic forcing among them harmonic, sawtooth, or square profiles and we have found, somewhat unexpectedly, different types of responses resulting in diverse transitions. As we have mentioned, low-frequency voltages can induce charge movements that, in turn, induce molecular reorientation, Carr-Helfrich mechanism [5]. Hence, different types of driven voltages can induce different charge motions. In the case of a square profile signal, we have observed a continuous or supercritical topological transition (see Fig. 1a). Changing to a harmonic signal, we have detected a discontinuous transition with the non-vortex state being replaced by a vortex lattice with a square crystalline structure. Figure 3 shows a square vortex lattice and its respective bifurcation diagram corresponding to the out of equilibrium counterpart of Abrikosov lattice [36, 37]. The vortex lattice in not hexagonal like the one of Abrikosov as a consequence of the asymmetry between the opposite charges [33]. The model Eq. (1) only accounts for the topological transition from disordered vortices to non-vortex state. The origin of these square vortex lattices is probably associated with the coupling of elastic deformations and fluid modes. To account qualitatively of this coupling, we include in the model Eq. (1) inertia and anisotropic effects, that is, a second temporal derivative of amplitude A. Simulations of this model show the emergence of a square lattice, as seen in Fig. 4. The Ginzburg-Landau Eq. (1) is a model infer close to the reorientational transition [32, 34]. Its derivation is based on the assumption of slowly varying amplitude; however,

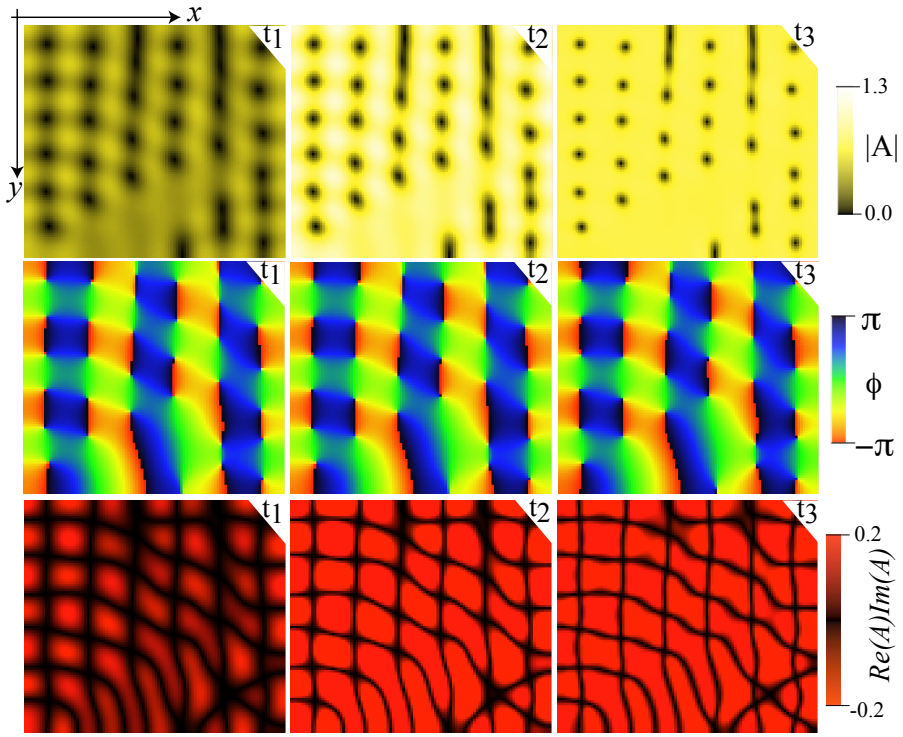

Figure 4. Numerical square vortex lattice. Temporal sequence ($t_1 < t_2 < t_3$) of the amplitude module $|A|$, phase $\phi = arctan[Im(A)/Re(A)]$, and polarisation field $Re(A)Im(A)$ of model Eq. (2) with inertia and anisotropic coupling over a period, by $\mu_0 = 0.6$, $T = 0.03$, $\lambda = 1.4$, $\delta = 0.3$, $\gamma = 3$, and $f = 0.1$. From numerical simulations, figure was created using Inkscape 1.0.

when the system is periodically forced, the first and second temporal variations can be of the same order. The inertia term phenomenologically accounts for the effects of movements of charges and liquid crystal inside the cell.

When decreasing the frequency, the square lattice undergoes a subcritical bifurcation leading to a square lattice of higher wavelength (see Fig. 3 and supplementary video 2). Increasing the frequency further the square lattice transitions to a glassy state (cf. Fig. 3 and supplementary video 3), in which the vortex structure does not have a precise unit cell. For even higher frequencies the system returns to the non-vortex state. Figure 3 summarises the complexity of the topological transitions in the liquid crystal cell maintained out of equilibrium at room temperature. We speculate that the origin of the periodic structures we have discovered may be associated with the interaction between the vortices or the excitation of stationary waves [49], however, precise understanding of this is an open problem.

III. DISCUSSION

Topological defects in liquid crystals are natural elements used for the generation of optical vortices [17, 21, 38–40]. As a matter of fact, optical vortices have attracted attention for their diverse photonic applications ranging from optical tweezers [41, 42], quantum computation [43], enhancement of astronomical images [44]. In all these applications, optical vortex lattices are always involved and required [45–48]. These vortex lattices require sophisticated and complex experimental setup. Instead, he vortex lattice that we observe emerge spontaneously in simple liquid crystal cells that do not require a complex structure of electrodes, inhomogeneities, applications of thermal gradients, combined forcing of electric and magnetic fields, or photosensitive walls.

In conclusion, we have shown that exotic states of matter with injection and dissipation of energy. In a nematic liquid crystal cell under the influence of a low frequency oscillatory electric field, we have observe transitions from non-vortex state to a state in which vortices persist. Depending on the frequency and type of the forcing (harmonic, sawtooth, or square profiles), the vortices self-organise forming square lattices, glassy states, and disordered vortex structures. Because the phenomenon reported here is qualitatively well described by a universal model Eq. (1), we

expect that any temporally modulated vectorial field system of low dimensionality can exhibit topological transitions out of equilibrium. The characterisation of the critical frequency and voltage as a function of liquid crystal features and cell configuration is an open question. Work in this direction is in progress. Furthermore, these findings could be a starting point for understanding and controlling the exotic states of matter out of equilibrium by means of the temporal modulation of parameters. Because vortex lattices emerge spontaneously in single cells subjected to alternative low-frequency voltages, it opens up the possibility of new and fresh applications of the generation of optical vortices.

Methods: Experimental description of the setup. Figure 1a shows a schematic representation of the experimental setup. It consists of a liquid crystal cell composed of two glass slabs with 600 mm^2 of cross-section separated by a distance of 15 μm, a thin film of a transparent conductor, indium tin oxide (ITO), and a thin film of transparent polyimide that has been deposited on each of the interior walls. Transparent conductors are used as electrodes. By rubbing process, microscopic grooves are generated in the polyimide layer, allowing the liquid crystal molecules anchoring orthogonally to the surfaces, homeotropic anchoring. This cell 5B100A150UT180 manufactured by Instec, contains glass beads as spacers. It is filled by capillarity with BYVA-01-5G (Instec) nematic liquid crystal that has negative anisotropy, $\epsilon_a = -4.89$ at room temperature. An external electric field is applied in the vertical direction (z-axis) using a sinusoidal sawtooth, or square voltage with amplitude 15 Vpp with low frequency. This voltage is produced by a function generator (Agilent 33521A) with a high voltage amplifier (Tabor Electronics 9200). The imaging system used is an Olympus BX51 microscope equipped with linear cross polarisers. The light from the microscope condenser illuminates the cell mounted on the microscope stage, and a CMOS camera (Thorlabs DCC1645C) is used to capture images. For studying thermal effects we used Leica DM2700 P microscope equipped with LTS420 hot stage.

Numerical Simulations. Numerical simulations of model Eq. (1) were implemented using a finite differences code with Runge-Kutta order-4 algorithm, with a 200×200 points grid, spacing $dx = 0.5$, and temporal increment $dt = 0.02$. Numerical simulations are performed with periodic boundary conditions and with an initial condition $A = 0$. The stochastic noise $\zeta(\vec{r}, t)$ is generated through the Box-Muller transform of a uniform random number generator. Equation (1) with inertia and anisotropic effects reads

$$\partial_{tt}A + \lambda\partial_t A = [\mu_0 + \gamma\cos(2\pi f t)]\, A - |A|^2 A + \nabla^2 A + \delta\partial_{\eta,\eta}\bar{A} + \sqrt{T}\zeta(\vec{r}, t), \tag{2}$$

where λ accounts for the rotational viscosity, δ stands for the difference of elastic constants [30–33], the operator $\partial_{\eta,\eta} = \partial_{xx} - \partial_{yy} + 2i\partial_{xy}$ describes the asymmetric coupling, and $\bar{A}$ is the complex conjugate of A. The results presented in figure 4 consider the same algorithm, boundary and initial conditions used in equation (1).

Reference

[1] Goodstein D.L. *States of Matter* (Dover publications, New York, 1985).
[2] Pethick, C. J., & Smith, H. *Bose-Einstein condensation in dilute gases* (Cambridge university press, New York, 2008).
[3] Tsuneto, T. *Superconductivity and superfluidity* (Cambridge University Press, New York,2005).
[4] Mühlbauer, S., Binz, B., Jonietz, F., Pfleiderer, C., Rosch, A., Neubauer, A., Georgii, R., & Böni, P. Skyrmion lattice in a chiral magnet. *Science*, **323**, 915-919. (2009).
[5] de Gennes, P.G. & Prost, J. *The physics of Liquid Crystals*, 2nd edn. (Oxford Science Publications, Clarendon Press, 1993).
[6] Tinkham M. *Introduction to superconductivity* (McGraw-Hill, New York, 1996).
[7] Berezinskii, V. L. Destruction of long-range order in one-dimensional and two-dimensional systems having a continuous symmetry group I, Classical systems. *Sov. Phys. JETP* **32**, 493-500 (1971).
[8] Kosterlitz, J. M., & Thouless, D.J. Ordering, metastability and phase transitions in two-dimensional systems. *J. Phys. Condens. Matter* **6** 1181-1203 (1973).
[9] Pismen L.M. *Vortices in Nonlinear Fields* (Oxford Science, New York, 1999).
[10] Dierking, I., Marshall, O., Wright, J., & Bulleid, N. Annihilation dynamics of umbilical defects in nematic liquid crystals under applied electric fields. *Phys. Rev. E*, **71**, 061709 (2005).
[11] Barboza, R., Sauma T., Bortolozzo, U., Assanto G., Clerc, M.G., & Residori, S. Characterization of vortex pair interaction law and nonlinear. *New J. Phys.* **15**, 013028 (2013).
[12] Coles, H.J., & Pivnenko, M.N. Liquid crystal 'blue phases' with a wide temperature range. *Nature* **436**, 997-1000 (2005).
[13] Chandrasekhar, S. *Liquid Crystal* (Cambridge, New York, 1992).
[14] Rapini, A. Umbilics: static properties and shear-induced displacements. *J. Phys. (Paris)* **34**, 629-633 (1973).

[15] Kim, M., & Serra, F. Tunable Dynamic Topological Defect Pattern Formation in Nematic Liquid Crystals. *Adv. Opt. Mater.* **8**, 1900991 (2020).
[16] Zambra, V., Clerc, M.G., Barboza, R., Bortolozzo, U., & Residori, S. Umbilical defects dynamics in an inhomogeneous nematic liquid crystal layer. *Phys. Rev. E.* **101**, 062704 (2020).
[17] Marrucci, L., Manzo, C., & Paparo, D. Optical Spin to Orbital Angular Momentum Conversion in Inhomogeneous Anisotropic Media. *Phys. Rev. Lett.* **96**, 163905 (2006).
[18] Murray, B. S., Pelcovits, R. A., & Rosenblatt, C. Creating arbitrary arrays of two-dimensional topological defects. *Phys. Rev. E* **90**, 052501 (2014).
[19] Loussert, C., Kushnir, K., & Brasselet, E. Q-plates micro-arrays for parallel processing of the photon orbital angular momentum. *Appl. Phys. Lett.* **105**, 121108 (2014).
[20] Sasaki, Y., Jampani, V. S. R., Tanaka, C., Sakurai, N., Sakane, S., Le, K. V., Araoka F., & Orihara, H. Large-scale self-organization of reconfigurable topological defect networks in nematic liquid crystals. *Nat. Commun.* **7**, 1-13 (2016).
[21] Salamon, P., Éber, N., Sasaki, Y., Orihara, H., Buka, Á., & Araoka, F. Tunable Optical Vortices Generated by Self-Assembled Defect Structures in Nematics. *Appl. Phys. Lett.* **10**, 044008 (2018).
[22] Harkai, S., Murray, B. S., Rosenblatt, C., & Kralj, S. Electric field driven reconfigurable multistable topological defect patterns. *Phys. Rev. Research* **2**, 013176 (2020).
[23] Pieranski, P., Yang, B., Burtz, L. J., Camu, A., & Simonetti, F. Generation of umbilics by magnets and flows. *Liq. Cryst.* **40**, 1593-1608 (2013).
[24] Pieranski, P., Dubois-Violette, E., & Guyon, E. Heat convection in liquid crystals heated from above. *Phys. Rev. Lett.* **30**, 736-739 (1973).
[25] Nicolis, G. & Prigogine, I. *Self-Organization in Non Equilibrium Systems* (Wiley, New York, 1977).
[26] Haken H. *Information and self-organization: A macroscopic approach to complex systems* (Springer Science & Business Media, Berlin, 2006).
[27] Blinov, L.M. *Structure and Properties of Liquid Crystals* (Springer, Dordrecht, 2011).
[28] Aranson, I.S., & Kramer, L. The world of the complex Ginzburg-Landau equation. *Rev. Mod. Phys.* **74**, 99-143 (2002).
[29] Pesch, W., & Kramer, L. Nonlinear analysis of spatial structures in two-dimensional anisotropic pattern forming systems. *Z. Phys. B* **63**, 121-130 (1986).
[30] Frisch, T., Rica, S., Coullet, P., & Gilli, J.M. Spiral waves in liquid crystal. *Phys. Rev. Lett.* **72**, 1471-1474 (1994).
[31] Coullet, P., & Plaza, F. Excitable spiral waves in nematic liquid crystals. *Internat. J. Bifur. Chaos* **4**, 1173-1182 (1994).
[32] Frisch, T. Spiral waves in nematic and cholesteric liquid crystals. *Physica D* **84**, 601-614 (1995).
[33] Clerc, M.G., Vidal-Henriquez, E., Davila, J.D., & Kowalczyk, M. Symmetry breaking of nematic umbilical defects through an amplitude equation. *Phys. Rev. E* **90**, 012507 (2014).
[34] Barboza, R., Bortolozzo, U., Clerc, M. G., Residori, S., & Vidal-Henriquez, E. Optical vortex induction via light-matter interaction in liquid-crystal media. *Adv. Opt. Photon.* **7**, 635 (2015).
[35] Landau, L.D., & Lifshitz, E.M. *Classical mechanics* (Pergamon Press, Oxford, 1960).
[36] Abrikosov, A.A. The magnetic properties of superconducting alloys. *J. Phys. Chem. Solids* **2**, 199-208 (1957).
[37] Abo-Shaeer, J.R., Raman, C., Vogels, J.M., & Ketterle, W. Observation of vortex lattices in Bose-Einstein condensates. *Science* **292**, 476-479 (2001).
[38] Brasselet, E., Murazawa, N., Misawa, H., & Juodkazis, S. Optical vortices from liquid crystal droplets. *Phys. Rev. Lett.* **103**, 103903 (2009).
[39] Barboza, R., Bortolozzo, U., Assanto, G., Vidal-Henriquez, E., Clerc, M. G., & Residori, S. Vortex induction via anisotropy stabilized light-matter interaction. *Phys. Rev. Lett.* **109**, 143901 (2012).
[40] Chen, P., Ma, L.L., Duan, W., Chen, J., Ge, S.J., Zhu, Z.H., Tang, M.J., Xu, R., Gao, W., Li, T., Hu, W., & Lu, Y.Q. Digitalizing Self-Assembled Chiral Superstructures for Optical Vortex Processing. *Adv. Mater.* **30**, 1705865 (2018).
[41] Grier, D. G. A revolution in optical manipulation. *Nature* **424**, 810-816 (2003).
[42] Padgett, M., & Bowman, R. Tweezers with a twist. *Nat. Photonics* **5**, 343-348 (2011).
[43] Arnaut, H. H., & Barbosa, G. A. Orbital and intrinsic angular momentum of single photons and entangled pairs of photons generated by parametric down-conversion. *Phys. Rev. Lett.* **85**, 286-289 (2000).
[44] Tamburini, F., Anzolin, G., Umbriaco, G., Bianchini, A., & Barbieri, C. Overcoming the Rayleigh criterion limit with optical vortices. *Phys. Rev. Lett.* **97**, 163903 (2006).
[45] Wang J., Yang J.-Y., Fazal I.M., Ahmed N., Yan Y., Huang H., Ren Y., Yue Y., Dolinar S., Tur M., & Willner A.E. Terabit free-space data transmission employing orbital angular momentum multiplexing. *Nat. Photonics* **6**, 488-496 (2012).
[46] Barboza, R., Bortolozzo, U., Assanto, G., Vidal-Henriquez, E., Clerc, M.G., & Residori, S. Harnessing optical vortex lattices in nematic liquid crystals, *Phys. Rev. Lett.* 111, 093902 (2013).
[47] Lei, T., Zhang, M., Li, Y.R., Jia, P., Liu, G.N., Xu, X.G., Li, Z.H., Min, C.J., Lin, J., Yu, C.Y., Niu, H.B., & Yuan, X.C. Massive individual orbital angular momentum channels for multiplexing enabled by Dammann gratings. *Light Sci. Appl.* **4**, e257 (2015).
[48] Stoyanov, L., Maleshkov, G., Zhekova ,M., Stefanov, I., Neshev, D.N., Paulus, G.G., & Dreischuh, A. Far-field pattern formation by manipulating the topological charges of square-shaped optical vortex lattices. *J. Opt. Soc. Am. B* **35**, 402-409 (2018).
[49] Migara, L.K., & Song, J.K. Standing wave-mediated molecular reorientation and spontaneous formation of tunable, concentric defect arrays in liquid crystal cells. *NPG Asia Materials* **10**, e459 (2018).

Acknowledgements: The authors thank M. Morel and G. Gonzalez for fruitful discussions. The authors acknowl-

edges the financial support of the Millennium Institute for Research in Optics (MIRO), Fondecyt project 1180903 and 1170164, and Fondo Basal CMM-Chile.

Author contributions M.G.C. and V.Z. conceived the experiments. V.Z. performed the experiments and analysed the data. M.G.C. and V.Z. performed the numerical computations. M.G.C., M.K., and V.Z. worked on the theoretical description. M.G.C. wrote the first draft of the article. All authors contributed to the overall scientific interpretation and edited the manuscript.

Competing interests: The authors declare that they have no competing financial interests.

Correspondence: Correspondence and requests for materials should be addressed to M.G.C. (email: marcel@dfi.uchile.cl), https://orcid.org/0000-0002-8006-0729.

Appendix E

Magnetic ring induced a vortex triplet and vortex lattice in a liquid crystal cell

Publication Details

- Title: Magnetic ring induced a vortex triplet and vortex lattice in a liquid crystal cell
- Author: Enrique Calisto, Marcel G. Clerc, and Valeska Zambra
- Submited to: Physical Review Letters

Magnetic ring induced a vortex triplet and vortex lattice in a liquid crystal cell

Enrique Calisto,[1,2] Marcel G. Clerc,[1] and Valeska Zambra[1]

[1] *Departamento de Física and Millennium Institute for Research in Optics, FCFM, Universidad de Chile, Casilla 487-3, Santiago, Chile*

[2] *Departamento de Ingeniería Matemática, FCFM, Universidad de Chile*

(Dated: July 26, 2020)

Vortices are particle-type solutions with topological charges that can steer the dynamics in various physical systems. By the application of electromagnetic fields onto a homeotropic nematic liquid crystal cell, we are able to induce a vortex triplet that remains stable and trapped at a given location. For a low frequency of the driven voltage, we observe that the vortex triplet is unstable and gives rise to the appearance of a topological lattice. Based on an amplitude allow us to reveal the origin of the vortex triplet and lattice. Numerical simulations show a quite fair agreement with theoretical findings and experimental observations.

Continuous media are characterized by exhibiting different robust phenomena such as waves, fronts, patterns, and dissipative structures [1–4]. One of the most attractive dynamic behaviors is particle-type solutions or localized structures, where solitons are the paradigmatic example [5, 6]. These dynamic behaviors are extended spatially; however, they exhibit characteristics associated with particles such as a position, amplitude, charge, width, among others. The localized structures are understood as patterns appearing in a restricted region of space [7–10]. Dissipative particle-type solutions have been theoretically predicted and experimentally observed in many fields of nonlinear science, such as laser physics, hydrodynamics, fluidized granular media, gas discharge systems, chemical reactions, magnetic media, and biology (see reviews [7–10] and references therein). Localized structures can be created or destroyed by localized disturbances [7–11]. All these features change radically when one considers particles-type solutions with topological charges, *vortices* [12]. Vortices are pointlike singularities that take place in complex fields, which locally break the rotation symmetry. They present zero intensity at the singular point with a phase spiraling around it. The topological charge is allocated by counting the number of phase jumps, while the sign is given by the direction of the spiral rotation. Conventionally, it is positive (negative) when the rotation is counterclockwise (clockwise). As a consequence of the conservation of topological charge, vortices are created and annihilate by pairs between opposite charges [12]. In addition, this conservation precludes that a local disturbance would destroy vortices. Indeed, the possession of a topological charge provides vortices with a topological stability, as occurs with fundamental particles [12]. A paradigmatic field model that presents vortices is the Ginzburg-Landau equation [12, 13]. This amplitude equation have been used to describe fluids, superfluids, superconductors, liquid crystals, granular matter, magnetic media, and optical dielectrics, to mention a few [12–15].

A natural physical context where dissipative vortices are observed is in liquid crystals [16, 17]. Vortices in this context are usually called umbilical defects or disclination lines. Considering a thin film of nematic liquid crystal with negative anisotropic dielectric constant and homeotropic anchoring, applying a sufficiently large transverse electric field generates a molecular reorientation, known as *the Fréedericksz transition* [18]. This transition is characterized by the spontaneously emergence of a vortex gas. Due to the attraction and annihilation of vortices pairs, the system ultimately finds its homogeneous equilibrium state, characterized by the fact that the molecules in the bulk are misaligned from the ap-

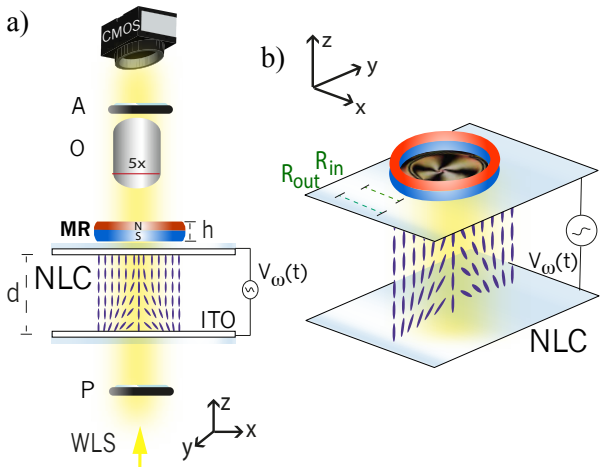

FIG. 1. Schematic representation of the experimental setup. (a) Vertical description of the experimental setup. NLC accounts for the nematic liquid crystal cell, d is the thickness of the cell, ITO accounts for the transparent electrode (indium oxide and tin), $V_\omega(t)$ is a harmonic voltage applied to the liquid crystal layer, where ω is the voltage frequency, MR is the magnetic ring of thickness h and internal and outer radius R_{in} and R_{out}, WLS is the while light source, P and A stand for polarizers, which are crossed, O accounts for the objective and CMOS is the complementary metal-oxide-semiconductor camera. The rods represent the average direction of molecules, directors. (b) Three-dimensional schematic representation of the liquid crystal cell under the influence of the electric and magnetic fields.

plied electric field [16, 17]. These topological defects are of great relevance because when interacting with the light they can be a source of optical vortex beams [19–22]. Alternatively, one can induce umbilical defects by means of intense light beams [23], photo-sensitive walls [21, 24], or by means of external magnetic and electric fields [25, 26]. The combined action of a distant magnetic ring with a uniform electric field into the nematic cell enables the self-engineering of macroscopic q-plate [26]. The possibility of manipulating vortices allows creating optical vortex lattices, which are useful for quantum computation [27], image analysis [28], and generation and data transmission [29].

This letter aims to show that a vortex triplet is induced by the combined action of a close magnetic ring and oscillatory electric field into a nematic liquid crystal layer. The vortex triplet is characterized by a positively charged vortex in the center and two vortices on its flanks of opposite charges. Namely, the triplet has a positive total topological charge consistent with that enforced by the magnetic ring. The vortex triplet is a consequence of the structure of the magnetic protuberance at the ring center, vertical electric field, and inherent anisotropy of the liquid crystal. For a low frequency of the driven voltage, we observe that the vortex triplet is unstable and gives rise to the appearance of a topological lattice. An amplitude equation allows us to explain the emergence of a vortex triplet and vortex lattice. Numerical simulations show a good agreement with experimental observations.

Experimental setup.– Figure 1 shows a schematic representation of the experimental setup. To study vortex dynamics, we consider a cell composed by two thin glass layers separated by a thickness of $d = 75$ μm, which is chemically treated on its interior walls to have a homogeneous homeotropic anchoring and with transparent electrodes included (indium oxide and tin, ITO with a thickness of 0.08 μm). This cell has been filled by capillarity with a nematic liquid cristal LC-BYVA-01-5G (Instec) with negative dielectric anisotropy $\epsilon_a = -4.89$, birefringence $\Delta n = n_e - n_o = 0.1$, rotation viscosity $\gamma = 204$ mPas, splay and bend elastic constant, respectively, $K_1 = 17.65$ pN and $K_3 = 21.39$ pN, and negative magnetic anisotropy χ_a (yet not measured). All experiments were conducted at room temperature of 21°C. A neodymium magnetic ring of 3200 G with a rectangular transversal section, outer radio $R_{out} = 7$ mm, internal $R_{in} = 2$ mm, and thickness of $h = 5$ mm is put onto the top of the nematic liquid crystal cell (cf. Fig. 1). The sample with the magnetic ring is introduced in an Olympus Bx51 microscope and it is sandwiched with two linear cross polarizers. A sinusoidal voltage of intensity $V_0 = 7.95$ Vpp, near to the reorientational transition, *Fréedericksz voltage* $V_{FT} = 6.57$ Vpp, with a frequency of $\omega = 100$Hz is applied to the sample. The system is illuminated by a white light (Halogen lamp). The temporal evolution of the liquid crystal cell under the simultaneous effects of the electric and magnetic field is monitored by a CMOS camera (Thorlabs DCC1645C), which allows us to observe the central zone of the magnetic ring.

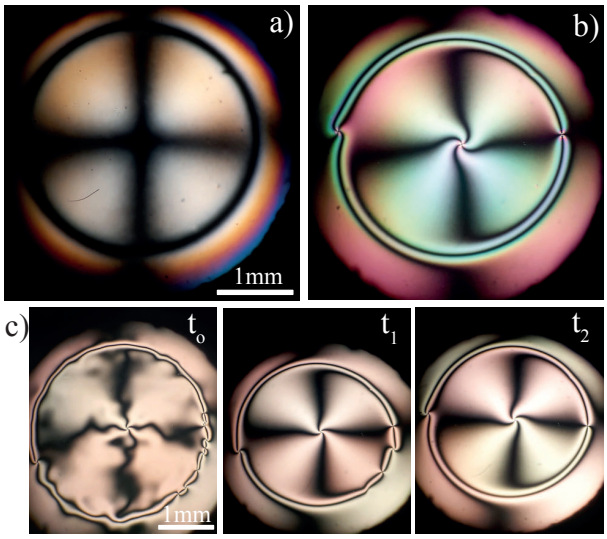

FIG. 2. Magnetic ring induced vortex triplet in a nematic liquid crystal layer. a) Snapshot of vortex observed close to the Fréedericksz transition $V_0 = 6.3$ Vpp. b) Snapshot of the vortex triplet observed above the orientational transition $V_0 = 7.95$ Vpp. c) A temporal sequence of snapshots of the emergence of vortex triplet formation $t_0 < t_1 < t_2$, far from the orientational transition $V_0 = 15.0$ Vpp.

Experimental observations of the vortex triplet.– When the liquid crystal sample is only under the influence of the magnetic field, there is no light transmission. Hence, the torque generated by the magnetic field is not capable of overcoming the elastic resistance; namely, the considering magnetic ring is not capable to induce the molecular reorientation. In order to generate this reorientation, a voltage drop is included orthogonal to the sample of the form $V_\omega(t) = V_0 \cos(\omega t)$. Due to negative electrical anisotropy and the simultaneous presence of the electric and magnetic field, we observe the reorientation transition for voltages less than the Fréedericksz voltage (critical voltage for the reorientation instability purely induced by an electric field). By increasing the magnetic intensity by using magnets of different thicknesses, we observe a transition of molecular reorientation for lower voltages. Unexpectedly, close to the reorientation instability, the emergence of a vortex with a thick core in the center with a ring near to the inner radius of the magnet is observed. Figure 2 shows the typically observed vortices. By increasing the voltage, we have a better resolution to observe the emergent structure that is made up of a positive vortex in the center and two vortices on its lateral flanks of opposite charges, *a vortex triplet* (cf. Fig. 2b). By turning off the voltage and then considering a higher voltage, the vortex structure emerges with a ring characterized by exhibiting multiple vortices with

alternating topological charges. Subsequently, these vortices are annihilated by pairs, and only two survive in the antipodes (see bottom panels in Fig. 2). The vortex triplet is the equilibrium state of the system.

An intuitive explanation of the appearance of a vortex triplet.– The induced vortex triplet is determined by the structure of the magnetic field generated by the magnetic ring. Since the magnet has a north and south pole parallel to the liquid crystal sample and a rectangular cross-section, then a magnetic protuberance is observed at the center of the ring [30]. Figure 3 shows the magnetic structure of a ring with a rectangular cross-section schematically. Dashed curves account for the magnetic protuberance. This magnetic protuberance is a consequence of the boundary condition imposed by the ring inner wall on the magnetic field. Liquid crystal molecules tend to orient ortogonal with the magnetic field as a consequence of the negative anisotropic magnetic susceptibility [16, 17]. When considering the liquid crystal sample inside the magnetic protuberance, it naturally induces a positive vortex at the center and also a circular defect line that circumscribes the vortex (cf. Fig. 3b). However, for homeotropic anchoring conditions, a defect line is unstable and always stabilizes in a set of vortices with alternating charges along the line [16, 17, 31]. Indeed, one expects this line to stabilize in vortices and, ultimately, only a few vortices to survive along the line. Observe that when the sample stands outside the magnetic protuberance, one only observes a single vortex, and there is no ring to circumscribe it [26]. Indeed, this can be accomplished by moving the liquid crystal sample away from the magnet.

Theoretical description of a vortex triplet.– The structure of the magnetic protuberance can be modeled in a first approximation by the magnetic field of a cylindrical magnet of the form

$$\vec{B}(\rho,z) = m\left[\frac{(3z^2-\sigma)\hat{z}}{(\rho^2+z^2)^{5/2}} - \frac{\hat{z}-3z\rho\hat{\rho}}{(\rho^2+z^2)^{3/2}}\right] + b_0\hat{z}, \quad (1)$$

where $\sigma > 0$ and b_0 are phenomenological dimensional parameters (meters^2 and tesla, respectively) that account for geometric features of the magnet ring, m is a constant that has a dimension of permeability per magnetic moment, and $\{z,\rho,\theta\}$ are the cylindrical coordinates. The origin of the coordinate is fixed at the center of the magnetic ring. Note that as a result of the azimuthal symmetry of the ring, the magnetic field does not depend on the θ coordinate.

To shed light on the mechanism of creation and pinning of vortices, we derive a model in the vicinity of the reorientational transition. As nematic liquid crystal molecules are weakly tilted from the axis $\hat{z}$the backflow effects can be neglected [17, 21, 24]. The molecular reorientation of the liquid crystal is described by the director vector $\vec{n}$ when the temperature is constant [16, 17]. The dynamic of the director is characterized by minimizing the

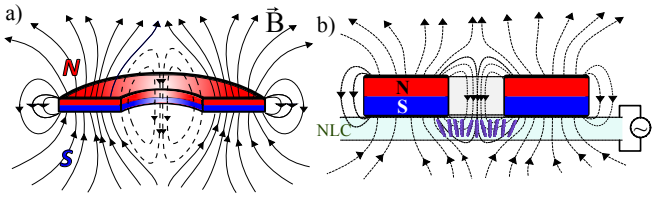

FIG. 3. Schematic representation of the magnetic field structure of a magnetic ring with a rectangular cross-section. a) Three-dimensional representation of the magnetic field. The curves account for the lines of the magnetic field. Dashed lines account for the structure of the magnetic field within the magnetic protuberance. b) Two-dimensional representation of the magnetic field of the ring onto the nematic liquid crystal layer. The rods stand for the average direction of molecules.

Frank-Ossen free energy

$$\mathcal{F} = \int dV \left\{ \frac{K_1}{2}(\nabla\cdot\vec{n})^2 + \frac{K_2}{2}(\vec{n}\cdot(\nabla\times\vec{n}))^2 + \frac{K_3}{2}(\vec{n}\times(\nabla\times\vec{n}))^2 - \frac{\epsilon_a}{2}(\vec{E}\cdot\vec{n})^2 - \frac{\chi_a}{2}(\vec{B}\cdot\vec{n})^2 \right\}, \quad (2)$$

where $\{K_1, K_2, K_3\}$ are the liquid crystal elastic constants, $\vec{E}$, and $\vec{B}$ are the electric and magnetic field, respectively [16, 17]. We consider a uniform vertical electric field $\vec{E} = E_z\hat{z} = V_\omega(t)/d\ \hat{z}$ and a magnetic field $\vec{B} = B_z\hat{z} + B_\rho\hat{\rho}$ given by formula (1).

To study the dynamics of the director, we will use the strategy, amplitud equation, presented in review [24] and references therein. Close to reorientational instability we use the ansatz

$$\vec{n} = \begin{pmatrix} \frac{\gamma\,\mathrm{Re}(A)}{a}\sin\left(\frac{\pi}{d}(z+\frac{h}{2})\right) \\ \frac{\gamma\,\mathrm{Im}(A)}{a}\sin\left(\frac{\pi}{d}(z+\frac{h}{2})\right) \\ 1-\frac{\gamma^2|A|^2}{2a^2}\sin^2\left(\frac{\pi}{d}(z+\frac{h}{2})\right) \end{pmatrix} + h.o.t., \quad (3)$$

where A accounts for the amplitud of the critical mode, $a^2 \equiv \left[(K_1-K_3)(\pi/d)^2 - 3\epsilon_a E_z^2 - 3\chi_a B_z^2\right]/4$ is a normalization constant, and $h.o.t.$ stands for high order terms in the critical amplitude. Using the above ansatz, Eq. (3), on the Frank free energy (2) and minimizing after straightforward calculations, one gets the amplitude equation (the dimensionless topologically driven Giznburg-Landau equation)

$$\gamma_0\partial_t A = \mu(\rho)A - |A|^2A + \nabla^2A + \delta\partial_{\eta\eta}\bar{A} + f(\rho)e^{i\theta}, \quad (4)$$

where the spatial coordinates have been scaled by $\vec{r}\to\vec{r}\sqrt{2/(K_1+K_2)}$, $\mu(\rho) = \mu_0+\mu_1(\rho)$ is the inhomogeneous bifurcation parameter, $\mu_0 \equiv -K_3(\pi/d)^2 - \epsilon_a E_z^2$ is the bifurcation parameter related to the electrical Fréedericksz transition, $\mu_1(\rho) \equiv \chi_a B_z^2(\rho,z_0)$ is the inhomogeneous modification of the reorientational transition, z_0 height of the liquid crystal sample, $\delta = (K_1-K_2)/(K_1+K_2)$

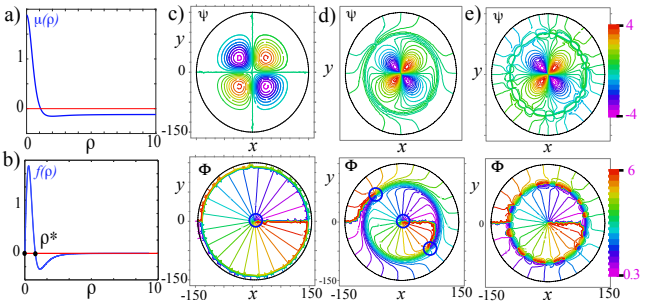

FIG. 4. Numerical simulation of vortex triplex obtained from the topologically Driven Gizburg-Landau Eq. (4) with $z_0 = 28$, $\sigma = 28$, $m = 13000$, $b_0 = 0$, $\gamma_0 = 1$, and $\delta = 0.1$. Profile of the inhomogeneous bifurcation parameter $\mu(\rho)$ (a) and topological forcing strength $f(\rho)$ (b) as a function of the radial coordinate. Contour plot of the polarized field $\psi(x,y) = Re(A)Im(A)$ (top panel) and phase field $\Phi(x,y) = \arctan[Im(A)/Re(A)]$ (bottom panel) of the complex amplitude A, below $\mu_0 < 0$ ($\mu_0 = -1$) (c) and above $\mu_0 > 0$ [$\mu_0 = 0.2$ (d) and $\mu_0 = 3.0$ (e)] the Fréedericksz voltage. Inserted circles highlight phase singularities.

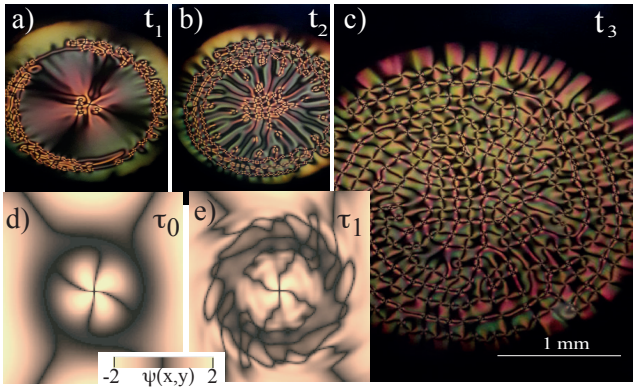

FIG. 5. Vortex lattices. a)-c) A temporal sequence of snapshots of the emergence of vortex lattice from a vortex triplet $t_1 < t_1 < t_3$, with $V_0 = 9.0$ Vpp and $\omega = 10$ mHz. d)-e) Numerical temporal sequence of vortex lattice, $\tau_0 < \tau_1$, obtained from the amplitude Eq. (5) with $z_0 = 15$, $\sigma = 2000$, $m = 1000$, $b_0 = 0.55$, $\gamma_0 = 0.5$, $\delta = 0.8$, $\Gamma = 1$, and $\omega = 1$.

accounts for the elastic anisotropy of the liquid crystal, $\partial_\eta \equiv \partial_x + i\partial_y$ is a differential operator in the complex plane, note that the laplacian satisfies $\nabla^2 = \partial_{\eta,\bar{\eta}}$, and $f(\rho) = 4\chi_a a^{1/4} B_\rho(\rho, z_0) B_z(\rho, z_0)/(\gamma\pi)$ accounts for the strength of the topological forcing. Notice a similar equation has been derived for liquid crystals with photosensitive walls but with a Gaussian forcing [21, 24], in which vortex induction has been demonstrated through the light-matter interaction. Figure 4 shows in left panels the bifurcation parameter and the forcing as a function of the radial coordinate. Notice that the vortices are placed at the zeros of the forcing. $f(\rho)$ is annulled at the origin and in the circumference of radius ρ^*. In the regime below the electrical Fréedericksz transition, $\mu_0 \lesssim 0$, the system exhibits an analytical approximation of the form $A \approx f(r)e^{i\theta}/\mu_0$ [32]. Indeed, this solution is characterizing by exhibits a vortex at the center and also a circular defect line that circumscribes the vortex. Figure 4c shows numerical simulations of Eq. (4) for $\mu_0 < 0$. From the polarized field $\psi(x,y) \equiv Re(A)Im(A)$ (top panel) [24], we only detect the central vortex with a cross shape. The ring that circumscribes the central vortex is not detected because it has a small amplitude. This ring is only detected in the phase field $\Phi(x,y) = \arctan[Im(A)/Re(A)]$ (bottom panel), this ring has two singularities of opposite charges in its antipodes. Numerical simulations of model Eq. (4) were conducted considering a triangular finite element code with adaptive spatial and temporal steps, and a simulation box of dimensions 300×300 with Neumann boundary condition was considered. Increasing the bifurcation parameter, the central vortex swirls and the ring that encloses the amplitude notoriously show two vortices of opposite charges at the antipodes (see Fig. 4d), which is what we observe in experiments (cf. Fig. 2).

Starting from $A = 0$ and considering a larger bifurcation parameter, we see the vortex emerge at the center with a circular defect line that destabilizes into a set of vortices that begin to interact and annihilate in pairs (see Fig. 4e). Note that a similar phenomenon is observed in the experiment (cf. Fig. 2c). Hence, model Eq. (4) describes the emergence of a vortex triplet induced by the combined action of a magnetic ring and electric field into a nematic liquid crystal layer (see Figs. 2 and 4).

Unexpectedly, when we decrease the frequency to a fraction of hertz, experimentally, the vortex triplet is destabilized from both the central vortex and the ring that circumscribes it by the induction of vortices, resulting in a front of vortices invading the system (see Fig. 5). A stationary oscillatory vortex lattice characterizes the equilibrium state of the system. When the low-frequency oscillatory behavior of the electric field $E_z(t)$ is included one cannot neglect the inertia in the dynamics of the director. Then the amplitude equation takes the form

$$\partial_{tt}A + \gamma_0\partial_t A = \mu A - |A|^2 A + \nabla^2 A + \delta\partial_{\eta\eta}\bar{A} + f(\rho)e^{i\theta}, \quad (5)$$

where $\mu = \mu_0 + \mu_1(\rho) + \Gamma\sin(2\omega t)$. For large γ_0 and high frequencies, this model equation is approximated by Eq. (4). Namely, this model presents a triplet vortex solution. However, when the frequency is decreased, the amplitude A begins to oscillate. For a critical frequency, the ring around the vortex becomes unstable. This instability generates the emergence of vortex pairs. Figure 5 shows the typically observed vortex lattice structure and the triplet that becomes unstable.

In summary, the combined effect of the magnetic field of a magnetic ring and the uniform electric field onto a homeotropic nematic liquid crystal cell induces a stable vortex triplet and vortex lattice. An amplitude equation allow us to reveal the origin of the vortex triplet and the

emergence of vortex lattice. Theoretical findings show a quite fair agreement with experimental observations. The generated vortex lattices are obtained in a simple configuration that does not require a complex structure of electrodes, inhomogeneities, applications of thermal gradients, or photosensitive walls.

The authors thank M Kowalczyk for fruitful discussions. The authors acknowledge the financial support of the Millennium Institute for Research in Optics (MIRO). MGC thanks financial support for the Fondecyt 1180903 project.

[1] A. L. Fetter, and J. D.Walecka, *Theoretical mechanics of particles and continua* (Courier Corporation, 2003).
[2] G. Nicolis and I. Prigogine, *Self-Organization in Nonequilibrium Systems*, (Wiley, New York, 1977).
[3] L. M. Pismen, *Patterns and Interfaces in Dissipative Dynamics*, (Springer, Berlin, 2006).
[4] M. Cross and H. Greenside, *Pattern Formation and Dynamics in Nonequilibrium Systems*, (Cambridge University Press, New York, 2009).
[5] A.C. Newell , *Solitons in Mathematics and Physics* (Society for Industrial and Applied Mathematics, Philadelphia, 1985).
[6] M. Remoissenet, *Waves called solitons: concepts and experiments*, (Springer-Verlag, Heidelberg, 1993).
[7] *Dissipative Solitons: From Optics to Biology and Medicine*, Lecture Notes in Physics Vol. 751, edited by N. Akhmediev and A. Ankiewicz (Springer, Heidelberg, 2008).
[8] H. G. Purwins, H. U. Bodeker, and S. Amiranashvili, *Dissipative solitons*, Adv. Phys. **59**, 485 (2010).
[9] O. Descalzi, M.G. Clerc, S. Residori, and G. Assanto, *Localized States in Physics: Solitons and Patterns*, (Springer, 2011).
[10] M. Tlidi, K. Staliunas, K. Panajotov, A. G. Vladimiorv, and M. Clerc, *Localized structures in dissipative media: from optics to plant ecology,* Philos. Trans. R. Soc., A **372**, 20140101 (2014)
[11] P. Coullet, it Localized patterns and fronts in nonequilibrium systems Int. J. Bifurcation Chaos, **12**, 2445 (2002).
[12] L.M. Pismen, *Vortices in Nonlinear Fields*, (Oxford Science Publications, New York, 1999).
[13] I.S. Aranson, and L. Kramer, *The world of the complex Ginzburg-Landau equation* Rev. Mod. Phys. **74**, 99 (2002).
[14] E. Sandier and S. Serfaty, *Vortices in the Magnetic Ginzburg-Landau Model*, (Springer Science & Business Media, Boston, 2008).
[15] F. Bethuel, H. Brezis, and F. Helein, *Ginzburg-Landau Vortices*, (Springer Science & Business Media, New York, 2012).
[16] S. Chandrasekhar, *Liquid Crystals*, (Cambridge University Press, Cambridge, 1992).
[17] P.G. de Gennes and J. Prost, *The Physics of Liquid Crystals*, 2nd ed. (Oxford Science/Clarendon, Oxford, 1993).
[18] V. Freedericksz and V. Zolina, Trans. Faraday Soc. **29**, 919 (1927).
[19] E. Brasselet, N. Murazawa, H. Misawa, and S. Juodkazis, *Optical vortices from liquid crystal droplets* Phys. Rev. Lett. **103**, 103903 (2009).
[20] E. Brasselet and C. Loussert, *Electrically controlled topological defects in liquid crystals as tunable spin-orbit encoders for photons*, Opt. Lett. **36**, 719 (2011)
[21] R. Barboza, U. Bortolozzo, G. Assanto, E. Vidal-Henriquez, M.G. Clerc, and S. Residori, *Vortex Induction via Anisotropy Stabilized Light-Matter Interaction*, Phys. Rev. Lett. **109**, 143901 (2012).
[22] E. Brasselet, *Tunable Optical Vortex Arrays from a Single Nematic Topological Defect*, Phys. Rev. Lett. **108**, 087801 (2012).
[23] M. El Ketara, and E. Brasselet, E. *Self-induced nonlinear spin-orbit interaction of light in liquid crystals*, Opt. Lett. **37**, 602 (2012).
[24] R. Barboza, U. Bortolozzo, M.G. Clerc, S. Residori, and E. Vidal-Henriquez, *Optical vortex induction via light-matter interaction in liquid-crystal medial* Adv. Opt. Photon. **7**, 635 (2015).
[25] P. Pieranski, B. Yang, L.-J. Burtz, A. Camu, A. and F. Simonetti, *Generation of umbilics by magnets and flows* Liq. Cryst. **40**, 1593 (2013).
[26] E. Brasselet, *Tunable High-Resolution Macroscopic Self-Engineered Geometric Phase Optical Elements*, Phys. Rev. Lett. **121**, 033901 (2018).
[27] H. H. Arnaut and G. A. Barbosa, Orbital and Intrinsic Angular Momentum of Single Photons and Entangled Pairs of Photons Generated by Parametric Down-Conversion. Phys. Rev. Lett. **85**, 286 (2000).
[28] F. Tamburini, G. Anzolin, G. Umbriaco, A. Bianchini, and C. Barbieri, Phys. Rev. Lett. 97, 163903 (2006).
[29] J. Wang, J.-Y. Yang, I.M. Fazal, N.Ahmed, Y. Yan, H. Huang, Y. Ren, Y. Yue, S. Dolinar, M. Tur, and A. E. Willner, Terabit free-space data transmission employing orbital angular momentum multiplexing. Nat. Photonics **6**, 488 (2012).
[30] I. Lebedev, Tekhnika Molodezhi 6, 2 (1991) [see, also, http://n-t.ru/tp/mr/mmk.htm]; M.F. Ostrikov, New manifestations of magnetism. (St. Petersburg, 1994).
[31] J.M. Gilli, M. Morabito, and T. Frisch, Ising-Bloch transition in a nematic liquid crystal. J. Phys. II France **4**, 319 (1994).
[32] E. Calisto, M.G. Clerc, M. Kowalczyk, and P. Smyrnelis, *On the origin of the optical vortex lattices in an nematic liquid crystal light valve,* Opt. Letts. **44**, 2947 (2019)

Appendix F
Wings of vortexes pairs

Honorable mention in Micro-imaging category from the 2018 Royal Society Publishing Photography Competition